Investigations on experimental and computational trim optimisation methods

Ocean Engineering 288 (2023) 116098

Contents lists available at ScienceDirect

Ocean Engineering

journal homepage: www.elsevier.com/locate/oceaneng

Investigations on experimental and computational trim optimisation methods☆

Kadir Burak Korkmaz [a,b,*], Sofia Werner [a], Rickard Bensow [b]

[a] RISE-SSPA Maritime Center, Chalmers Tvärgata 10, Box 24001 Se-400 22, Göteborg, Sweden
[b] Chalmers University of Technology, Sweden

ARTICLE INFO

Keywords:
Trim optimisation
CFD
Combined EFD/CFD methods
Transom flow
Ship monitoring
Verification and validation

ABSTRACT

Shipping is vital for global trade but also emits significant greenhouse gases. To address this issue, various measures have been proposed, including improved ship design, alternative fuels, and improved operational practices. One such cost-effective operational measure is trim optimisation, which involves operating the ship at the hydrodynamically optimal forward and aft draughts.

This study focuses on investigating the trim trends of a RoPax vessel using experimental fluid dynamics (EFD) and computational fluid dynamics (CFD) methods. The trim trends are derived in resistance and self-propelled modes. Multiple CFD methods are examined, along with different extrapolation techniques for experimental results. Uncertainty assessment is conducted for the experimental data, and a verification and validation study is performed. Furthermore, the predictions are compared with real operational data. The findings reveal that determining trim trends solely in towed mode is inadequate due to the profound influence of the operating propeller. Some of the investigated CFD methods demonstrate good agreement with the model test results in self-propelled mode, while others exhibit limitations. By selecting appropriate models and configurations, this study demonstrates that trim trends can be determined with sufficient precision, as evidenced by the comparison between ship operational data and predictions from EFD and CFD methods.

1. Introduction

Seaborne transportation plays a crucial role in global trade by mobilising more than 80% of the cargo carried worldwide but emitting almost 3% of global greenhouse gas (GHG) emissions (IMO, 2021). According to the long-term economic and energy scenarios, IMO (2021) projects that the shipping emissions will increase by 90%–130% compared to the levels of 2008 by 2050. Considering the steady growth in seaborne trade over decades and the goals set by IMO to reduce GHG emissions from shipping, one of the most feasible paths is to increase the energy efficiency of ships. In line with the vision, IMO has introduced regulations to mitigate the harmful emissions from shipping, such as the Energy Efficiency Design Index (EEDI) (IMO, 2011). The EEDI regulations aim to promote high energy efficiency designs and eliminate inefficient ships from joining the market. As calculating the EEDI index is now a mandatory step, the applicable ships must undergo pre-verification during the design phase of a new ship. Therefore, solutions towards higher efficiency that can be implemented during the design phase, such as hull form optimisation and utilising energy saving devices, gained attention.

The two new regulations introduced by IMO taking effect from the beginning of 2023, Energy Efficiency Existing Ship Index (EEXI) (IMO, 2022b) and Carbon Intensity Indicator (CII) (IMO, 2022a), are aiming to measure existing ships' energy efficiency and to monitor a ship's operational carbon intensity, respectively. IMO defines carbon intensity as a measure of GHG emissions per the amount of cargo carried over the distance travelled and sets goals to gradually reduce the carbon intensity levels (40% by 2030). Unlike the EEDI and EEXI, the CII value can also be improved by better operation of the vessel, such as speed and route optimisation, hull and propeller cleaning, lowering the power consumption of the auxiliary systems, and trim optimisation (IMO, 2023).

As noted by Bertram (2020), possible energy savings for each alternative depend on many factors, such as the ship type, hull design, interaction with other energy saving devices or techniques, ship size, and sea state. The main topic of this study, trim optimisation, is applicable to almost all vessel types and typically results in a reduction of fuel consumption ranging from 0.5% to 5%, without requiring any modifications to the vessel's design or structure (IMO, 2023). The trim of the

☆ Investigations on experimental and computational trim optimisation methods.

* Corresponding author at: Chalmers University of Technology, Sweden.
E-mail addresses: burak.korkmaz@ri.se, korkmaz@chalmers.se (K.B. Korkmaz).

https://doi.org/10.1016/j.oceaneng.2023.116098
Received 5 June 2023; Received in revised form 16 October 2023; Accepted 18 October 2023
Available online 25 October 2023

vessel can be adjusted by loading the vessel accordingly, ballasting the vessel, or shifting ballast water between the tanks. Trim optimisation has larger energy saving potential for medium and slender vessels often trading in partial load conditions (Sames and Köpke, 2012) than the full block vessels with limited flexibility on trim variations (IMO, 2023). Moreover, each vessel's hull design and propulsion arrangement will result in different energy-saving potentials since the flow phenomena observed in combinations of different draught, trim, and speed are unique for each design.

The concept of trim optimisation originates from the fact that ship resistance and propulsive efficiency vary with different trim angles at a given displacement and ship speed. During the design phase, the hydrodynamic performance of vessels is often optimised for several loading conditions (e.g. design and ballast loading conditions) and speeds. However, real-life ship operations will occur not only in the 'optimised conditions' but also in partial loading conditions and speeds. The lowest propulsive power does not always occur at the even keel condition or some other fixed trim value for all combinations of different displacements and speeds. Instead, the minimum power can often be obtained at different trim angles at for various conditions and speeds. Therefore, the final design needs to be further evaluated at the design and off-design conditions by obtaining the delivered power at various displacements, trims, and speeds. This information can be used as a decision support tool by the crew. As a result, the optimum trim can be selected to achieve the minimum delivered power at a given displacement and speed during operation.

The decision support for trim optimisation can be generated in three ways: experimental methods (experimental fluid dynamics, EFD), computational methods (computational fluid dynamics, CFD), and through the analysis of real operations based on data measured by the onboard systems. The experimental method involves model testing in a towing tank, and then the model test results are extrapolated to full scale. Both steps, testing and scaling, introduce different uncertainty sources to the final predictions for the trim optimisation trends of the full-scale vessel. The measurement uncertainties related to the towing tank tests are incredibly scarce in the literature. Quantification of the measurement uncertainty is not only a valuable input to determine the confidence in the test results but a mandatory input for the validation of computational methods at model scale (Korkmaz et al., 2021b,a).

The uncertainties related to the extrapolation methods are caused by the assumptions involved in scaling from the model to full-scale. As discussed in Sections 2.1 and 2.2, the 1957 ITTC Performance Prediction Method and the 1978 ITTC Performance Prediction Method almost entirely differ in the scaling of the resistance and self-propulsion results. Moreover, the model test scope required for each extrapolation method differs; for example, the ITTC-57 method requires only self-propulsion tests, while the ITTC-78 method requires resistance, self-propulsion, and propeller open water tests. Reichel et al. (2014) investigated extrapolation methods with several different assumptions, such as individual form factors or thrust deduction for each loading condition versus fixed form factor and thrust deduction obtained from the even keel loading. It was observed that the optimum trim predictions from different scaling procedures differ by varying degrees at slow, medium and high speeds. Considering that the simplified method could have decreased the towing tank scope significantly while producing somewhat comparable results to the more extensive testing and detailed extrapolation procedure, Reichel et al. (2014) concludes that the choice of the scaling procedure is a compromise between the required level of accuracy and the resources dedicated to towing tank testing.

A challenge for the extrapolation methods that may occur frequently in trim optimisation investigations is the flow recirculation behind the transom. As the trim optimisation tests are performed at trim by bow and stern, the transom submergence will likely be substantial in some stern trim conditions. If the transom is followed by a flow recirculation (i.e. wetted transom or partially dry transom), Korkmaz et al. (2022) showed that the recommended procedure of the International Towing Tank Committee (ITTC), ITTC-78 method, is not suitable for extrapolation because the form factor assumption (Hughes, 1954) is violated and viscous resistance is underpredicted in full scale. In such cases where the transom submergence is significant, and flow separation is observed behind the transom, a correction method was proposed in Korkmaz et al. (2022) for correcting the full-scale viscous resistance.

The second approach to determine trim optimisation trends is the computational methods. The most popular contemporary computational technique used in the literature is the free-surface (FS) Reynolds-averaged Navier–Stokes (RANS) approach (Chen et al., 2019; Islam and Guedes Soares, 2019; Mahmoodi et al., 2023; Mahmoodi and Hajivand, 2022; Sun et al., 2016; Shivachev et al., 2017). According to the literature mentioned, the computations are most commonly performed in model scale, and the resistance simulations are overwhelmingly more common than the self-propulsion computations. The validation of free-surface RANS computations with the experimental results indicates that the numerical methods are mature enough to reasonably provide the trim trends in model scale (Sun et al., 2016; Shivachev et al., 2017; Lemb Larsen et al., 2012). Recent publications presented (Mahmoodi et al., 2023; Mahmoodi and Hajivand, 2022) simulated the trim optimisation tests not only for resistance but also for self-propulsion. They concluded that the trim considerably affects the propulsive factors, and their effects are not negligible. The importance of performing self-propulsion tests was also emphasised through towing tank tests by Lemb Larsen et al. (2012) as approximately 20% of the total gain in energy efficiency originates from the increased propulsive efficiency at the optimum trim condition.

Another computational method for obtaining the trim trends is the potential flow approach. As explained in Hansen and Freund (2010), the potential flow code is used to obtain the wave resistance (or residual resistance), and the viscous resistance is approximated through a friction line and a form factor; hence, the total resistance is obtained for each loading condition, and trim trends are obtained. However, the potential flow fails to model highly viscous effects, such as the recirculation zone at the stern. In such cases, the trim matrix can be adjusted or calibrated with full-scale RANS computations as noted in Hansen and Freund (2010). The comprehensive investigations performed by Lemb Larsen et al. (2012) show that the potential flow provides similar trim guidance as the EFD and RANS approach, but it largely underpredicts the trim trends. Additionally, the potential flow codes can experience convergence problems when the wave deformation is sharp, such as for breaking waves (Lemb Larsen et al., 2012); therefore, computing the whole trim, draught, and speed combinations poses a challenge for some ships.

According to the literature, more advanced numerical approaches such as detached eddy simulation (DES) or large eddy simulation (LES) are not commonly used for trim optimisation determination, probably due to overwhelmingly higher computational demand for DES and LES than RANS (Kanninen et al., 2022).

The last approach to determine trim optimisation trends is through the analysis of real operations-based data, referred to as *ship monitoring data* in this study. Depending on the analysis type (white box numerical models, black box models, and grey box models), the ship monitoring data is used to construct a model to predict the ship's behaviour in terms of resistance or self-propulsion with a set of variables, such as ship speed, draught, trim, and environmental conditions (Coraddu et al., 2017). As the trim is one of the independent variables (also referred to as a feature in machine learning) for the model, the trim trends can be effectively extracted, or the optimum trim can be calculated for an arbitrary loading condition and ship speed (Hüffmeier et al., 2020).

This study aims to address the knowledge gap in comparing different methods for extracting trim trends, which are crucial for decision support onboard. Previous literature lacks a comprehensive comparison of the various methods in terms of cost and accuracy. Therefore, it is

important to conduct a direct comparison of these methods to determine their suitability and provide valuable guidance for selecting the most appropriate method. This study fills this gap in the literature and offers insights that can enhance decision-making processes onboard, considering both the cost and accuracy of the methods used for trim trend extraction. The scope of this study includes investigations on the trim optimisation trends of a RoPax vessel using both experimental and computational methods. Resistance and self-propulsion model tests have been performed together with an estimation of the measurement uncertainty. The model scale trim trends from the resistance and self-propulsion tests have been compared to the predictions from different CFD methods together with a thorough verification and validation exercise. Full-scale power predictions from different extrapolation methods have been calculated for each displacement, trim, and speed. The extrapolated predictions are compared to full-scale CFD predictions from two different methods. The trim trends obtained in model and full scale are discussed, and the differences are explained through flow visualisations. The final step compares the full-scale predictions to the ship monitoring data. Through the analysis of the trim trends, this paper aims to

- explain the physics behind the trim optimisation trends
- quantify the differences between the trim trends obtained at model and full scale
- assess the accuracy of different CFD methods and suggest a recommended CFD approach through verification and validation
- highlight issues with model test extrapolation methods regarding the trim optimisation tests and discuss the implications
- compare the ship monitoring data with the predictions from EFD and CFD.

Overall, this study aims to provide valuable insights into trim trend extraction methods, guiding ship owners and operators in selecting the most appropriate method.

This paper is structured as follows: Section 2 describes the experiment based model to full-scale extrapolation methods. The two flow solvers used in this study, SHIPFLOW and FINE™/Marine codes, are introduced together with the numerical methods, computational domain and boundary conditions in Section 3. In addition, a coupled CFD-empirical method is presented in Section 3 as an alternative to the full scale self-propulsion CFD computations. In Section 4, the test case used in this study is presented together with the full-scale ship monitoring data collection process, and the conditions for the experiments and computations. The details for the resistance and self-propulsion tests, the testing facility, measurement equipment and the results of the measurement uncertainty analysis are presented in Section 5. The verification and validation (V&V) results in model scale, and the verification results in full scale for resistance and self-propulsion are presented including the modified V&V procedure, and details for the grid generation in Section 6. The model scale trim trends obtained from the towing tank tests and multiple CFD methods are compared together with a discussion of the flow physics behind the trim trends, the change of the resistance components with regards to trim and the effect of a working propeller in Section 7. Section 8 presents the full-scale trim optimisation trends from different extrapolation methods, CFD computations and ship monitoring data. In addition, the implications and the shortcoming of using different model to full scale extrapolation techniques are discussed together with the scale effects observed between the model and full scale CFD computations in Section 8. Moreover, the data analysis process of full-scale ship monitoring data is explained in Section 8.4. Finally, the conclusions are summarised in Section 9.

2. EFD based model for full-scale extrapolation methods

In this study, three model to full scale extrapolation methods are utilised: 1957 ITTC Performance Prediction Method, the standard 1978 ITTC Performance Prediction Method (ITTC, 2021a), and the 1978 ITTC Performance Prediction Method with the empirical transom correction (Korkmaz et al., 2022). The same towing tank test results are employed for different extrapolation methods to predict full scale speed–power relations.

2.1. 1957 ITTC performance prediction method

The ITTC-57 method significantly differs from the contemporary extrapolation methods, as it does not require resistance and propeller open water tests to predict the delivered power (P_{DS}) and propeller rotation rate (n_S). To predict the power and the rate of revolutions, a self-propulsion test is required, where the model is towed at speeds that yield the same Froude numbers (Fr) as those for the full-scale ship. The propeller rate of revolutions is adjusted during each run so that the towing force (R_a) is attained. The simple extrapolation from the model (denoted with M in the subscript) to full scale (denoted with S in the subscript) is performed using with Froude's law of similarity. For each Froude number, n_S and Q_S are obtained as follows:

$$n_S = n_M / \sqrt{\lambda}, \tag{1}$$

where λ is the scale factor (ship dimension/model dimension), and,

$$Q_S = Q_M \frac{\rho_S}{\rho_M} \lambda^4, \tag{2}$$

where ρ_S is the mass density of seawater and ρ_M is the mass density of the towing tank water.

The laws of similarity in Eqs. (1) and (1) are applicable when the model propeller is unloaded with the towing force, which accounts for the difference between the frictional resistance of the model and the frictional resistance of the ship converted into the model scale with a friction correction. The delivered power is calculated as

$$P_{DS} = n_S Q_S 2\pi \ . \tag{3}$$

2.2. The standard 1978 ITTC performance prediction method

The ITTC-78 method, as recommended by ITTC (2021a), is employed without any modification to extrapolate the towing tank test results to full scale. To predict the power and the propeller turning rate, tests for resistance, self-propulsion and, propeller open water are required, as the scaling procedure is more detailed than the ITTC-57 method.

As recommended in ITTC (2021a), the ITTC-57 model-ship correlation line (ITTC, 1957) is used in the extrapolation of the resistance. In accordance with the recommended procedure of ITTC (2021g), the form factors of each loading condition were determined by the Prohaska method (Prohaska, 1966), supplemented by the CFD based form factor method (Korkmaz et al., 2021b,a; ITTC, 2021d,e). The scaling of the resistance is performed with the assumption that the form factor is the same in the model and full scale, even though the form factor prerequisite of not having separated flow (Hughes, 1954) , violated in some loading conditions due to a partially wet transom.

The scaling of the resistance, propeller open water, and self-propulsion tests are explained in detail in the procedures ITTC (2021g), ITTC (2021c), and ITTC (2021a), respectively.

2.3. ITTC-78 method with empirical transom correction

This method is identical to the standard 1978 ITTC Performance Prediction Method for extrapolating propeller open water and self-propulsion tests, but it differs in the scaling of the resistance from model to full scale.

As mentioned in Section 2.2, some loading conditions involve substantial transom submergence, causing transom flow to be wetted or partially wetted. As explained by Korkmaz et al. (2022), wetted transom flow results in flow separation behind the transom, rendering the

form factor approach recommended in current procedures for scaling of the resistance invalid (ITTC, 2021g, p. 11). Therefore, the model and full-scale form factors are distinguished. The model scale form factor (k_M) remains the same as the standard ITTC-78 method (Section 2.2) and is obtained from the Prohaska and CFD-based form factor methods. The full-scale form factor (k_S) is calculated

$$k_S = k_M + k_{tr} \ , \tag{4}$$

where the k_{tr} is obtained from the empirical formula described in Korkmaz et al. (2022). The total resistance coefficient in full scale

$$C_{TS} = (1 + k_S)C_{FS} + \Delta C_F + C_A + C_R + C_{AAS}, \tag{5}$$

where k_S is the full scale form factor, C_{FS} is the frictional resistance coefficient, C_R is the residual resistance coefficient, ΔC_F represents the roughness allowance, C_A is the correlation allowance, and C_{AAS} is the air resistance coefficient. Similarly to the ITTC-78 method, the residual resistance in Eq. (5) is assumed to be the same in model and full-scale and it is obtained as

$$C_R = C_{TM} - (1 + k_M)C_{FM}, \tag{6}$$

where C_{TM} is the total resistance coefficient (the subscript 'M' signifies the model scale).

3. Computational methods

The SHIPFLOW and FINE™/Marine codes were employed for the computations. The former was utilised for the double-body RANS and the potential flow computations, while the latter was employed for the free-surface RANS simulations related to resistance and self-propulsion.

3.1. Double-body RANS-SHIPFLOW

SHIPFLOW version 6.5 was used to solve the steady state viscous flow. The solver, XCHAP, is based on the finite volume method (Broberg et al., 2014), and it can handle only structured grids. The grids for each loading condition were generated with SHIPFLOW's grid generator, XGRID. The hull was generated as a single block of structured grid and, the rudder, which is included in the form factor determination, was modelled in the computations using the overlapping grid technique (Regnström, 2008). The no-slip boundary condition was implemented using the wall resolved approach. Therefore, the first cell size in the normal direction to the hull was selected to ensure that the non-dimensional cell size y^+ value would be lower than 0.25 on average. The double-body computations were computed using the $k-\omega$ SST (Menter, 1994) turbulence model. Further details regarding to the flow solver, grid generation, computational domain, and boundary conditions can be found in Korkmaz et al. (2021a), where the quality assurance, as described in ITTC (2021f), was demonstrated for the CFD based form factor calculation method. This study followed the best practice guidelines outlined in Korkmaz et al. (2021a), with the exception of the domain size, which was increased longitudinally by a factor of 2 in the present study.

3.2. Fully nonlinear potential flow

The fully nonlinear potential flow solver of SHIPFLOW Motions version 7.0 was employed to obtain the wave resistance for each loading condition. The solver includes an unstructured automatic free surface mesh generator with adaptive grid refinement capability. However, in this project, the discretisation of the hull and the rudder (the other appendages were too far from the free surface and thus ignored) was performed manually. The grid density at the aftbody was generated especially fine because the solver keeps track of which grid panels are wet and thereby includes them in the boundary value problem. This precaution was taken since some loading conditions resulted in the stern waves just skimming the stern overhang; hence, the finer stern grid would provide more accuracy in determining the wetness. For more details about the SHIPFLOW Motions solver, see Kjellberg et al. (2022).

3.3. RANS-VOF

FINE™/Marine computing suite version 10.2 is used for the free-surface RANS computations. The incompressible RANS equations were solved with the ISIS-CFD flow solver based on the finite volume method. The face-based method is generalised for a multitude of grid types, including the three-dimensional unstructured grids. The velocity field is obtained from the momentum conservation equations, and the pressure is extracted from the continuity equation. In the same way as the momentum equations, the transport equations for turbulence modelling is discretised and solved. The AVLSMART discretisation scheme is used for both momentum and turbulence transport equations. All free-surface RANS computations were performed in steady state with $k-\omega$ SST (Menter, 1994) turbulence model (Menter, 1993). The detailed description of the solver is presented in Queutey and Visonneau (2007).

The free surface is modelled with a multi-phase flow approach (i.e. Volume of Fluid, VOF). In ISIS-CFD, the Blended Reconstructed Interface Capturing Scheme (BRICS) scheme is used for the multi-fluid discretisation scheme. Further details regarding the surface capturing method used in ISIS-CFD are given in Wackers et al. (2011).

The unstructured hexahedral grids were generated with the HEXPRESS™ module of the FINE™/Marine suite. The volume-to-surface approach is utilised for generating the non-conformal body-fitted full hexahedral unstructured grids around the hull and the appendages. Boundary layers were inserted between the no-slip wall and the surrounding hexahedral grids, as seen in Fig. 1(a). The grids were further refined with a local zone of refinement near the free surface in the entire domain to eliminate large grid spacing in the z-direction. The free surface refinement covers approximately all the draughts, while its extension in longitudinal and lateral directions was not restricted. In the case of self-propulsion, an additional cylindrical local refinement region is added just around the actuator disc to eliminate interpolation errors between the background grid and actuator disc. Further grid refinements were performed with the help of the Adaptive Grid Refinement (AGR) technique (Wackers et al., 2014) while the computation is running. The usage of AGR in the context of this study is thoroughly explained in Section 6.1.

Instead of generating separate grids for each loading condition and speed, one grid is generated per speed. For example, the model scale resistance computations for three speeds, three trims, and two displacements (six loading conditions, eighteen computations) were performed with three sets of grids. For each grid corresponding to a certain speed, only the first cell size normal to the no-slip wall is varied to aim for the same y^+ value. Hence, three grids only vary marginally in the boundary layer cells but are identical elsewhere. For a given speed, the base grid is generated for the static even keel (zero trim) heavy displacement condition. The grids for the other five loading conditions (aft and fore trims at heavy and light displacement) for each speed are obtained by an analytically weighted mesh deformation technique for body motion. In all computations, the body is fixed in surge motion but free to sink and heel. Therefore, the mesh is effectively deformed to follow the body motion.

The computational domains for all computations are shaped as a rectangular prism. The distances between the inlet to the fore perpendicular and the outlet to the aft perpendicular are 1.5 L_{PP} and 3 L_{PP}, respectively. The side of the domain is 2 L_{PP} from the centre-plane. The top and bottom boundaries of the domain are 1 L_{PP} and 1.5 L_{PP} from the baseline, respectively.

The solid wall boundaries (hull and the appendages) are modelled with a wall-law boundary condition in model and full-scale computations. The full-scale self-propulsion computations were performed with roughness, which is also modelled through a wall function approach. The sand-grain roughness height of 30 μm is chosen to represent the typical anti-fouling coating as recommended by Schultz (2007). Thanks

to the twin-screw propulsion arrangement, both resistance and self-propulsion computations were computed with the symmetry condition at the centre-plane. The inlet, outlet, and the side boundaries are classified as far-field condition, which can be Dirichlet or a Neumann condition depending on the local entering or leaving the domain. The top and bottom boundaries are set as Dirichlet condition that is based on the prescribed pressure, which is updated based on the hydrostatic pressure to account for the mesh moving vertically or the free surface position. The fluid is free to enter or exit from the top and bottom boundaries, simulating the unconstrained water depth and air.

The effect of the propellers was simulated with the actuator disc model of the ISIS-CFD solver. The body force terms from the actuator disc are included in the momentum equations of the cells where the centre of a control volume is located inside the actuator disc. The force distribution around the actuator disc can be default, uniform, user-defined or can be calculated with a propeller code. In this study, the default distribution (with normal and tangential forces) is used for self-propulsion computations. The torque and propeller rotation rate are predicted with the help of the propeller open water curve (POW). The POW values of K_T and K_Q against J were not computed with CFD but adopted from the model tests. The full-scale computations were performed with the extrapolated POW curves according to ITTC (2021c). The thrust of the actuator disc equals the drag in absolute value. However, external forces were applied to the hull in the model (the towing force R_a) and full scale (air resistance). Therefore, the thrust equals the summation of the drag and external force vectors but with a negative sign. The thrust, torque, and propeller turning rate are updated at every time step.

3.4. Combined RANS-VOF resistance and empirical propulsion model

This method is considered as an alternative to the full-scale propulsion CFD computations, which are considerably more resource-demanding compared to the resistance computations. Therefore, the alternative method uses the full-scale resistance values from the CFD computations and predicts the propulsive performance with an empirical method.

The empirical method is based on statistical analysis and the propeller open-water curves of the standard propeller series of SSPA. The thrust deduction, full-scale wake fraction, and relative rotative efficiency are obtained from a statistical analysis of SSPA's database, which has more than 8000 model test results. Through filtering of the relevant ship types, main dimensions, non-dimensional coefficients (i.e. block coefficient, LCB position, etc.), and propulsive arrangement, the propulsive factors were obtained. The changes in thrust deduction, full-scale wake fraction, and relative rotative efficiency with respect to the trim are also gathered from earlier trim optimisation tests.

In the empirical prediction program, the propeller diameter, pitch of the propeller at 70% radii, propeller type (fixed and controllable pitch), number of blades, and blade area ratio are entered as input. From the standard propeller series of SSPA, the relevant open-water curves are obtained. Using the full-scale resistance computations with FINE^{TM}/Marine (see Section 3.3), propulsive factors, and propeller characteristics, the delivered power and propeller rotation rate for the full-scale ship are predicted.

In this study, the test case is a twin-screw vessel; hence, the burden on the computational resources is not extremely different between full-scale resistance and self-propulsion computations. However, for a single skeg vessel, both sides of the hull have to be discretised for the self-propulsion computations. In addition, instead of an actuator disc, the propeller geometry can also be discretised (sliding mesh). In such cases, the required computational resources for a complete trim optimisation test scope will greatly differ between the resistance and self-propulsion computations. Therefore, the combined CFD and empirical method can be a cost-efficient alternative.

4. Test case, full-scale data collection, experimental and computational conditions

The test case used in this study is a RoPax vessel that was built more than a decade ago and is still in operation. The vessel operates only between two harbours; hence, the route remains the same. The vessel has a twin-screw propulsive arrangement. Each shaft line is tilted and supported by shaft bossings, an I-bracket, and a V-bracket. The transversal positions of the rudders are positioned nearly at the same y-position as the shaft line. In terms of hull lines, shaft arrangement, propulsion setup, and the propeller design, the test case can be considered as an ordinary RoPax vessel; however, due to the confidentiality of the hull lines and the propulsive arrangement, the images or drawings cannot be shared in this paper.

The trim optimisation scope is determined by a statistical analysis of the ship monitoring data. As a result, three speeds and two displacements were selected. The two displacements are named as light (denoted L) and heavy (called H) throughout the paper. Three trim conditions, 1.5 m trim by the bow, even keel, and 1.5 m trim by stern, were model tested. The trim is calculated as

$$trim = T_f - T_a \tag{7}$$

where T_f is the draught at the fore perpendicular, and T_a represents the draught at the aft perpendicular. As a result of the Eq. (7) convention, the trim by the bow is represented with a positive sign (trim> 0), while the trim by the aft is shown with a negative sign (trim< 0) in the paper.

The experimental conditions are thoroughly explained in Section 5.1. The model scale computations replicated the same conditions (speed, temperature, salinity, the model geometry as built, towing force in the self-propulsion computations, etc.).

The full-scale computations were performed for seawater at 15 °C. The superstructure of the vessel was not included in the computations. Instead, the same geometry as the model scale was used in full-scale computations, and the resistance due to air resistance is added as an external force in the computations. The air resistance was calculated as in ITTC (2021g) for each loading condition (two displacements and three trims). All computations were calculated for deep and unconstrained waters.

4.1. Ship monitoring data

The ship is equipped with a multitude of sensors that monitor and record the condition of the ship (draught at fore and aft perpendiculars, heel angle, speed over ground, speed through water), environment (current, depth below keel, water temperature, apparent and true wind speed and direction, now-casting based swell and wave height and period), and the performance of the vessel (propeller turning rate and shaft torque per propeller, fuel consumption). The data received from the ship owners start from 2015 to 2022, with a time interval of 10 min between each measurement. Installation of the sensors and collection of the ship monitoring data are performed by the ship owners; hence, the scope of this study is limited to the analysis of the collected data.

5. Model tests

Based on the drawings from the ship owner, a model made of plastic foam material called Divinycell was manufactured at SSPA with a 5-axis CNC milling machine. The appendages (shaft bossings, I-bracket, and V-bracket) were produced with high-precision 3-D printing, and the rudder was milled out of wood. After the surface finishing and painting, a 1 mm thick trip wire was mounted at 5% of L_{pp} aft from the fore perpendicular for the turbulence stimulation. The model is equipped with all the appendages, rudders, and dummy propeller hubs for the resistance tests.

The model tests were performed at SSPA's 260 m long, 10 m wide, and 5 metres deep towing tank. The complete scope of the test matrix,

Table 1
The components and the combined expanded uncertainties in percentage of the average forces for all loading conditions and the speed corresponding to 15 kn.

	L+1.5m $n = 2$, $t_{95} = 12.71$	L $n = 2$, $t_{95} = 12.71$	L-1.5m $n = 2$, $t_{95} = 12.71$	H+1.5m $n = 2$, $t_{95} = 12.71$	H $n = 4$, $t_{95} = 3.18$	H-1.5m $n = 4$, $t_{95} = 3.18$
Wetted area	0.180	0.180	0.180	0.179	0.179	0.179
Speed	0.128	0.128	0.128	0.128	0.128	0.128
Water temp.	0.021	0.021	0.019	0.021	0.021	0.018
Water density	0.003	0.003	0.003	0.003	0.003	0.003
Dynamometer	0.298	0.295	0.261	0.292	0.281	0.245
Repeat test, Deviation	3.058	3.479	5.650	1.674	1.539	0.785
Combined for single test (prediction limit)	3.080	3.499	5.660	1.714	1.580	0.852
Repeat test, Deviation of mean	1.765	2.009	3.262	0.967	0.688	0.351
Combined for test avg (confidence limit)	**1.804**	**2.042**	**3.280**	**1.034**	**0.775**	**0.482**

Table 2
The components and the combined expanded uncertainties in percentage of the average forces for all loading conditions and the speed corresponding to 17 kn.

	L+1.5m $n = 3$, $t_{95} = 4.30$	L $n = 3$, $t_{95} = 4.30$	L-1.5m $n = 3$, $t_{95} = 4.30$	H+1.5m $n = 3$, $t_{95} = 4.30$	H $n = 5$, $t_{95} = 2.78$	H-1.5m $n = 4$, $t_{95} = 3.18$
Wetted area	0.180	0.180	0.180	0.179	0.179	0.179
Speed	0.113	0.113	0.113	0.113	0.113	0.113
Water temp.	0.021	0.021	0.019	0.020	0.021	0.018
Water Density	0.003	0.003	0.003	0.003	0.003	0.003
Dynamometer	0.236	0.237	0.212	0.225	0.222	0.197
Repeat test, Deviation	0.785	0.126	1.355	0.585	1.994	1.155
Combined for single test (prediction limit)	0.848	0.343	1.388	0.662	2.017	1.190
Repeat test, Deviation of mean	0.393	0.063	0.678	0.293	0.814	0.516
Combined for test avg (confidence limit)	**0.506**	**0.325**	**0.741**	**0.426**	**0.870**	**0.592**

Table 3
The components and the combined expanded uncertainties in percentage of the average forces for all loading conditions and the speed corresponding to 19 kn.

	L+1.5m $n = 2$, $t_{95} = 12.71$	L $n = 2$, $t_{95} = 12.71$	L-1.5m $n = 2$, $t_{95} = 12.71$	H+1.5m $n = 2$, $t_{95} = 12.71$	H $n = 4$, $t_{95} = 3.18$	H-1.5m $n = 3$, $t_{95} = 4.30$
Wetted area	0.180	0.180	0.180	0.179	0.179	0.179
Speed	0.101	0.101	0.101	0.101	0.101	0.101
Water temp.	0.019	0.021	0.019	0.019	0.020	0.018
Water Density	0.003	0.003	0.003	0.003	0.003	0.003
Dynamometer	0.184	0.189	0.173	0.173	0.174	0.159
Repeat test, Deviation	1.467	2.298	3.615	1.768	3.413	1.849
Combined for single test (prediction limit)	1.493	2.315	3.625	1.789	3.424	1.868
Repeat test, Deviation of mean	0.847	1.327	2.087	1.021	1.526	0.925
Combined for test avg (confidence limit)	**0.891**	**1.356**	**2.104**	**1.056**	**1.550**	**0.961**

covering two displacements and three trim angles, was completed by the tests carried out in February and October of 2022. Two of the six loading conditions were repeated in both testing sessions, while the other four were tested only in October. Total resistance, sinkage, and trim were measured at each loading condition for three speeds. No blockage correction was applied to the measurements, as the area of the maximum transverse section of the model among all loading conditions is 0.64% of the sectional area of the tank, and the depth Froude number is low.

5.1. Measurement uncertainty analysis of the resistance tests

The uncertainty analyses of measurements of the total resistance in the resistance tests were performed according to ITTC (2021b). In an earlier study, the measurement uncertainty of KVLCC2 in ballast loading condition was presented in Korkmaz et al. (2021b) where ITTC (2014) was used. It should be noted that the procedures outlined in ITTC (2014) and ITTC (2021b) are broadly similar procedures. One of the main differences is the presentation of the uncertainties, which are reported as expanded uncertainty (95% confidence interval) in ITTC (2021b). The individual uncertainty components, wetted area, speed, water temperature, water density (absent in ITTC (2014)), dynamometer, repeat test deviation, and the combined uncertainties for the test average will be explained and presented in this section.

The uncertainties regarding the wetted surface area are quantified by measuring the model ballasting, i.e. the model and calibrated weights. Each calibrated weight (typically around 25 pieces) could not be measured for all six loading conditions due to the time limit. However, the statistics from the earlier study (Korkmaz et al., 2021b) were used together with the bias limits of two scales. As a result, the discrepancy between the actual displacement of the model and the nominal displacement obtained from hydrostatics was assumed to be similar to the earlier test with the KVLCC2 model (0.0375%).

The water temperature variation during the tests is also adopted from the earlier tests as the temperature variation was less than 0.1 °C (Korkmaz et al., 2021b). The water temperature difference between the two testing sessions in February and September was less than 2 °C as SSPA's towing tank is heated in cold temperatures and

sheltered from direct sunlight. In addition, the temperature difference between the model workshop and the towing tank was approximately 5 °C. Therefore, the thermal deformation of the model is expected to be limited. As described in ITTC (2021b), the measured resistance is converted to 15.0 °C, and the resulting expanded uncertainties on the water temperature and water density variation were calculated for the water temperature variation of 0.1 °C.

The expanded uncertainties of the towing speed are assessed by the bias limit of the towing carriage speed. As the towing speed for each run slightly deviates from the nominal value, the measured resistance is corrected for the nominal speed as described in ITTC (2021b).

The calibration uncertainty for the dynamometer originates from the uncertainty in the applied force during the calibration, the standard deviation of the time series from the Data Acquisition System (DAS), and the uncertainty of the linear curve fit. As indicated by ITTC (2021b), the first two terms are negligible for the calibration; therefore, the uncertainty of the dynamometer calibration was quantified by the standard error of estimate (SEE) from linear regression analysis. The dynamometer calibration range is approximately ten times larger than the maximum measured force. The dynamometer should also be considered when coupled with the DAS, where the data sampling rate, sampling period, and filtering are applied to obtain a single reading. During the tests, a sampling rate of 100 Hz was used. The time series were filtered with a 4th order low pass Butterworth filter with a cutoff frequency of 0.5 Hz. The standard uncertainties of the average of the sampling history of all runs are, on average, approximately 0.038%. Therefore, the uncertainty of a single "reading" (i.e., the average of a time history) from the DAS is considered negligible.

Based on the analysis described in ITTC (2021b), all components of uncertainties are summarised and combined through RSS (Root-Sum-Square) as listed in Tables 1 to 3. The vertical columns in the tables represent results for different loading conditions, which include a letter (L for light loading and H for heavy loading) and the following numbers indicating the amount of trim (+1.5m indicates trim by the bow and −1.5m indicates trim by the stern). If a number does not follow the letter L or H, the trim is zero (i.e. even keel condition). The n and t_{95} values under the loading conditions represent the number of repetitions and the T critical value from the Student's t distribution, respectively. As suggested in ITTC (2021b), the Student-t value, t_{95}, is adopted as the coverage factor since the number of repeats is small for many of the loading conditions due to the time limitations in the towing tank.

As seen in Tables 1 to 3, the contribution of the expanded uncertainties for the wetted surface, speed, water temperature and water density to the combined uncertainties is mostly insignificant. On the other hand, the major sources of the uncertainties originate from the dynamometer and the deviation of the repeat tests. The dynamometer uncertainty can be considered a secondary source of the combined uncertainty for 15 kn and 17 kn as seen in Tables 1 and 2. However, at the fastest speed as presented in Table 3, 19 kn, the dynamometer's uncertainty drops as the calibration's SEE becomes too small relative to the measured forces, which are much larger at this speed. The biggest contributor to the combined uncertainties is the deviation of the repeat tests for all loading conditions and speeds. The "Repeat test, Deviation" term in Tables 1 to 3 is calculated by

$$U = t_{95}\sigma\sqrt{1+1/n}\,, \tag{8}$$

where σ is the standard deviation of the force measured in the repeat tests. The "Repeat test, Deviation of mean" term is obtained by

$$U_{\overline{R}_T} = t_{95}s/\sqrt{n}\,. \tag{9}$$

The standard deviation, σ, of the repeat tests, on average, is 0.28%. However, the repeat test deviation terms, U and $U_{\overline{R}_T}$, are much larger because of the large coverage factors (t_{95}) used for calculating the uncertainties within the 95% confidence interval. As can be observed in the Tables 1 to 3, the t_{95} values used for Eqs. (8) and (9) can be very high due to the limited number of repetitions. As an example, the "L+1.5m" loading condition in Table 1 indicates the standard uncertainty for the repeat test deviations U and $U_{\overline{R}_T}$ are multiplied by 15.56 and 12.71, respectively, to cover 95% confidence interval.

The combined uncertainties in measurement for resistance are presented in two different forms, prediction limit and confidence limit. The former is calculated using the U term in Eq. (8) and ITTC (2021b) recommends using the prediction limit if the results are applied to the model to full-scale extrapolation. In the context of the present study, the uncertainty analysis is used for the validation of the CFD computations; hence, the combined for test average (confidence limit) will be used. As seen in Tables 1 to 3, the combined uncertainties are varying between 0.325% and 3.28%. This large variation can be mainly attributed to the number of repeat tests. However, the repeat test deviations can be relatively larger when flow around the hull features largely unstable flow phenomena: separation, breaking wave, and spill breakers, as observed in some loading conditions but not in others.

6. Verification and validation

This section discusses the verification and validation of the computation results from the RANS-VOF method (see Section 3.3). Grid refinement studies were performed for resistance and self-propulsion in both model and full scale. Therefore, four verification exercises are presented in Section 6.3 and Section 6.4. The validation results are only available in model scale as full-scale measurements with uncertainty estimations are not available.

6.1. Grid generation

The grid refinement study did pose challenges because unstructured grids were used with the RANS-VOF method, while one of the main requirements for verification is using geometrically similar grids (ITTC, 2021h). Using regular unstructured grid generators to obtain a constant ratio of cell sizes between two meshes, which should have cells of similar shape and orientation in any given position, is challenging, if not impossible. Therefore, the adaptive grid refinement technique is employed to generate a series of anisotropically refined meshes as recommended by ITTC (2021h).

The adaptive grid refinement (AGR) technique is implemented in FINEMARINE's ISIS-CFD solver. The original hexahedral grids generated by the grid generator can be further refined with AGR during the computation. Depending on the criterion selected, original cells can be divided into finer cells in either an isotropic or anisotropic way. The refinement of the same cell can be repeated several times, or earlier refinements can be undone until the AGR criterion is fulfilled with the desired cell sizes. As thoroughly explained in Wackers et al. (2017), anisotropic grid refinement is achieved by utilising metric tensors as refinement criteria, making it possible to determine cell sizes to be inversely proportional to the magnitude of the refinement criteria.

The refinement criterion used in this study is based on the combination of the Hessian matrix of second spatial derivatives and free surface refinement. The Hessian matrix of second spatial derivatives is interpreted as a measure of the truncation error for a second-order finite-volume discretisation (Wackers et al., 2017). The AGR criterion used throughout the RANS-VOF computations is based on Hessians of both the pressure and the velocity, which are weighted as they appear in the flux. The main advantage of the flux-component Hessian (FCH) criterion is that both pressure-based flows (waves, vortices) and boundary layers, shear layers and wakes can be tracked, and grids are refined precisely where needed.

Two protective measures have been implemented to keep the number of cell sizes at a certain level and improve the refined grids' regularity. The first measure is imposing a minimum cell size, which prevents infinite refinement around flow singularities and spurious refinement where large errors can be observed, such as the high aspect-ratio cells of the near-wall boundary layer grid. The minimum cell size

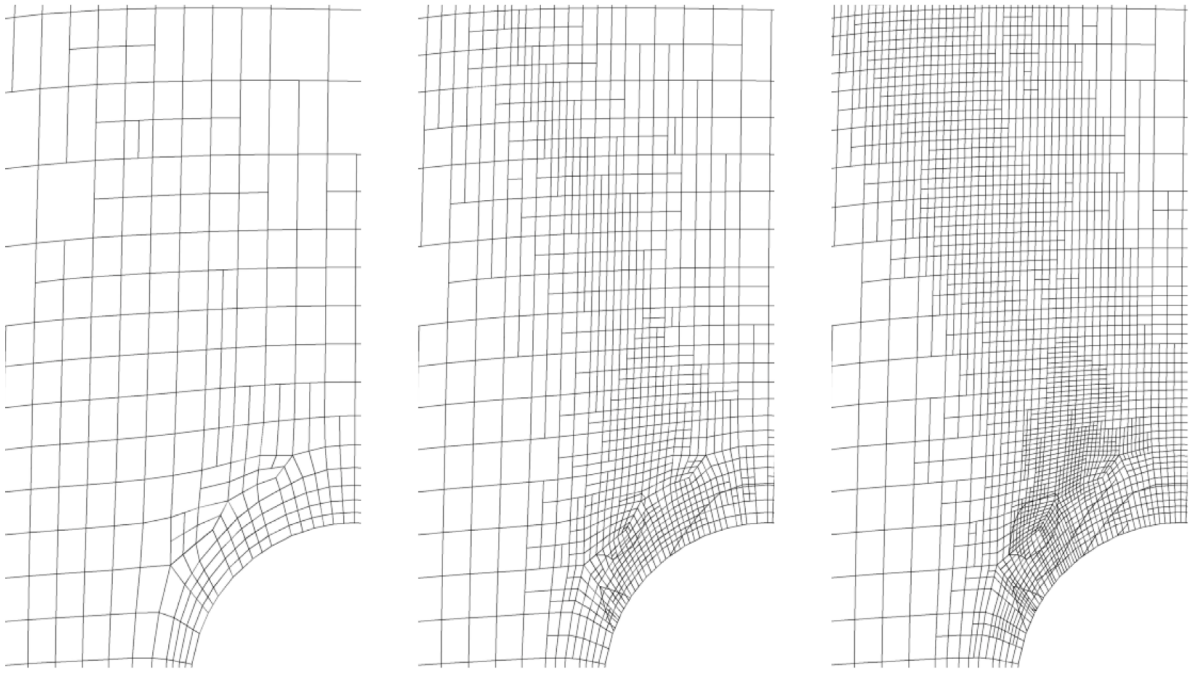

(a) $T_r = 4.0$ (b) $T_r = 2.0$ (c) $T_r = 1.00$

Fig. 1. Grid cells for different AGR criteria.

was set to $1 \times 10^{-4} \times L_{ref}$, where the L_{ref} is the length between perpendiculars in model or full scale for the corresponding computations.. The second measure is to protect the boundary layer grids where the original grid has layers of wall-aligned cells. To keep the number of wall-aligned layers the same, refinement is constrained to add cells parallel to the wall within the boundary layer grids. However, if a cell within the boundary layer grid needs refinement in the normal direction, all cells are refined from the wall to the outer layer; hence, the column/layer structure is preserved (Wackers et al., 2017). The first cell size normal to the wall is selected to obtain $y^+ \approx 30$ and $y^+ \approx 300$ for model and full-scale computations.

As mentioned, the AGR procedure divides the cells to refine the original grid. However, for geometrical similarity, the cells need to be divided in the middle, which can only be achieved by reducing the refinement criterion, T_r, by a power of two. If T_r is reduced in any other factor than a power of two, the cell sizes are divided by the nearest power of two. In this case, the grids are not formally geometrically similar but closely resemble each other. In addition, the grid size is not inversely proportional to the refinement criterion in the regions where the criterion is already satisfied, and the original grid is not refined.

An example from the grids generated for the grid refinement study is presented in Fig. 1. The grid cuts are in the y–z plane, cutting the shaft partially (the quarter circle in the bottom right corner) and longitudinally positioned just downstream of the V-brackets. As seen in Fig. 1, the grid is gradually refined with decreasing AGR criterion, T_r. It is easier to spot where the geometric similarity is not achieved than the other way around. Starting with the boundary layer grids around the no-slip wall of the shaft, no additional wall-aligned layers were added to the four layers from the original grid, as is the desired behaviour for grids with law-of-the-wall boundary conditions. Secondly, the cells at the bottom left corner of Figs. 1(a) to 1(c) indicate no change as the original grid already satisfies the AGR criterion. As explained in Wackers et al. (2017), improving geometrical similarity in the unrefined region is far less critical in reducing the numerical errors, and it does not hinder the verification study as this method is recommended by ITTC (2021b).

6.2. Verification procedure

ITTC (2021h) recommends that Richardson extrapolation and Least Squares Regression methods should be used for estimating the numerical uncertainties for unstructured grids. Therefore, the verification procedure is based on the method explained by Eça and Hoekstra (2014), wherein the numerical error is estimated as a function of the typical cell size. As discussed in Section 6.1, the systematically refined grids with AGR should, in principle, have typical cell size inversely proportional to the AGR criterion (T_r). Thus, the basic equation to estimate the discretisation error ϵ_S is:

$$\epsilon_S \simeq S_i - S_0 = \alpha(T_r)_i^p \ , \tag{10}$$

where S_i is the non-dimensionalised force coefficient, S_0 represents the estimate of the exact solution, p is the observed order of grid convergence, α is a constant for the power series expansion fit, and T_r is the AGR criterion which indicates the typical cell size. Note that only the refinement criterion of the flux-component Hessian criterion, T_r, will be mentioned in the verification study as the free surface refinement criterion is always changed with the same ratio as T_r for each grid.

The error estimation is performed in the least squares sense by minimising a set of functions (regular and weighted approaches), as explained in Eça and Hoekstra (2014), to determine S_0, p, and α. In addition, the standard deviation of the fits, denoted as σ, serves as a measure of the quality of the fits. Finally, depending on the observed order of convergence and the standard deviations obtained from regular and weighted approaches, the error is estimated, and the safety factor, as recommended by Roache (2009) is applied to ensure that the uncertainty estimation falls within the 95% confidence interval.

6.3. V&v results in model scale

6.3.1. Resistance computations

A grid refinement study for the resistance computations was performed with seven different AGR thresholds (i.e., seven systematically

refined grids) as explained in Section 6.1. As shown in Table 4, the difference in T_r between the finest and coarsest grids is eight, and each successive grid is not increased by a factor of two. Although, for strict geometrical similarity, the threshold value increase should be by a factor of 2 between the successive grids, selecting such a factor for would have been excessively resource-intensive especially for the finest grids. In the case of seven grids, the difference between the cell sizes would have been 64 times if a factor of two was chosen between the grids. Instead, two pairs of geometrically similar grid families were created: g1, g3, g5, g7 and g2, g4, g6. The adaptive grid refinement criterion of the flux-component Hessian criterion, T_r, and the free surface refinement criterion for the coarsest grid were determined by trial and error. The AGR criteria that increased in the total number of cells approximately 10% compared to the original grid was selected as the coarsest grid, g7. The flux-component Hessian criterion for the g7 approximately corresponds to $T_r = 4 \times 10^{-7} Re$, where Re is the Reynolds number. The free surface refinement criterion for the coarsest grid corresponds to $L_{W0} \times 0.025$ where L_{W0} is the fundamental wave length (Larsson and Raven, 2010, p.25),

$$L_{W0} = 2\pi Fr^2 L_{ref} \ , \tag{11}$$

where L_{ref} is the model scale waterline length. The g7 belongs to the first geometrically similar grid family, while g6 is the coarsest grid for the second geometrically similar grid family. The AGR criterion difference between g6 and g7 is adopted from Wackers et al. (2017). Within each grid families (g1, g3, g5, g7 and g2, g4, g6), the adaptive grid refinement criterion of the flux-component Hessian criterion, T_r, for each successive grid changes by a factor of two as presented in Table 4. As shown in Wackers et al. (2017), the two grid families are globally similar to each other and can be used for uncertainty estimation by the least squares approach. Therefore, estimation of the numerical errors were performed on the whole range of grids (g1, g2, g3, g4, g5, g6 and g7).

The computations were performed in double precision to discard the round-off errors. To eliminate the iterative convergence errors, the computations were performed with strict convergence tolerances, an exhaustively large number of time steps (approximately 7500) with ten non-linear iterations between each time step, and a relatively conservative time step of 0.01 seconds, which is approximately half of the recommended time step of $t = 0.0035 L_{ref}/V_M$ by Tezdogan et al. (2016). Therefore, it was assumed that discretisation errors dominate the numerical errors.

The numerical errors, U_{SN}, were estimated by the procedure proposed by Eça and Hoekstra (2014) as explained in Section 6.2. The numerical errors for viscous and pressure resistance coefficients are presented as error bars in Fig. 2. The numerical uncertainties and the computed values are plotted as a ratio of the finest grid solution $U_{SN}\%S_1$ and $S_i\%S_1$, respectively. In addition, the power expansion curves based on regular and weighted observed order of accuracy, p and p_w, are presented in Fig. 2. It is observed that both C_V and C_P exhibit monotonic convergence. The finest grid's numerical uncertainty for C_V and C_P is 0.31% and 8.70%, respectively. Some fluctuations can be observed between the computed values from successive grids, which can be attributed to the fact that the successive grids are not strictly similar, as mentioned earlier. Possibly, a higher-order error is present, considering the complexity of the flow. However, the standard deviation of the difference between the computed values on all grids and the power-law values are 0.17% and 1.9% of S_0 for C_V and C_P, respectively, indicating that the series of meshes produce asymptotic convergence reasonably well.

Verification and validation (V&V) analysis can be performed for the total resistance coefficient as the measurement uncertainties were determined in Section 5.1. The results of the V&V study are presented in Table 4. The comparison error E, numerical uncertainty U_{SN} and validation uncertainty U_V are presented as a ratio of the measured force D. The non-dimensional comparison error is

$$E\%D = (D - S_i)/D \times 100 \ . \tag{12}$$

Table 4
Verification and validation for total resistance coefficient C_T, $\sigma = 0.15\%$ of the exact solution and $U_D\%D = 0.87\%$.

Grid	Cells [M]	T_r	$E\%D$	$U_{SN}\%D$	$U_V\%D$
g1	11.55	0.75	0.64	1.24	1.51
g2	6.81	1	−0.06	1.61	1.83
g3	3.36	1.5	−0.46	2.17	2.34
g4	2.68	2	−1.03	2.96	3.09
g5	1.50	3	−2.41	4.60	4.68
g6	1.28	4	−3.73	6.40	6.46
g7	1.12	6	−6.78	10.07	10.11

Table 4 shows that the comparison errors are approximately within ±1% for the four finest grids. Remarkably, g4, with only 2.68M cells, is able to predict the resistance with such accuracy, considering that the test case is an open shaft vessel with a considerable number of appendages and rather challenging wave-making characteristics that will be discussed in the later sections.

The non-dimensional numerical uncertainty is calculated as

$$U_{SN}\%D = U_{SN}/D \times 100 \ . \tag{13}$$

Similar to the C_V and C_P, the total resistance coefficient also converges monotonically. The numerical uncertainty $U_{SN}\%D$ for C_T is 1.24% for the finest grid. As shown in Fig. 3, the fluctuations of the computed values between the successive grids are significantly reduced. The standard deviation of the difference between the computed values on all grids and the power-law values, σ, is 0.015% indicating that the grid series generated with the AGR refinement converge mostly asymptotically.

Assuming that input parameter uncertainty, U_{input}, is negligible, the validation uncertainty is calculated as

$$U_V^2 = U_{SN}^2 + U_D^2 \ , \tag{14}$$

where the measurement uncertainty is the combined for test average value ($U_D\%D$) from Table 2 for the heavy loading even keel condition (denoted as H). As shown in Table 4, the validation uncertainty is less than 2% for the two finest grids, thanks to low measurement and numerical uncertainties.

In order to exercise the validation procedure of ITTC (2021h), the three variables U_V, $|E|$, and U_{reqd} should be compared with each other. The required uncertainty, U_{reqd}, is determined as 2.5%, which should be the combination of typical values on U_{SN} (2%) and U_D (1%). According to the six combinations of the comparison of U_V, $|E|$, and U_{reqd} values in ITTC (2021h), all grids indicate that validation is achieved ($|E| < U_V$), and the comparison error is below the noise level. In addition, the finest three grids show the condition $|E| < U_V < U_{reqd}$, which means the validation is successful from a programmatic standpoint. For the finest three grids, attempting to estimate modelling errors is not feasible because the numerical and modelling errors are well within the reasonably small levels.

6.3.2. Self-propulsion computations

A grid dependence study was performed for self-propulsion at the model scale. The original grid generation for the self-propulsion computations is the same as the resistance simulations, except an additional cylindrical local refinement region is added around the actuator disc for the propulsion computations. The adaptive grid refinement criteria, the number of non-linear iterations, and the time step were identical to the resistance computations. To maintain the same standard of selecting the coarsest grid for the resistance and self-propulsion computations the same, the coarsest grid in the resistance computations, g7, is skipped

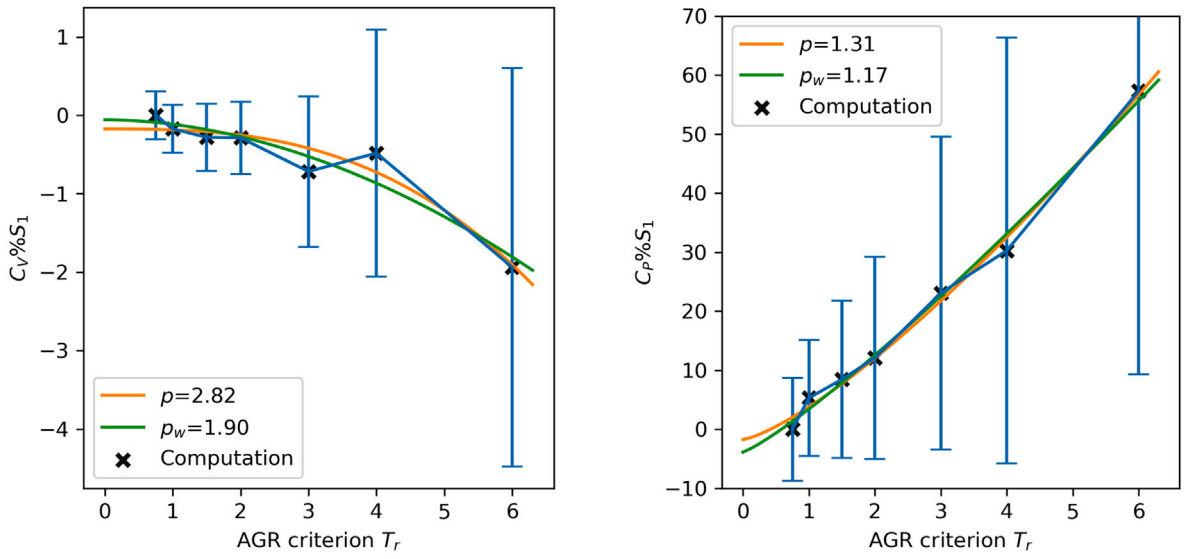

(a) Viscous Resistance Coefficient (b) Pressure Resistance Coefficient

Fig. 2. Computed resistance coefficients relative to the finest grid solution (S_1) with numerical uncertainties as error bars, and observed order of convergences against the AGR criteria.

Table 5
Comparison error and numerical uncertainty $E\%D$, $U_{SN}\%D$ of thrust, torque, propeller rotation rate and delivered power in model scale.

Grid	Cells [M]	T_r	T_M		Q_M		n_M		P_{DM}	
			$E\%D$	$U_{SN}\%D$	$E\%D$	$U_{SN}\%D$	$E\%D$	$U_{SN}\%D$	$E\%D$	$U_{SN}\%D$
g1	16.22	0.75	4.03	0.77	0.57	0.68	0.89	0.29	1.45	0.95
g2	10.40	1	3.62	0.99	0.21	0.89	0.75	0.39	0.95	1.26
g3	6.82	1.5	3.16	1.57	−0.17	1.38	0.64	0.60	0.47	1.93
g4	5.57	2	2.18	2.72	−1.04	2.41	0.30	0.94	−0.74	3.31
g5	4.79	3	1.14	5.45	−1.90	4.66	0.05	1.64	−1.85	6.28
g6	4.53	4	−2.39	8.46	−4.77	7.07	−0.80	2.32	−5.61	9.41

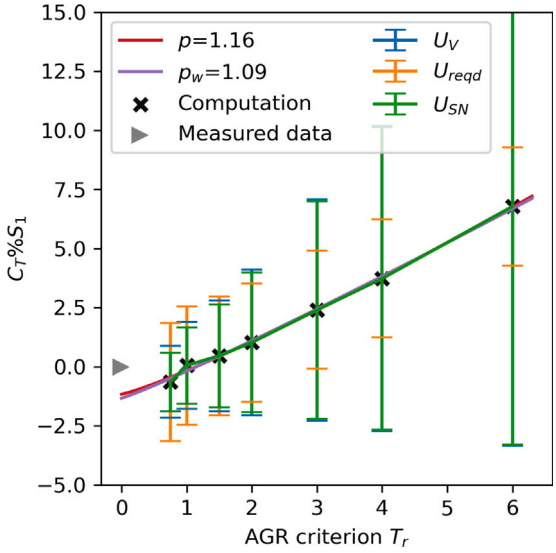

Fig. 3. Total resistance coefficient.

for the self-propulsion computations as the number of cells added by the AGR was less than 10% of the cell count of the original grid. However, as seen in Table 5, the total number of cells in the self-propulsion computations is 40% to 250% larger with the same AGR criteria in self-propulsion computations compared to the resistance simulations. A large number of additional cells indicates that even with a simplistic propeller model (actuator disc), resolving the relatively simple propeller jet adds considerable cost in terms of computational resources.

The comparison errors are calculated, and the numerical uncertainties are estimated for thrust (T_M), torque (Q_M), propeller rotation rate (n_M), and delivered power (P_{DM}). The self-propulsion results are presented in Table 5. Starting with the finest grid (g1), the comparison errors are less than 1.5% for Q_M, n_M, and P_{DM}, while the T_M is 4% under-predicted. These results require further attention as the thrust is the only value obtained directly, i.e. the pressure jump created by the propeller model. The torque and propeller rotation rate are obtained from the actuator disc program where the K_{TM} and K_{QM} from the POW curves are used as inputs. The resulting propeller turning rate and the advance ratio (J_{TM}) are used to calculate the predicted wake fraction

$$w_{TM} = 1 - \frac{J_{TM} D_M n_M}{V} , \tag{15}$$

where D_M is the model scale propeller diameter, and V is the free stream velocity. It is observed that the w_{TM} resulted in over-prediction, which partially counterbalanced the effect of a 4% under-prediction of thrust by shifting the advance ratio towards the model test value. As a result, the CFD predictions for the torque and rps read from the corresponding J_{TM} value in POW curves are significantly closer to the model test results compared to the thrust.

The estimated numerical uncertainties for T_M, Q_M, n_M, and P_{DM} are presented in Table 5 and visualised in Fig. 4. The order of accuracy for all self-propulsion characteristics and the fluctuations between the successive grids are similar. This similarity is expected as the self-propulsion computation is mainly based on the thrust value, which balances the resistance minus the towing force.

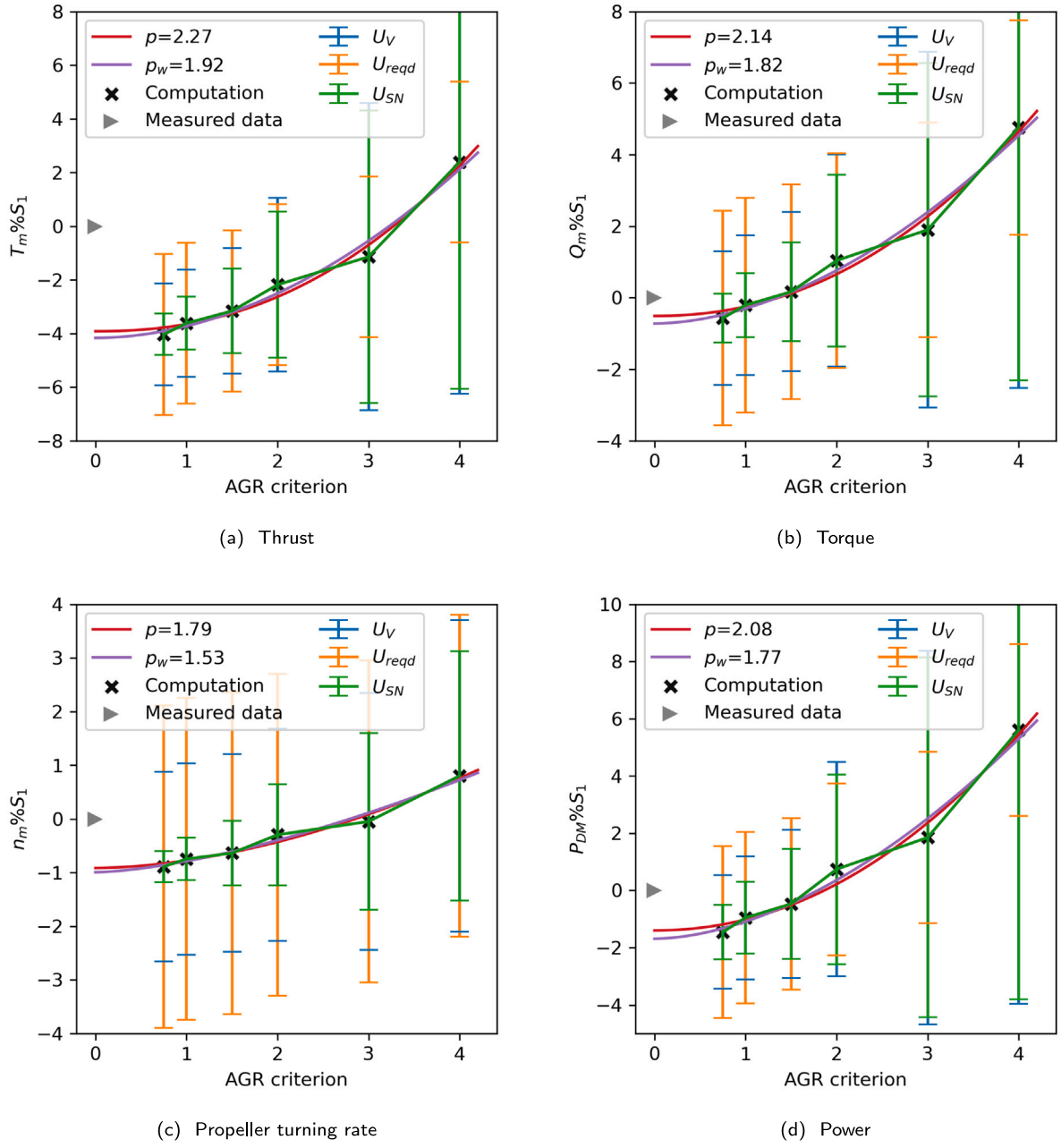

Fig. 4. Computed model scale self-propulsion results relative to the finest grid solution (S_1) with numerical uncertainties as error bars and observed order of convergences against the AGR criteria.

Even though the measurement uncertainties for the self-propulsion tests were not determined for thrust, torque, and the propeller turning rate, an attempt was made for a validation study. It is assumed that the measurement uncertainties will be similar in resistance and self-propulsion measurements; however, the U_D/D value from the resistance test (see Section 5.1) is multiplied by two as a safety factor for the self-propulsion. U_{reqd} is determined by assuming $U_D/D \approx 1.75\%$ and $U_{SN}/D \approx 2.5\%$ as typical values. Based on these assumptions, the validation study indicates that the comparison error is below the noise level for the fine grids' torque, propeller turning rate, and delivered power. However, the comparison error for the thrust is above the noise level, indicating that the modelling errors are significant. Considering the relative simplicity of the effective wake generated by the actuator disc model, this conclusion is expected.

6.4. V&v results in full scale

6.4.1. Resistance computations

A grid refinement study for the full-scale resistance computations was performed with seven different AGR thresholds similar to the model scale. From model to full scale, T_r values have been increased by a factor of 64 to keep the number of cells at reasonable levels. The original grid in full scale is nearly geometrically similar to the model scale original grid, except for the boundary layer grids where more layers were inserted parallel to the wall to capture the higher velocity gradients in full scale. Similar to model scale computations, a large number of time steps were computed with ten non-linear iterations between each time step. The time step is determined by $t = 0.0035 L_{ref}/V_S$ as proposed by Tezdogan et al. (2016) where V_S represents the full-scale ship speed.

The numerical uncertainties are estimated as explained in Section 6.2 and are presented in Table 6 for the viscous, pressure, and

Table 6
Numerical uncertainty $U_{SN}\%S_1$ of viscous, pressure and total resistance coefficient in full scale.

Grid	Cells [M]	T_r	$U_{SN}\%S_1$		
			C_V	C_P	C_T
g1	13.81	48	1.34	4.42	0.79
g2	9.67	64	1.67	6.50	1.14
g3	5.99	96	2.11	10.37	1.85
g4	4.91	128	2.48	14.38	2.74
g5	3.68	192	3.28	28.56	5.95
g6	3.22	256	3.87	43.93	9.57
g7	2.70	384	4.76	76.52	18.00

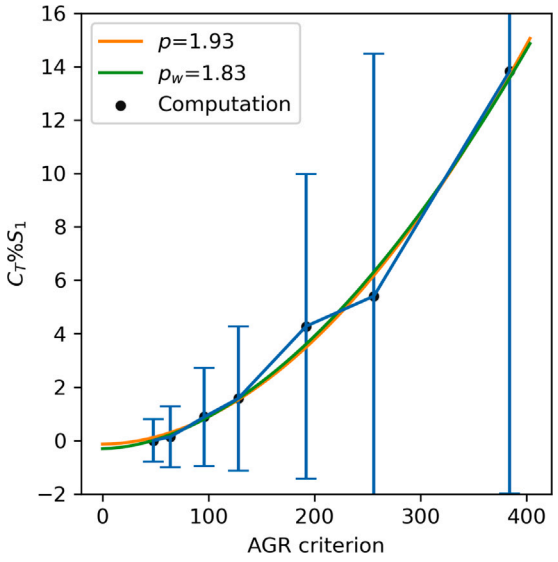

Fig. 5. Numerical uncertainties for the total resistance Coefficient.

Table 7
Numerical uncertainty $U_{SN}\%S_1$ of thrust, torque, propeller rotation rate and delivered power in full scale.

Grid	Cells [M]	T_r	$U_{SN}\%S_1$			
			T_S	Q_S	n_S	P_{DS}
g1	17.57	48	1.35	1.24	0.37	1.60
g2	13.26	64	1.39	1.30	0.42	1.69
g3	10.01	96	2.63	2.42	0.69	3.09
g4	8.49	128	3.45	3.21	1.00	4.20
g5	7.53	192	7.13	6.53	1.89	8.46
g6	7.32	256	10.08	9.13	2.55	11.81

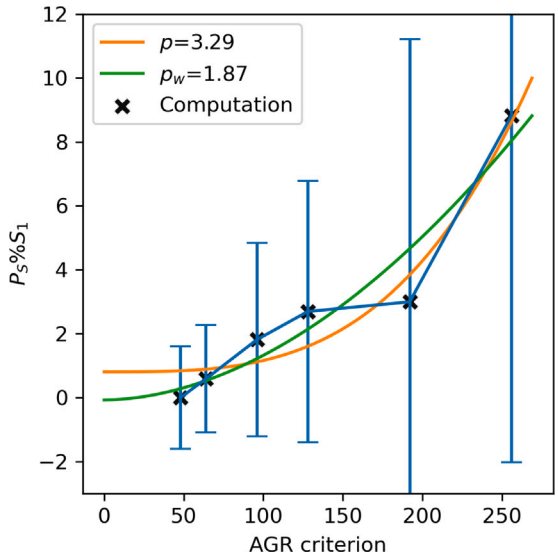

Fig. 6. Numerical uncertainties for the delivered power in full scale.

total resistance coefficients. The regular observed order of accuracy (p) for C_V, C_P, and C_T are 0.69, 1.74 and 1.93, respectively. Even though all coefficients indicate monotonic convergence, the p value for C_V indicates a considerable difference between the model and the full scale. In addition, the numerical uncertainties are significantly larger for C_V in full scale than in the model scale. At the same time, the $U_{SN}\%S_1$ for the total resistance coefficients decreased from model to full scale.

The numerical uncertainties, power-of-law curve fits and computed values for C_T are presented in Fig. 5. Similar to the model scale, g5 and g6 show some considerable fluctuations, which could be caused by the imperfect geometrical similarity between them but also the presence of higher-order errors. However, the standard deviation of the difference between the computed values on all grids and the power-law values is only 0.39% of the exact solution. Therefore, it can be argued that the series of meshes produce asymptotic convergence reasonably well.

6.4.2. Self-propulsion computations

A grid dependence study was performed for self-propulsion at full scale. The original grid generation for the full-scale self-propulsion computations is the same as the full-scale resistance simulations, except for an additional cylindrical local refinement region is added just around the actuator disc for the propulsion computations. The adaptive grid refinement criteria, the number of non-linear iterations, and the time step were identical to the full-scale resistance computations. However, as presented in Table 7, the total cell count in self-propulsion computations is considerably higher than in the resistance computations since the propeller jet needs to be resolved by the added cells from AGR. In addition, the law-of-the-wall boundary condition is modified in self-propulsion computations to simulate the standard hull roughness recommended by ITTC (2021g).

The estimated numerical uncertainties are presented in Table 7. Compared to the model scale, $U_{SN}\%S_1$ is larger in full-scale self-propulsion computations. However, the resemblance of the observed order of accuracy of the thrust and the other torque and propeller rotation rate is similar in model and full scale as a consequence of using the actuator disc model. As seen in Fig. 6, the computed values fluctuate around the power-law curve fits the most in full-scale self-propulsion computations compared to the full-scale resistance and model-scale computations. In addition, the standard deviation of the difference between the computed values on all grids and the power-law values from the weighted fit is 0.88%, significantly higher than in the earlier conditions. Considering the observed order of accuracy of 1.87 for the weighted fit, the series of six grids indicate asymptotic convergence at an acceptable level.

6.5. Selection of the grid for further computations

Based on the verification of a series of grids in the model and full-scale for resistance and self-propulsion computations, an AGR threshold can be determined for further computations. The AGR threshold should be sufficiently low to ensure reasonable numerical accuracy while maintaining manageable computational costs. However, the grid refinement study was limited to only one loading condition (H) out of six (see Section 4). In addition, the trimmed conditions from the towing tank experiments exhibited challenging flow phenomena such as breaking waves, separated flow and spill breakers. Therefore, it is anticipated that trimming by the bow and by the stern pose greater numerical challenges as either the transom stern significantly submerges and the

bulbous bow pierces the still water surface or the transom stern lifts up, and the bow with a large flare submerges.

The heavy loading condition at even keel (zero trim) condition was verified and validated for model-scale resistance computations as explained in Section 6.3. Using the same original grid as the $V\&V$ study, the trim by the bow (H+1.5m) and the trim by the stern (H-1.5m) conditions were simulated with the AGR thresholds corresponding to g1, g2, and g6 (see Table 4). The final grid for each loading condition should be globally similar, as the same AGR thresholds are used, and the mesh deformation technique is employed to solve the heave and trim motions of the vessel. In other words, the grids for the trimmed conditions originate from the same original grid as the even keel condition, and the mesh deformation technique achieves the final dynamic sinkage and trim condition for each loading condition while keeping the AGR threshold the same. Therefore, it is reasonable to assume that numerical uncertainties for the trimmed conditions are similar to those of the even keel condition.

The comparison errors for different loading conditions and grid fineness (AGR threshold) are presented in Table 8. Firstly, it should be noted that $E\%D$ values for the even keel condition (H) in Table 8 are not precisely the same as those reported in $V\&V$ (see Table 4), because the results in Table 8 were simulated again with less strict convergence tolerances, such as a smaller number of time steps and non-linear iterations between each time step. Performing the computations with fewer time steps and non-linear iterations is expected to introduce iterative errors. As a consequence, the numerical errors for the computations with less stringent convergence tolerances will be higher than the values obtained in the V&V study where the iterative errors were kept minimal. The comparison error for the g1, g2 and g6 at the even keel condition in Table 8 varies 0.27%, 0.33%, and 0.33% from the comparison errors obtained from the verification study, respectively. Considering that these differences in the comparison errors are 5, 5, and 20 times smaller than the discretisation errors of the corresponding grids estimated in the verification study (see Section 6.3), performing the computations with fewer time steps and non-linear iterations are considered reasonable. Since the calculation of the relative change in resistance or propulsion characteristics between trimmed conditions and the even keel (e.k.) loading is sufficient for trim optimisation study, the calculation of the absolute values is not as critical. As a result of less stringent convergence, the computational time is reduced by 3 to 4 times compared to the computations for the verification study, while the comparison error remains reasonably similar. Therefore, the computations for the rest of the study are performed with the less stringent convergence tolerances.

The trim by the bow loading condition (H+1.5m) exhibits similar $E\%D$ values to the even keel condition. On the other hand, the trim by the bow indicates about three per cent larger comparison error, which suggests the presence of modelling errors, more than the even keel condition for the two finest grids. The comparison error seems to decrease from even keel to trimming by the stern for the g6 grid. Considering the increased complexity of the flow, this reduction in $E\%D$ for g6 is likely due to numerical and modelling errors cancelling each other. Therefore, g6 is deemed to be too coarse to continue with the rest of the simulations. The g1 and g2 show similar comparison errors for the three loading conditions. The mean absolute value of the comparison errors for the three loading conditions for g1, g2, and g6 are 4.01%, 4.16%, and 9.55%, respectively. Therefore, the second finest grid, g2, provides nearly the same accuracy while reducing the computational effort by more than half compared to g1. Besides capturing the absolute values of the resistance force, the relative change in the resistance between trimmed conditions and even keel (e.k.) loading is even more relevant for the trim optimisation study. All three grids showed similar trends between the trimmed and zero trim conditions. Considering the numerical errors and complexity of the flow, the second finest grid is the right compromise between the computational cost and accuracy. Therefore, further computations are computed with the corresponding AGR threshold of g2 in the model and the full scale.

Table 8
Comparison errors for different AGR thresholds corresponding to the g1, g2 and g6.

Loading	$E(g1)\%D$	$E(g2)\%D$	$E(g6)\%D$
H-1.5m	2.99	3.43	−1.20
H	0.37	0.27	−4.06
H+1.5m	−0.38	−0.67	−4.61

7. Comparison between the towing tank tests and different CFD methods

7.1. Resistance

The trim optimisation test scope of two displacements, three trims, and three speeds is discussed in this section. The towing tank test results with the measurement uncertainties (Section 5.1), free-surface RANS computations (Section 3.3), and the combination of double-body RANS (Section 3.1) and potential flow (Section 3.2) computation results were used for the comparison. The change in the quantity of interest between the trimmed and the even keel conditions for each displacement and speed is calculated; for example, for the resistance force,

$$\Delta R_{TM} = \frac{R_{TM}(trim) - R_{TM}(trim = 0)}{R_{TM}(trim = 0)} \times 100\ , \tag{16}$$

where ΔR_{TM} is the relative change in resistance force in a given trim condition ($R_{TM}(trim)$) in per cent of the resistance of the zero trim condition ($R_{TM}(trim = 0)$).

Note that even though this section only presents model tests and computations performed at the model scale, the vessel's speed is always indicated with the corresponding full-scale speed in knots. This decision is based on the fact that the same full-scale speed at different loading conditions cannot be addressed with a single Froude number because the waterline lengths vary significantly between the loading conditions.

7.1.1. Towing tank tests

The results of the trim optimisation towing tank tests are presented in Fig. 7. The measured data from the tests are represented by black markers, with measurement uncertainties indicated by the accompanying error bars. Each sub-figure in Fig. 7 illustrates the relative change in resistance under trimmed conditions compared to the even keel condition for a specific displacement and speed, as noted in the captions. An overall analysis of the ΔR_{TM} trends in Fig. 7 suggests that the potential for reducing resistance by trimming at the bow is negligible in 19 kn, modest at in 17 kn and somewhat limited at 15 kn. Conversely, trimming the vessel by stern results in increased resistance across all displacements and all speeds. The potential gains are overshadowed by the possible resistance penalties incurred when operating the vessel under non-optimal conditions, amounting to as much as 15%.

A comparison between the light (top row) and the heavy displacements (bottom row) at their respective speeds reveals little difference, despite the disparity in displacement volumes of approximately 10%. This similarity can be attributed, in part, to the forebody design. The bulbous bow was optimised for narrow operational conditions due to its length and the positioning of the bulb's volume centre relatively close to the water surface and the forward end of the bulb close to the tip. Consequently, the loading conditions where the bulb is too close to the water surface (trim < 0) and low Froude numbers (Fr) result in unfavourable wave patterns, occasionally leading to breaking waves, as observed in Fig. 8(d). Other characteristics of the forebody design, such as significant flare and a relatively blunt waterline entrance angle above the design waterline, cause the water surface to rise along hull as a thin sheet (heights up to 30% of the draught from the water surface) before rolling on the sides when trimmed by the bow (trim > 0) at higher speeds, as depicted in Fig. 9(d). The similarity in ΔR_{TM} trends for each speed in different displacements can largely be explained by

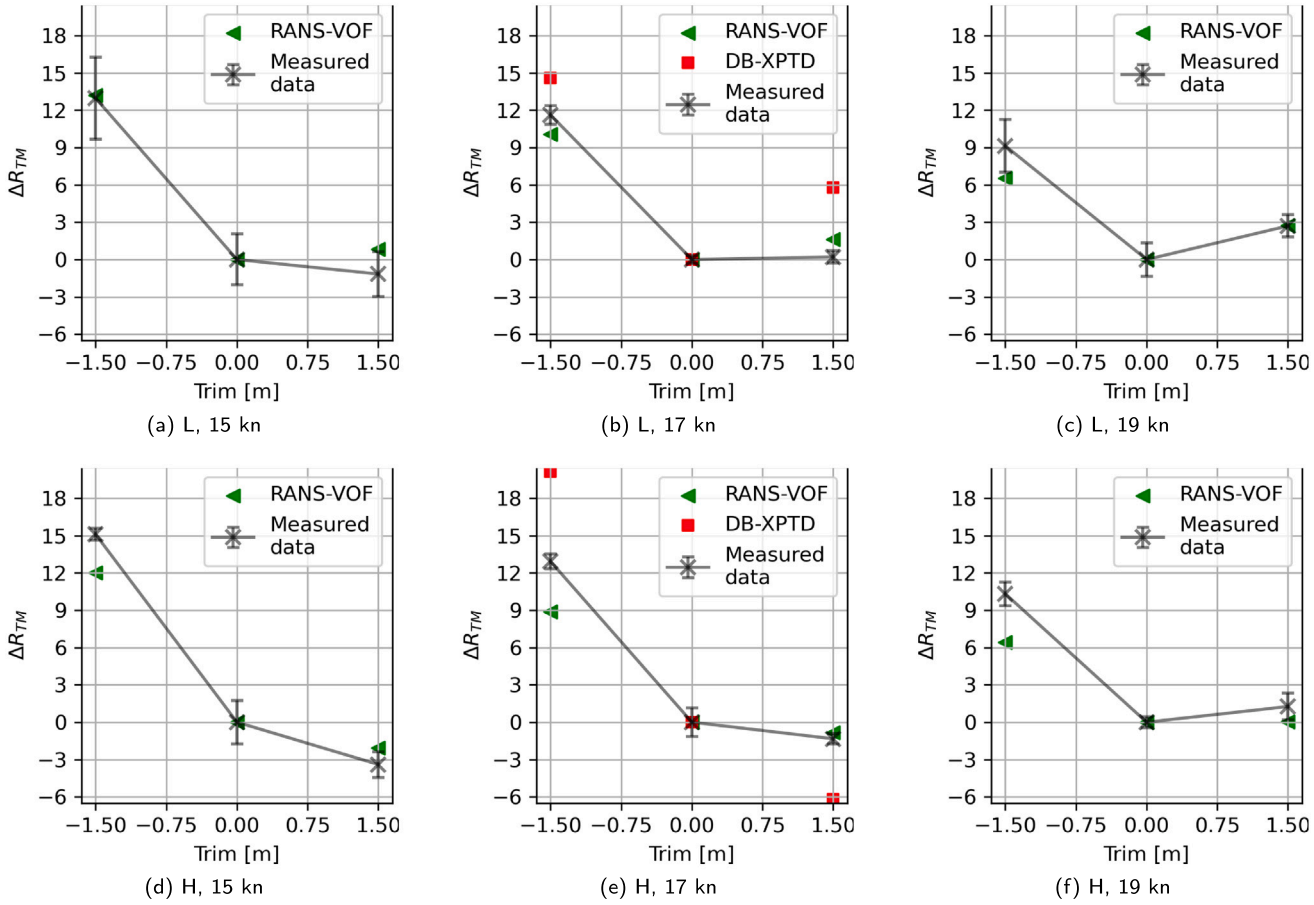

Fig. 7. Trim optimisation results of resistance from the towing tank measurements, RANS-VOF computations and the combined DB-XPTD simulations.

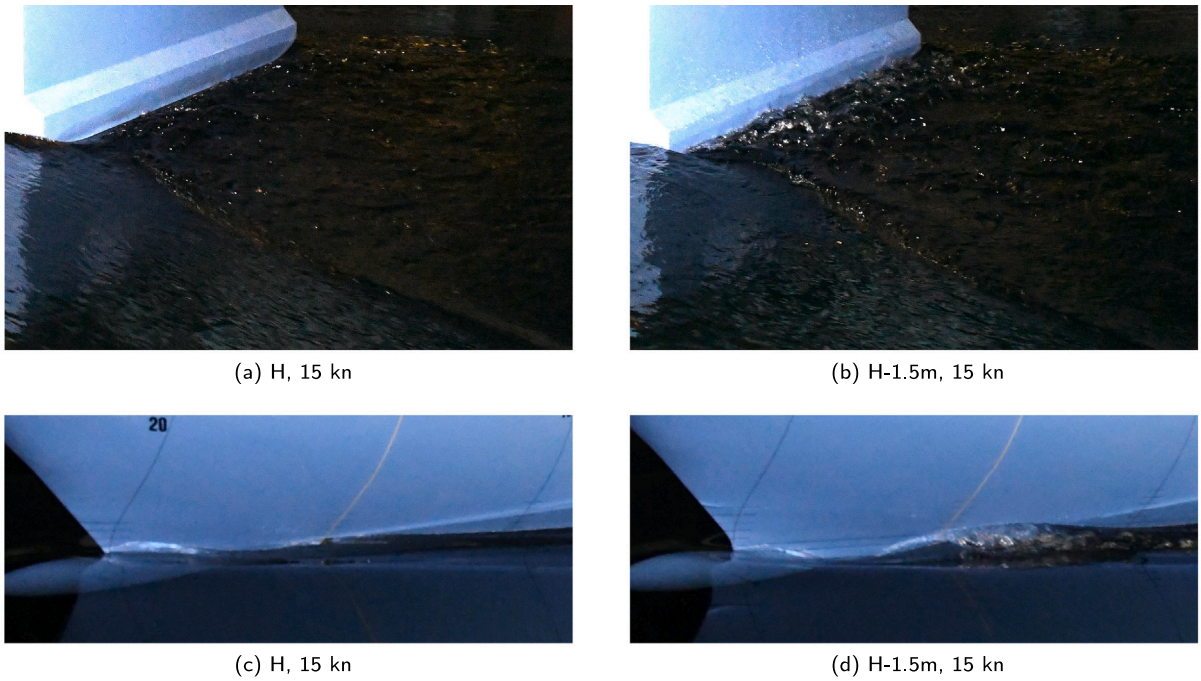

Fig. 8. Towing tank resistance tests from the bow and stern views.

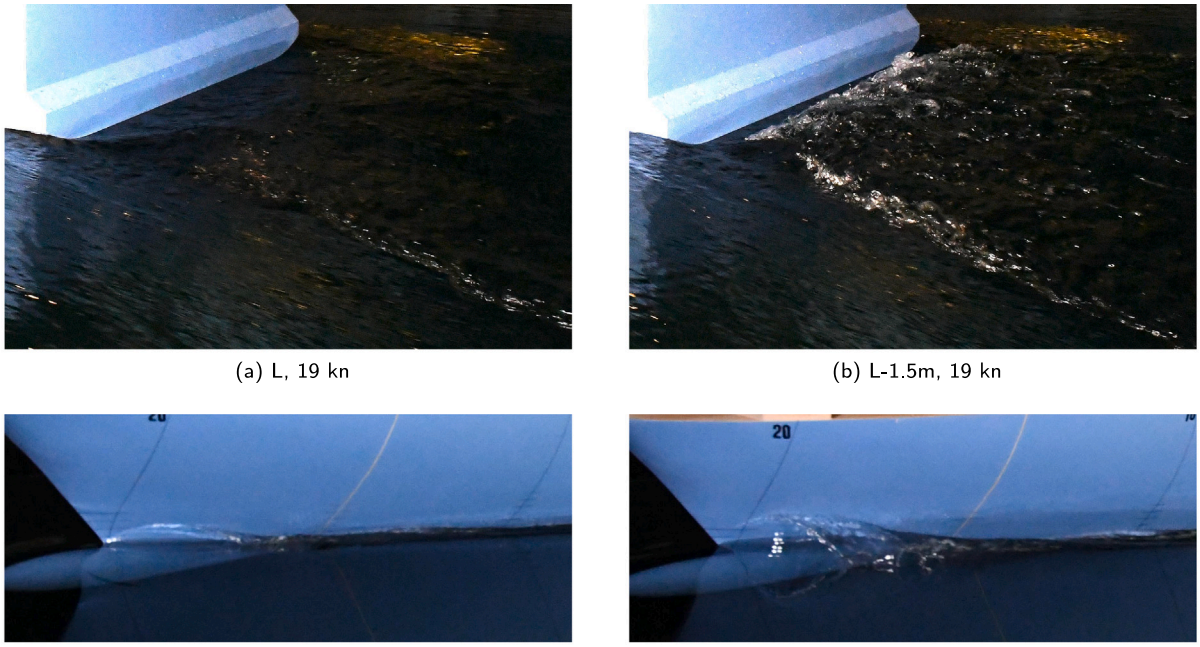

(a) L, 19 kn (b) L-1.5m, 19 kn

(c) L, 19 kn (d) L+1.5m, 19 kn

Fig. 9. Towing tank resistance tests from the bow view.

the fact that similar flow phenomena, albeit with varying intensities, are observed in both displacements, rather than entirely distinct wave patterns.

The flow regime behind the transom exhibits significant variation depending on trim and speed conditions, including the dry-transom, wetted-transom and partially dry-transom flows observed in the towing tank tests. However, the case of regular transom flow (Larsson and Raven, 2010), where the lower edge of the transom is above the still water level and waves smoothly leave the hull, was not observed, as the wave crest at the stern consistently exceeded the transom edge at all conditions. Conversely, the dry-transom flow, where the flow smoothly leaves the transom edge tangential to the buttocks, was only observed at the highest speed (19 kn or $Fr = 0.21$) in the light displacement even keel condition, as depicted in Fig. 9(a), as well as in and both displacements with trim by the bow conditions. The majority of the other trim conditions and speeds resulted in partially dry-transom flows.

To sustain the dry-transom flow, the pressure at the transom edge must be equal to the atmospheric pressure (Larsson and Raven, 2010). Consequently, decreasing the speed or increasing the transom submergence through trimming increases the required hydrodynamic pressure for achieving dry-transom flow. This leads to an increase of the upward curvature of the streamlines behind the transom. Eventually, the steepening streamlines, coupled with momentum deficit in the boundary layer, results in the longitudinal velocity to disappear (Starke et al., 2007). As a consequence, spilling wave breakers emerge between the transom and the first wave crest, as seen in Fig. 9(b). Further increases in transom submergence or speed reduction will cause the spill breakers to reach the transom, leading to the formation of a recirculation region behind the transom, categorised as wetted-transom flow, as observed in Fig. 8(b). The wetted transom flow regime only occurred with the high displacement trim by the stern and the slowest speed ($Fr = 0.166$ and $Fr_{tr} = 2.75$).

7.1.2. Double-body RANS and potential flow combined (DB-XPTD)

This trim optimisation method combines RANS-DB and potential flow computations (XPTD). The computations were limited to only 17 kn, as the success of this method in replicating the towing tank test results was limited. RANS-DB and potential flow computations were performed as explained in Section 3.1 and Section 3.2, respectively. As previously mentioned, not all loading conditions at 17 kn result in wetted-transom flow, which is required for the double-body assumption (Korkmaz et al., 2022). One way to address this issue is to replace the transom with a pseudo extension of the stern overhang that connects the flat free surface and the hull. In cases where pseudo-extension wall cells are classified as the slip boundary condition and excluded in the integration of the viscous pressure force, double-body computations can be used for a dry-transom condition. However, at 17kn, the flow regime behind the transom is partially dry-transom, which is not significantly different from the wetted-transom flow condition. Therefore, the double-body assumption is considered valid.

The potential flow computations (XPTD) for the trim by the bow conditions presented some challenges as the free surface "just skimmed" the stern overhang, leading to numerical difficulties. However, the even keel and the trim by the stern conditions were computed using the XPTD method without any issues. The total resistance coefficient is approximated by summing the viscous resistance from the DB RANS computations and the wave resistance from the potential flow computations. This total resistance coefficient is denoted as "DB-XPDT" and is shown with red square markers in Figs. 7(b) and 7(e). It is important to note that the total resistance from the "DB-XPTD" is an approximation, as the viscous resistance from the double-body computations neglects the viscous effects due to the free-surface deformation, and the wave resistance is obtained without accounting for the viscous effects and breaking waves.

The resistance trends from the DB-XPDT method are correct in a general sense for the trim by the stern. However, ΔR_{TM} predictions are 3% and 7% higher than the measurements for the light and heavy displacements, respectively. ΔR_{TM} predictions for the trim by the bow are inconsistent, with a considerably high deviation from the towing tank measurements. To understand the source of this deviation, the total resistance from the DB-XPTD method is decomposed into frictional (R_{FM}), viscous pressure (R_{PVM}), and wave-making resistance (R_{WM}). The first two resistance components are obtained from the DB RANS computations, and their summation yields the viscous resistance R_{VM}. As shown in Table 9, the relative change in resistance components and

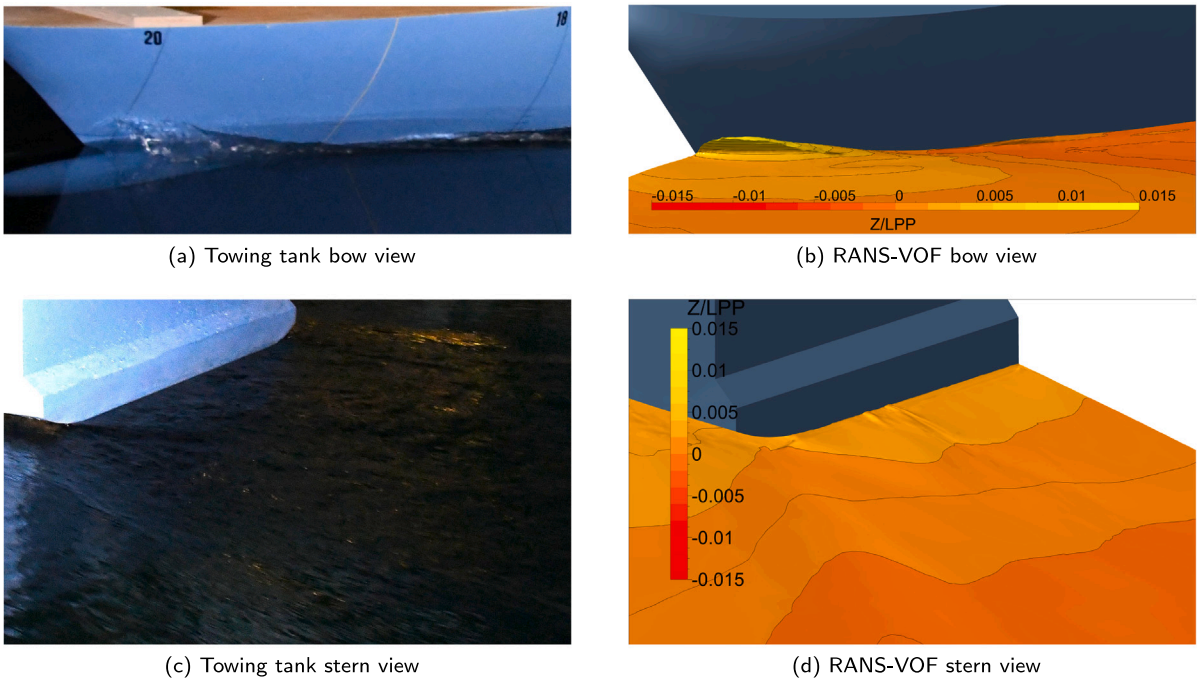

(a) Towing tank bow view

(b) RANS-VOF bow view

(c) Towing tank stern view

(d) RANS-VOF stern view

Fig. 10. Wave pattern from the towing tank resistance tests and RANS-VOF computations in model scale, trim by the bow condition (H+1.5m) at 17 kn.

Table 9
The relative change of resistance components and the total resistance between the trimmed and even keel conditions from DB-XPDT computations.

Loading condition	ΔR_{FM}	ΔR_{PVM}	ΔR_{VM}	ΔR_{WM}	ΔR_{TM}
L-1.5m	1.1	47.4	4.3	447.8	14.6
L+1.5m	−0.9	−0.2	−0.8	282.7	5.8
H-1.5m	−0.5	87.6	6.7	333.3	20.1
H+1.5m	−6.2	−20.9	−7.4	21.1	−6.2

the total resistance between the trimmed and even keel conditions are calculated in a similar manner to Eq. (16). The double-body computations reveal a sharp increase in viscous pressure resistance with trim by the stern, which is attributed to increased transom submergence in both displacements. Conversely, the L+1.5m condition shows a marginal change in R_{PVM} as the transom remains outside of the water in both L and L+1.5m conditions. Finally, the significant drop in viscous resistance from H to H+1.5m is primarily due to a decrease in the frictional resistance component, as most of the stern overhang lifts out of the still water surface in the double-body computations. As observed in the model tests, the wave crest at the stern was large enough to submerge the entire stern overhang, so the substantial reduction in ΔR_{FM} and consequently in ΔR_{TM} for the H+1.5m loading condition is not realistic but rather a consequence of the double-body assumption.

The change in wave resistance, ΔR_{WM}, in trimmed conditions is much more significant than the other resistance components and varies between 21% to 448%. Given the complexity of the breaking waves, the thin sheet wave observed at the forebody, and the spilling wave breakers seen at the aft body, it is challenging, if not impossible, for potential flow to accurately model the flow phenomena in the trimmed conditions for this hull. The resulting ΔR_{WM} values are too large and cause an overshoot in ΔR_{TM} in L-1.5m, L+1.5m, and H-1.5m loading conditions.

7.1.3. RANS-VOF-resistance

The final method for trim optimisation is the RANS-VOF method. ΔR_{TM} values are presented in Fig. 7 as green triangle markers. It can be argued that ΔR_{TM} predictions accurately replicated the towing tank measurements, as the mean of the absolute values of the differences between ΔR_{TM} predictions from the RANS-VOF and model tests is only 1.82% (excluding zero trim conditions).

As seen in Fig. 7, the RANS-VOF predictions are particularly successful in predicting the trim by the bow, where the transom submergence is decreased compared to the even keel condition. The wave pattern of the H+1.5m condition is visualised from the images of the towing tank experiments and the RANS-VOF in Fig. 10. The flow behind the transom is far less complicated than in the even keel and the trim by the stern conditions, as the wake behind the transom is smooth, free from recirculating flow and spill breakers as seen in Fig. 10(c). The computed wave pattern from the RANS-VOF method closely resembles the towing tank tests, as seen in Fig. 10(d). This result is expected since modelling assumptions such as time averaging and turbulence modelling should not prevent capturing the flow characteristics behind the transom.

On the other hand, the flow phenomenon at the bow differs from the stern in the H+1.5m condition due to its unsteady nature. As seen in Fig. 10(a), a thin sheet of water climbs up the hull rapidly and reaches approximately $Z/L_{pp} = 0.015$ (Z denotes water surface elevation with respect to the still water level) in the towing tank test. Then, the quasi-stable thin sheet of water rolls sideways to meet with the water surface again. The thin sheet of water is, in general, captured by the RANS-VOF method, as seen in Fig. 10(b); however, the wave height is slightly smaller ($Z/L_{pp} = 0.012$), and the rolling of the water sheet sideways is missing in the CFD. The following diverging wave initiated between stations 19 (95% of L_{pp} from the AP) and 18 is also steep and breaking in the towing tank tests. However, the RANS-VOF method predicts the diverging waves with significantly less steepness and breaking.

The difference of ΔR_{TM} between the towing tank measurements and RANS-VOF predictions varies from 0.2% to 4% in the trim by the stern conditions. As seen in Fig. 7, the light displacement was predicted more accurately than the heavy displacement in aft trim conditions. As the transom and the bow are submerged more in the light displacement than in the heavy displacement, it is expected that the severity of breaking waves in the forebody, and spill breakers and eddies in the aft body will increase. Therefore, numerical and modelling errors (time averaging, turbulence modelling) significantly affect prediction accuracy. The numerical errors were investigated in Section 6.5, and it was

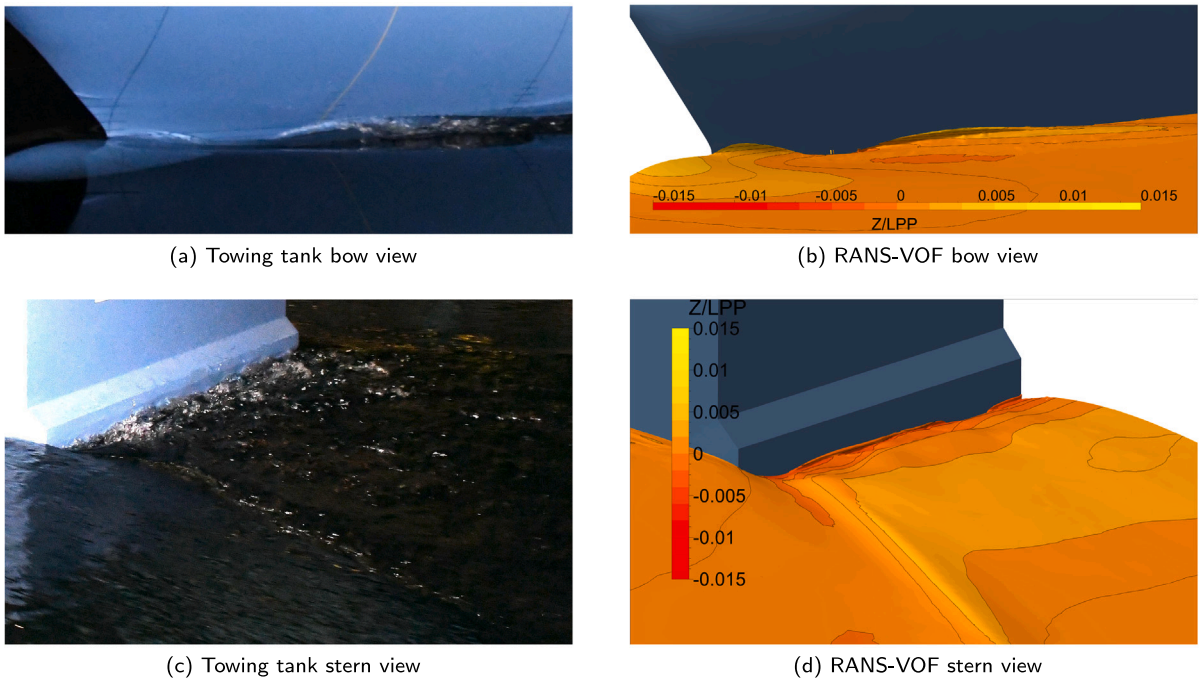

(a) Towing tank bow view (b) RANS-VOF bow view

(c) Towing tank stern view (d) RANS-VOF stern view

Fig. 11. Wave pattern from the towing tank resistance tests and RANS-VOF computations in model scale, trim by the stern condition (H-1.5m) at 17 kn.

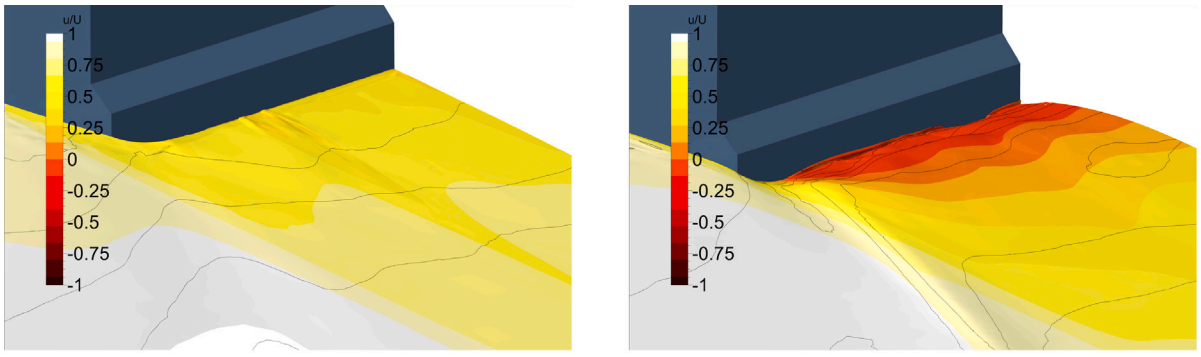

(a) H+1.5m (b) H-1.5m

Fig. 12. Non-dimensional longitudinal velocity on the free surface from RANS-VOF computations in model scale at 17 kn.

concluded that increasing the number of cells (i.e., decreasing the AGR threshold) helps only marginally; therefore, modelling errors should be the main reason for the prediction accuracy. The wave pattern of the H-1.5m condition is presented in Fig. 11 with the photographs from the towing tank experiments and the post-processed images from the RANS-VOF computations.

The wave pattern at the forebody in Fig. 11(a) shows the effect of the bulbous bow being too close to the water surface in aft trim conditions. As it is easier to understand the surface elevation in the post-processed image from RANS-VOF in Fig. 11(a), the large wave crest precisely on top of the bulb can be identified. The interpolation of the bulb and the bow stem wave systems results in a sharp wave trough between Station 19 (where the white trip wire is mounted) and 20 (the vertical line at the fore perpendicular). The wave crest, followed by the sharp and deep wave trough, then breaks at Station 19 (95% of L_{pp} from the AP), initiating diverging waves. As seen in Fig. 11(a), RANS-VOF can capture the forebody waves, except the breaking waves were not fully resolved.

The free surface and flow structures at the stern are presented in Fig. 11(c) for the trim by the stern condition. Contrary to the trim by the bow at the same displacement and speed (Fig. 10(c)), the flow behind the transom is complicated with unsteady flow features such as recirculation, spilling wave breakers, and eddies in the aft trim conditions. In addition, a steep diverging wave system is radiated from the corner of the transom. The transom wake is followed by significantly large transverse waves, which RANS-VOF predicts well. As seen in Fig. 11(d), the free surface predicted by RANS-VOF is smooth and missing the spilling wave breakers and eddies visible on the surface from the towing tank image (Fig. 11(c)). Not being able to replicate such complex flow structures is a direct consequence of the cost-effective grid resolution and modelling methods (time averaging, RANS method coupled with k−ω SST turbulence model). However, ΔR_{TM} between the towing tank measurements and RANS-VOF predictions shows that the integrated forces in aft trim conditions are predicted with acceptable accuracy, as seen in Fig. 7.

As seen in Fig. 12, the wake behind the transom is visualised by plotting the non-dimensional longitudinal velocity contours (u/V where u is longitudinal velocity and V is the free stream velocity) at the free surface. The negative u/U values indicate that water on the free surface is moving in the same direction as the model, trailing the hull. The contour lines in Fig. 12 mark the Z/L_{pp} levels with the an interval of 0.001, and they are inherited from the earlier surface elevation plots

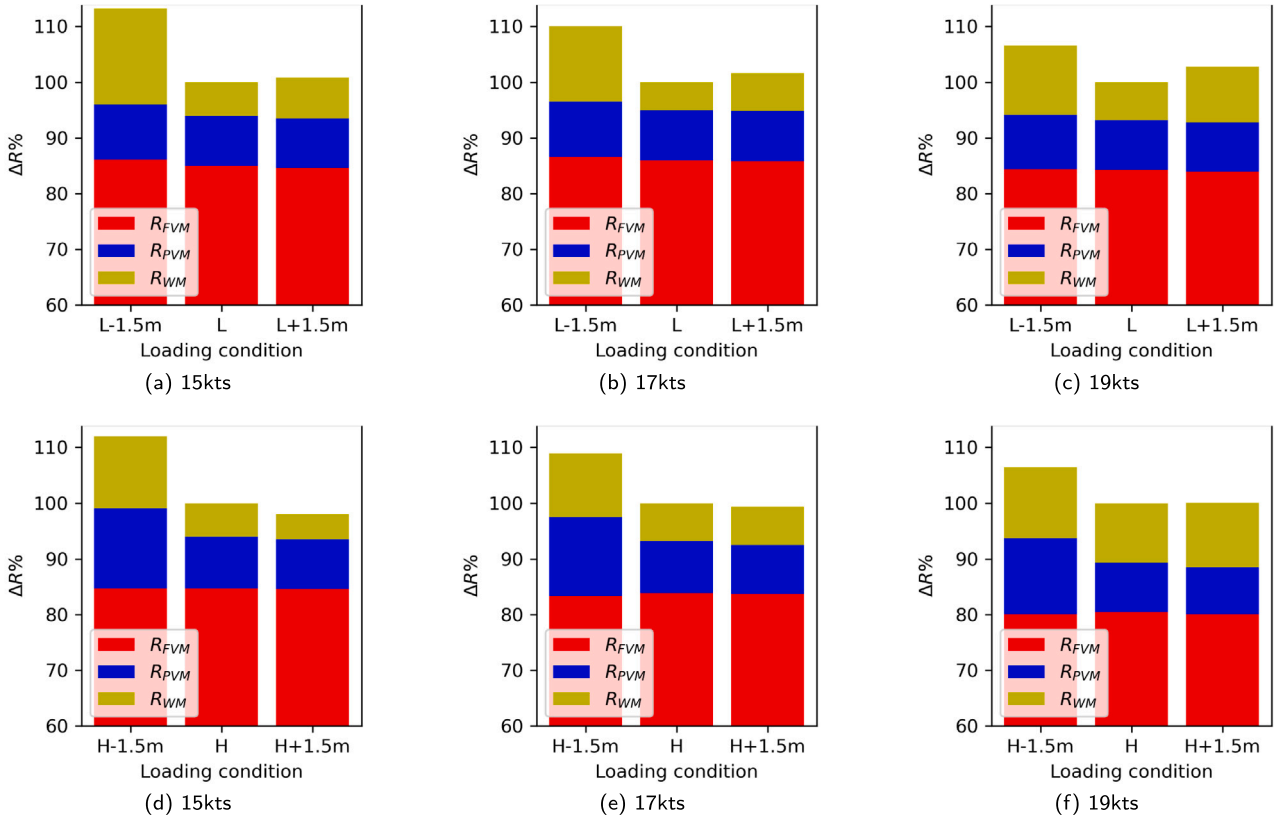

Fig. 13. The change of resistance components R_{FVM}, R_{PVM}, R_{WM} with respect to speed and loading condition.

(e.g., Fig. 11(d)) to maintain the sense of wave formation on the free surface. As mentioned earlier, the H+1.5m condition at 17 kn had a definitive dry-transom. As seen in Fig. 12(a), the wake behind the transom leaves the hull smoothly with some momentum loss due to the boundary layer formed along the hull and the appendages. However, the H-1.5m condition at 17 kn with the partially dry-transom shows flow trailing the hull ($u/V < 0$) immediately behind the transom, as seen in Fig. 12(b). In fact, the spill breakers (white and irregular protruding patches on the free surface) observed in the towing tank tests (Fig. 11(a)) mostly emerge in the recirculation region, which is marked with negative u/U values in the CFD computations. Therefore, it can be argued that even though CFD could not model some of the flow details observed in the towing tank tests, the main flow features, such as the transom dryness, recirculation zone, and wave pattern, are captured by the RANS-VOF model accurately.

7.1.4. Decomposing the total resistance coefficient to understand the gains and losses in trimmed conditions

The trim optimisation results for the total resistance and the flow features observed at different trim conditions were discussed in Sections 7.1.1 and 7.1.3. This section divides the total resistance coefficient into its constituent parts to identify the sources of gains or losses in each loading condition and speed. From a free-surface RANS computation, the total resistance coefficient is obtained

$$C_{TM} = C_{FVM} + C_{PM} \ , \tag{17}$$

where C_{FVM} is the viscous frictional resistance coefficient and C_{PM} represents the pressure coefficient. C_{FVM} includes flat plate friction (C_{F0}) and form effect friction components, while C_{PM} term constitutes viscous pressure (form effect pressure C_{PVM}) and wave making (wave pattern and wave breaking, C_{WM}) terms (Larsson and Raven, 2010). Even though obtaining C_{PVM} and C_{WM} components separately is not possible through free-surface RANS computations, the form factor approach (Hughes, 1954) can be adopted from ITTC extrapolation procedures to approximately separate C_{PM} from the RANS-VOF computations. The viscous pressure resistance

$$C_{PVM} = C_{F0} \times k \ , \tag{18}$$

where k is the form factor. According to ITTC (2021g) and Hughes (1954), the frictional resistance coefficient should be derived from a flat plate but using C_{FVM} from RANS-VOF computation is considered as a reasonable approximation since the form effect friction component in C_{FVM} will be of a similar size (approximately 3%–4% of C_{FVM}) in all loading conditions. The form factors for each loading condition are adopted from the Prohaska method (Prohaska, 1966), supported by the double-body computations (ITTC, 2021g; Korkmaz et al., 2021a). Consequently, the wave resistance is

$$C_{WM} = C_{PM} - C_{PVM} \ . \tag{19}$$

The total resistance coefficients, C_{FVM}, C_{PVM}, and C_{WM} in the trimmed conditions are converted back to forces and are presented in Fig. 13. Similar to previous plots (e.g. Fig. 7), the total resistance and its components ($R_{TM} = R_{FVM} + R_{PVM} + R_{WM}$) in the trimmed conditions are presented relative to the even keel condition for each speed and the displacement. In addition, R_{FVM}, R_{PVM}, and R_{WM} are represented as percentages of R_{TM} for each condition. The y-axis of the stacked bar plots in Fig. 13 starts from 60% and to enhance the visualisation of the minor differences between the loading conditions. For instance, in Fig. 13(a), viscous friction resistance accounts for 85% of the R_{TM} in the L condition. Moreover, the total resistance coefficient in the L-1.5m condition is 13% higher than in the L condition, and R_{WM} in the L-1.5m condition is nearly three times the size of the wave resistance in the L condition at 15kn.

As depicted in Fig. 13, the proportion of R_{VM} in the total resistance decreases with the increasing speed, as the viscous effects are inversely proportional to the Reynolds number, and wave resistance increases

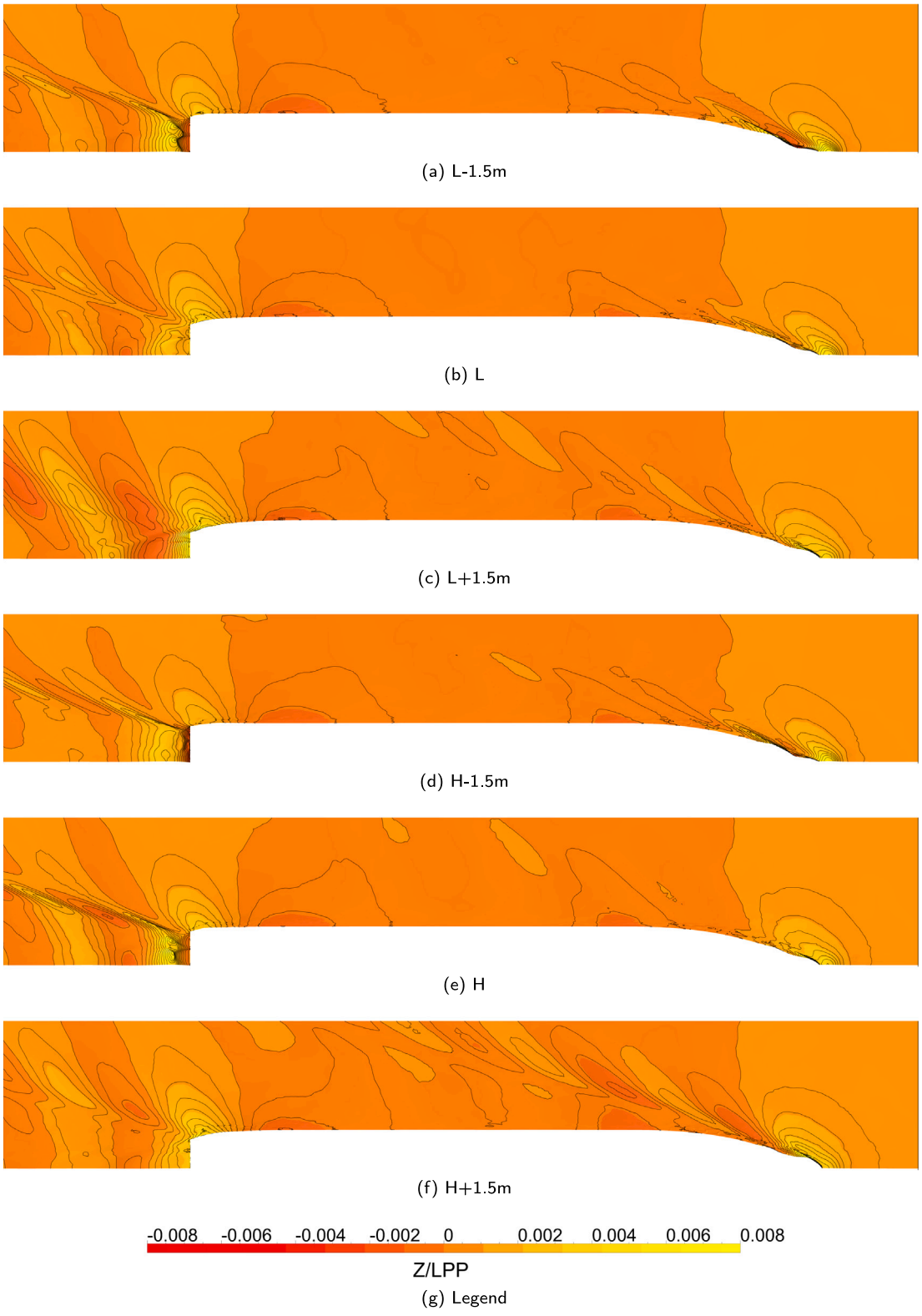

Fig. 14. Wave pattern contours for different loading conditions at 17kn.

its relative size with an increasing Froude number. Furthermore, the change in R_{VM} between the different conditions at the same speed and displacement is limited. Consequently, the frictional resistance component can be considered predominantly a neutral term in this trim optimisation.

The viscous pressure resistance R_{PVM} remains relatively consistent in the light displacement for all speeds and trim conditions. However, R_{PVM} undergoes significant changes in the heavy displacement. As observed in Fig. 13(d), the increase in R_{PVM} from the even keel to the H-1.5m condition (trim by stern) is the most substantial. This is

attributed to the H-1.5m loading condition having the greatest transom submergence and the smallest Froude number.Consequently, the transom remains mostly submerged (see Fig. 8(b)), leading to a resistance increase due to the pressure drop at the transom caused by the recirculating flow, which is reflected in R_{PVM} component (Korkmaz et al., 2022). As demonstrated in Korkmaz et al. (2019), R_{PVM} is relatively insensitive to the mild trim changes when the main flow characteristics, such as flow separation, wake behind the transom, and eddy making, remain similar. This can be observed between the even keel and L+1.5m conditions, as the R_{PVM} term remains similar with respect to the frictional resistance term for each speed and displacement, as shown in Fig. 13.

The wave resistance R_{WM} comprises wave pattern and wave-breaking resistance components. As illustrated in Fig. 13, R_{WM} is the resistance component that exhibits the most significant variation with respect to the trim conditions, as also concluded by Lemb Larsen et al. (2012). The wave patterns at 17 kn are presented in Fig. 14 for all loading conditions. Beginning with the even keel conditions (Figs. 14(b) and 14(e)), it is evident that neither condition radiates significant diverging wave systems from the forebody. Mild breaking waves are observed in the light displacement with zero trim due to the bulb being too close to the water surface. Conversely, the bow wave height is higher than in the heavy displacement and even keel condition compared to the light loading, but no significant breaking waves are observed in the forebody. Trimming by the bow eliminates the breaking waves altogether in both displacements but triggers diverging waves, as seen in Figs. 14(c) and 14(f). Trimming by the stern brings the bulb closer to the free surface, increasing the breaking wave height. In conclusion, the wave patterns at the forebody do not differ significantly between the two displacements with trimming by the bow or the stern.

On the other hand, the wave patterns for the even keel conditions at the aft body differ significantly between the light and heavy displacement, as the H condition has a substantial transom submergence. Due to the transom submergence, the transverse waves are more prominent in the H condition than in the L loading, and the diverging waves break in the heavy displacement, unlike the light loading condition. Further increasing the transom submergence by aft trim triggers breaking diverging waves in the light displacement, but the wave heights behind the transom are slightly reduced in the heavy displacement. Trim by the bow improves the wave resistance in the aft for heavy displacement, as the transom becomes mostly dry, but increases the wave heights in the light loading.

In conclusion, trimming by the stern worsens the overall wave pattern as the bulb gets too close to the water surface and transom submergence increases. However, gains and losses due to the changes in wave patterns from the forebody and the aft body are not always in the same direction. Therefore, the change in R_{WM} is significantly less for the bow trim compared to the aft trim, as seen in Fig. 13.

7.2. Self-propulsion

This section presents the results of the self-propulsion towing tank tests and computations. The same trim optimisation test conditions as those in the resistance tests (see Section 7.1) were employed; two displacements, three trims, and three speeds. The delivered power in the model scale was calculated from the measured torque and propeller rotation rate, with their measurement uncertainties were predicted as explained in Section 5.1. Compared to the measurements, only the RANS-VOF method (Section 3.3) method was used, as the combination of double-body RANS and potential flow computation results could not accurately predict the resistance trends. The change in delivered power between the trimmed and the even keel conditions for each displacement and speed is calculated

$$\Delta P_{DM} = \frac{P_{DM}(trim) - P_{DM}(trim = 0)}{P_{DM}(trim = 0)} \times 100 \ , \tag{20}$$

where $P_{DM}(trim)$ is the delivered power at a given trim condition and $P_{DM}(trim = 0)$ represents the power at the zero trim condition.

Table 10
Trim trends at 17kts for adjusted total resistance from the resistance tests ($\Delta(R_{TM} - R_a)$), and thrust (ΔT_M), torque (ΔQ_M), propeller turning rate (Δn_M) and delivered power (ΔP_{DM}) from the self-propulsion tests.

Loading	Resistance test	Self-propulsion test			
	$\Delta(R_{TM} - R_a)$	ΔT_M	ΔQ_M	Δn_M	ΔP_{DM}
L-1.5m	16.7	15.0	14.0	5.2	19.9
L+1.5m	0.5	0.1	0.3	−1.0	−0.7
H-1.5m	17.6	16.5	15.3	5.1	21.2
H+1.5m	−2.4	−3.5	−4.0	−2.1	−5.9

7.2.1. Towing tank tests-self-propulsion

The self-propulsion results from the trim optimisation towing tank tests are presented in Fig. 15. The measured data from the tests are denoted by black markers, with the approximated measurement uncertainties indicated by the error bars. Each sub-figure in Fig. 15 represents the relative change in delivered power (ΔP_{DM}) under the trimmed conditions with respect to the even keel condition for a specific displacement and speed. A comparison between the total resistance obtained from resistance tests (Fig. 7) and the delivered power from self-propulsion tests (Fig. 15) shows that trim trends are consistent across most of the loading conditions and speeds. In both sets of tests, trimming by the stern leads to high penalties, while trimming by the bow can result in gains or losses depending on the displacement and speed compared to the even keel condition.

The most notable distinction between the resistance and self-propulsion tests is that the amount of possible gains or losses by trimming the hull seems to be much larger in self-propulsion. For instance, at the H-1.5m condition and 15 kn, ΔR_{TM} is 15% and ΔP_{DM} is 24%. This disparity is not solely attributable to propulsive efficiency but is largely influenced by the differences in the test setups. As required by the ITTC-78 method, the self-propulsion tests were carried out with a towing force (R_a), which is unloading the propeller in the tests to account for the difference between frictional resistance coefficients in the model and full scale, and the roughness allowance. In other words, in self-propulsion tests, the propeller thrust does not entirely counteract the resistance observed in the resistance test; instead it is supplemented by a towing force. Consequently, the effective power, as seen in Fig. 7 ($P_{EM} = V_M \times R_{TM}$, where V_M represents the model scale velocity and R_{TM} is the resistance from the resistance test), and the power in self-propulsion test, as shown in Fig. 15 ($P_{DM} = 2\pi n_M \times Q_M$), cannot be directly compared.

For a fairer comparison, the towing force applied during the self-propulsion test needs to be subtracted from the total resistance obtained in the resistance test. Table 10 displays the trim trends at 17 kn for the adjusted total resistance from the resistance tests ($\Delta(R_{TM} - R_a)$), and thrust (ΔT_M), torque (ΔQ_M), propeller turning rate (Δn_M) and delivered power (ΔP_{DM}) from the self-propulsion tests. The change in thrust from the even keel to the aft trim conditions (L-1.5m and H-1.5m) is lower than the adjusted total resistance ($\Delta(R_{TM} - R_a)$), indicating a lower thrust deduction in the aft trim condition compared to the even keel. However, the sharp increase in the propeller turning rate (approximately 5%) in the aft trim condition compared to the even keel indicates that the wake fraction is also decreased. The hull efficiency

$$\eta_H = \frac{1 - t}{1 - w_{TM}} \ , \tag{21}$$

where t represents the thrust deduction and w_{TM} is the wake fraction at the model scale. The hull efficiency is reduced from even keel condition to aft trimming. In addition, trimming the vessel by the stern causes a shift in the propeller loading condition (K_{TM}/J_{TM}^2, where K_{TM} is the non-dimensional thrust coefficient, and J_{TM} is the advance ratio) due to the sharp increase in resistance, resulting in a drop in the propeller efficiency. The relative rotative efficiency shows limited change when the vessel is trimmed by the stern; however, the torque increase closely follows the thrust trends. As the delivered power is proportional to

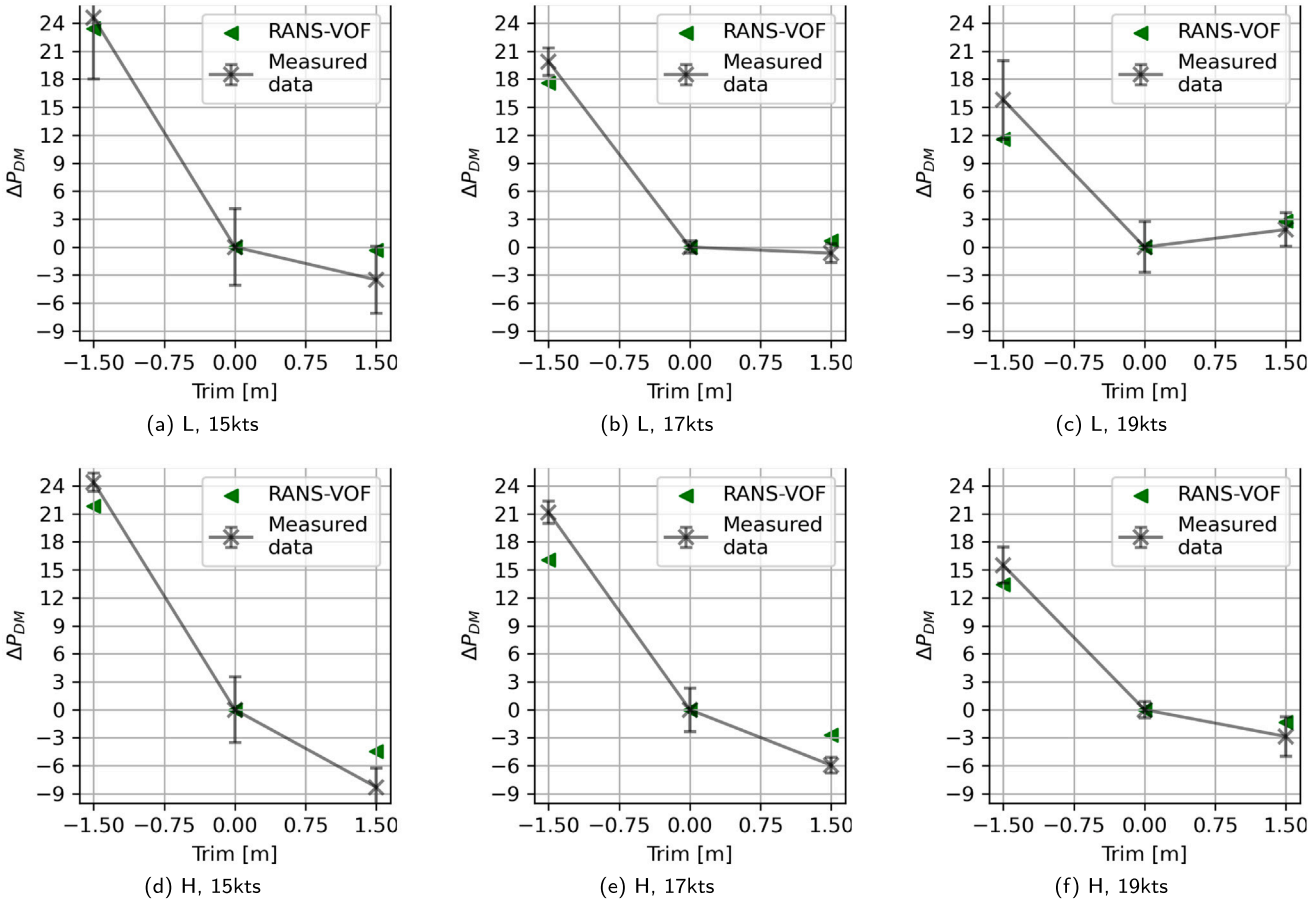

Fig. 15. Trim optimisation results of delivered power from self-propulsion from the towing tank measurements and RANS-VOF computations.

the product of torque and propeller turning rate, ΔP_{DM} ends up being larger than the change in adjusted resistance. In other words, the adverse effects of trimming by the stern are exacerbated by reduced propulsive efficiency.

As shown in Table 10, the trim by the bow leads to lower increase in thrust in the L+1.5m condition and a greater decrease in the H+1.5m condition due to reduced thrust deduction in both cases. In contrast to trim by aft, the wake fraction increases during bow trimming, resulting in higher hull efficiency compared to the even keel condition. The propeller and relative rotative efficiencies exhibit relatively minor sensitivity to bow trimming. Consequently, total efficiency increases with trimming by the bow, particularly in heavy displacement, increasing the potential for gains in self-propulsion compared to the resistance.

The findings at other speeds further underscore the differences between self-propulsion and resistance tests. While resistance tests provide a general indication of trim trends, an accurate quantification of optimal trim and potential gains or losses requires self-propulsion tests, which offer a more precise reflection of actual ship operation.

7.2.2. RANS-VOF-self-propulsion

The towing tank test conditions for self-propulsion, including the towing force, were computed using the RANS-VOF method, and the ΔP_{DM} values are presented in Fig. 15. In the plots, these computation results are denoted as "RANS-VOF" and represented with green triangle markers. Similar to the total resistance predictions in the resistance tests (Fig. 7), the RANS-VOF method accurately replicated the trim trends for delivered power from the towing tank. The mean of the absolute values of the differences between ΔP_{DM} predictions from the RANS-VOF method and model tests is 2.62% (excluding zero trim conditions). Considering the simple propeller model employed in the self-propulsion computations, the overall prediction accuracy of the trim trends is remarkably similar to the resistance computations. Therefore, it can be suggested that the actuator disc model adequately captured thrust deduction, wake fraction and propeller loading changes between the trim conditions with reasonable precision.

As observed in Fig. 15, ΔP_{DM} is under-predicted 1% to 5% for the trim by the stern. Similar observations were made when predicting resistance in Section 7.1.3, leading to the conclusion that the lack of accuracy in aft trim conditions arises from modelling errors attributed to the presence of severe breaking waves and highly unsteady spill breakers and eddies. Therefore, the under-prediction of ΔP_{DM} is more likely due to the under-prediction of the resistance (or thrust) in the self-propulsion computations rather than the propeller modelling. The RANS-VOF predictions are more successful in predicting the change of power at the trim by the bow than in the aft trim, as the flow is significantly less complex for the trim by the bow compared to the aft trim.

7.3. Comparison of resistance and self-propulsion

The trends in trim optimisation for resistance, obtained from resistance tests, and delivered power, determined through self-propulsion tests, are discussed in Sections 7.1.1 and 7.2.1, respectively. It is evident that propulsive efficiency significantly influences the trim trends. This section explores the distinctions in the flow fields between the resistance and the self-propulsion tests and computations. The latter more closely resembles the full-scale ship operating at sea, as it also models the propeller and its effects. The operational propeller introduces significant variations in the pressure distribution at the aft body, and the local flow upstream, and particularly downstream of the

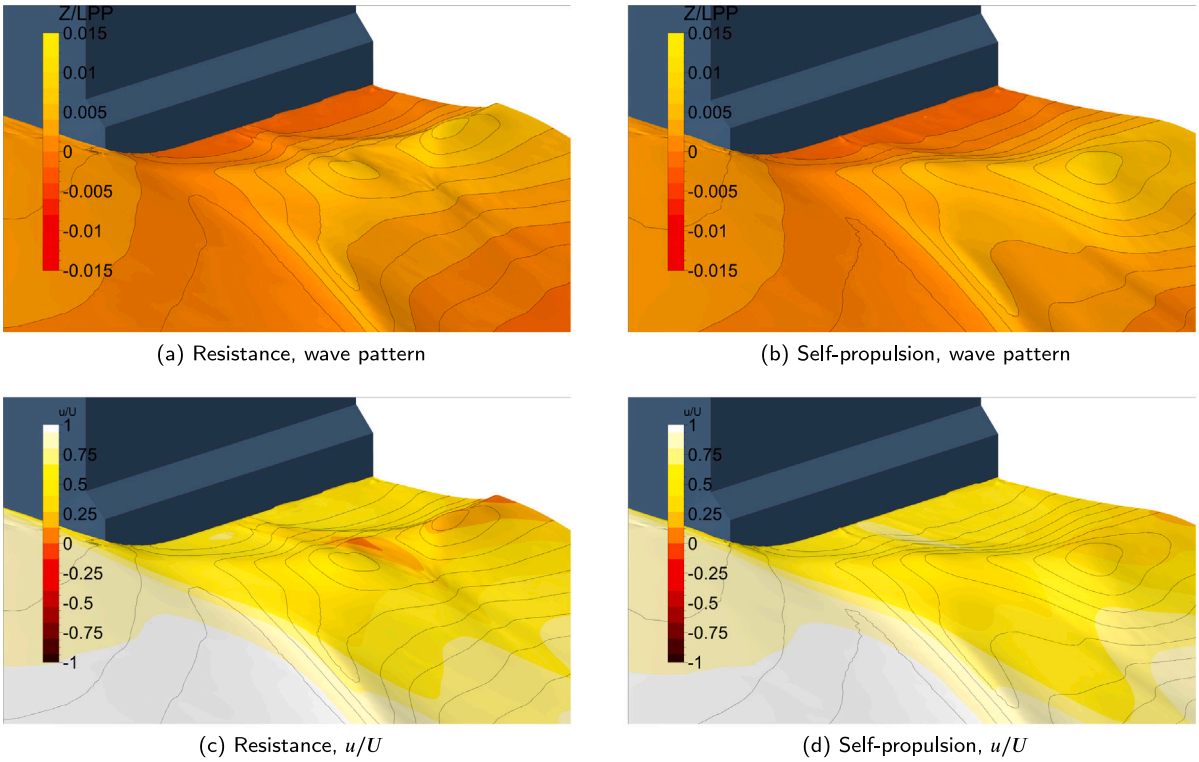

(a) Resistance, wave pattern

(b) Self-propulsion, wave pattern

(c) Resistance, u/U

(d) Self-propulsion, u/U

Fig. 16. Wake behind the transom from the RANS-VOF computations in model scale, heavy displacement even keel condition, 19 kn.

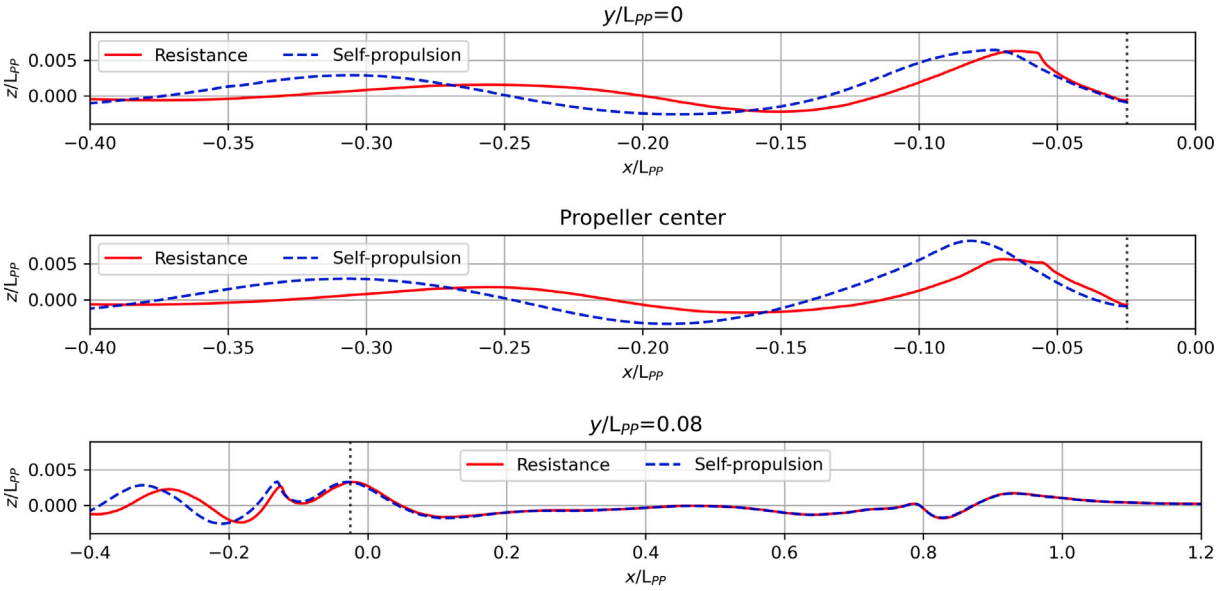

Fig. 17. The longitudinal wave cuts from RANS-VOF computations in model scale, heavy displacement even keel condition, 19 kn.

propeller location. The pressure drop induced by the propeller at the hull and the appendages, such as the rudder, causes an increase in the dynamic sinkage at the aft body and alters the wave pattern in the hull's wake compared to the resistance mode. Moreover, the propeller's jet effect extends not only downstream of the propeller but also reaches up to the free surface, potentially modifying the flow behind the transom.

Due to confidentiality constraints, the pressure distribution on the hull and the appendages cannot be presented. Instead, the wave pattern and the non-dimensional longitudinal velocity (u/V) from the resistance and self-propulsion computations at the heavy displacement even keel condition (H) at 19 kn are presented in Fig. 16. As argued earlier, the altered pressure distribution, sinkage at the aft body and the propeller jet cause a profound change in the wave pattern behind the transom as seen in Figs. 16(a) and 16(b). In the resistance computation, the trace left by the rudder (originating from approximately the middle of the centre line and side of the transom) can be observed longitudinally from the transom through the first transverse wave crest after the transom. The transverse wave is divided into two, forming a valley where the longitudinal velocity (u/V) drops below zero, indicating the flow recirculation. In self-propulsion, Fig. 16(b), the wave trace from the rudder vanishes, and the recirculating flow is eliminated not only

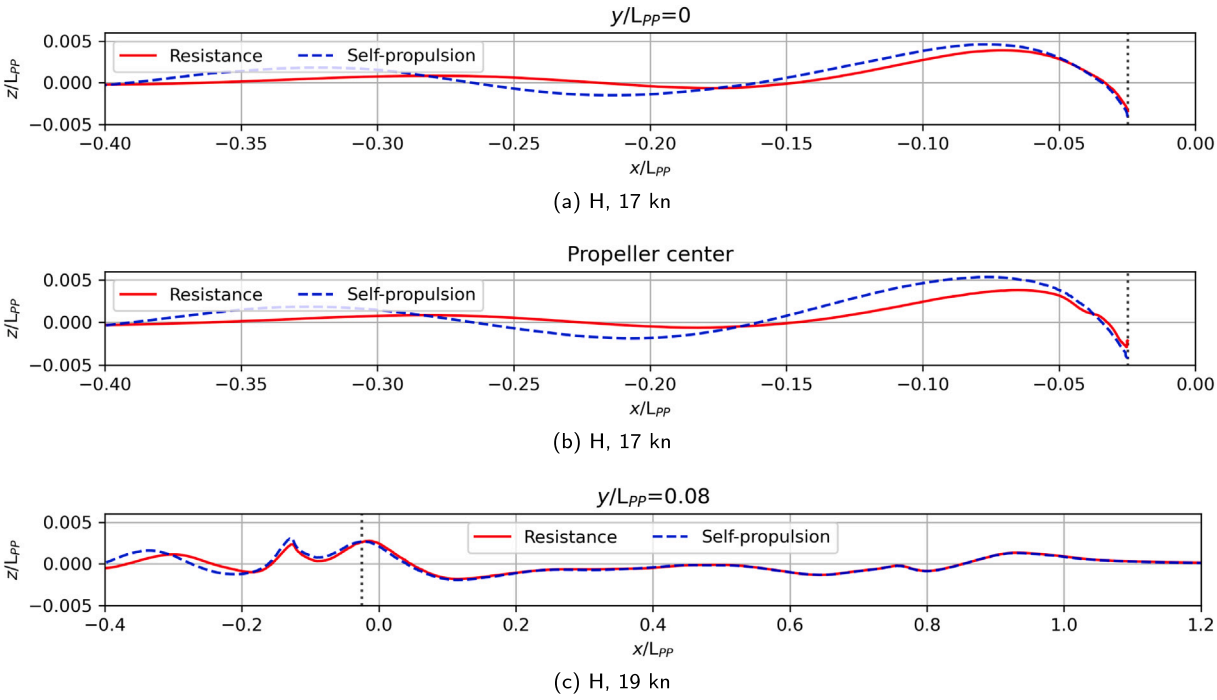

Fig. 18. The longitudinal wave cuts from RANS-VOF computations in model scale, heavy displacement trim by the stern, 19 kn.

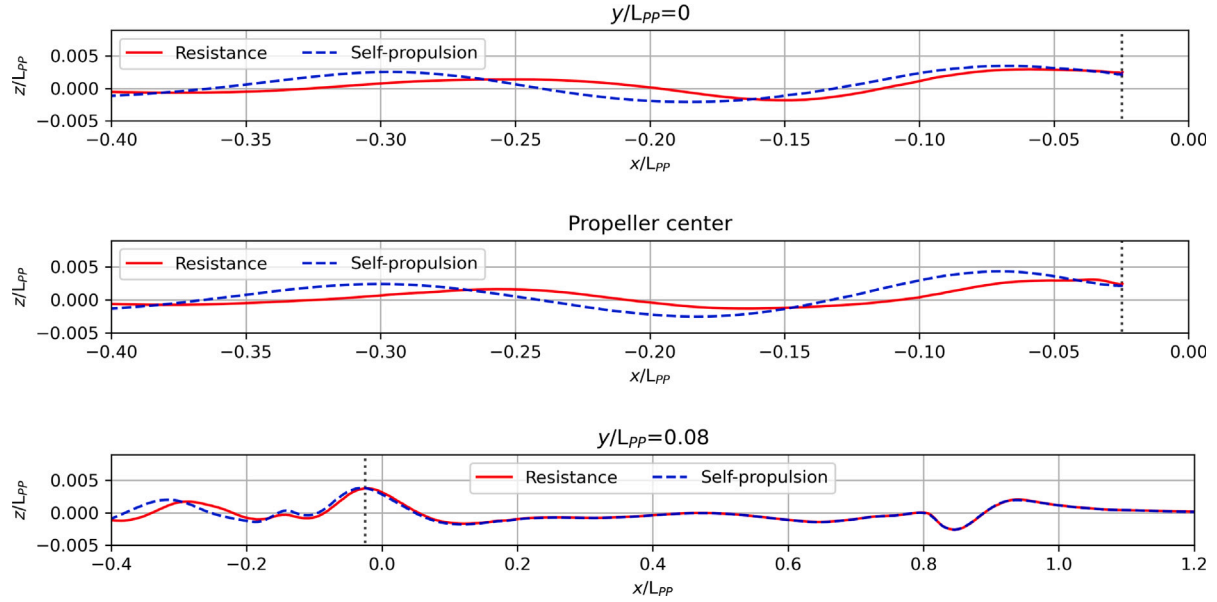

Fig. 19. The longitudinal wave cuts from RANS-VOF computations in model scale, heavy displacement trim by the bow, 19 kn.

just behind the propeller but also at the wave crest along the centre line as seen in Fig. 16(d).

To comprehend the differences in the wave pattern between resistance and self-propulsion, three longitudinal wave cuts were generated. These wave cuts are positioned transversely at $y/L_{PP} = 0$ (at the centreline), at the transverse location of the propeller centre, and at $y/L_{PP} = 0.08$ from the centreline. In Fig. 17, the wave cuts from the resistance and self-propulsion computations are represented by a solid red line, and blue dashed line, respectively. The vertical black dotted line indicates the longitudinal position of the transom. The wave cuts at the centre line and the propeller centre reveal a significant decrease in the steepness of the first wave crest in self-propulsion compared to the resistance. As mentioned earlier in Section 7.1.3, negative u/V values indicated the existence of the flow recirculation where intense spill breakers are observed (see Figs. 12(b) and 11(c)). From the CFD predictions, it can be argued that the smooth wave profiles as in Fig. 17 and non-negative u/V contours on the free surface in the self-propulsion reduced or eliminated the flow recirculation and decreased the intensity of the severe spilling wave breakers compared to the resistance. In fact, the observations from the towing tank tests align with the CFD predictions regarding the flow behind the transom.

Another distinction between the resistance and self-propulsion simulations is that the wave heights downstream of the transom are considerably increased in self-propulsion as seen Figs. 16 and 17. The longitudinal wave cuts at the centre-line and the transverse position of the propeller centre shows that the wave heights after the first wave

crest behind the transom are increased in self-propulsion by approximately 39% and 76% compared to the resistance, respectively. The wave cuts from $y/L_{PP} = 0.08$ at the downstream of the stern also shows differences between the two simulations but the change is around 14%; hence not as significant as the downstream of the propeller jet and transom. On the other hand, the wave pattern upstream of the aft body shows little to no change as the wave cuts at $y/L_{PP} = 0.08$ from both computations overlap perfectly.

The longitudinal wave cuts from the same transversal position for the H-1.5m and the H+1.5m conditions at 19 kn are presented in Figs. 18 and 19, respectively. It is evident that both trim conditions exhibit fewer differences between resistance and self-propulsion computations compared to the even keel condition. The primary reason for this observation is the flow regimes behind the transom for each loading condition. The H+1.5m at 19 kn shows a definitive dry transom flow that is less affected by the altered pressure distribution at the aft body and the propeller jet. Similarly, the H-1.5m condition exhibits nearly wetted transom flow, where extensive recirculation and spilling wave breakers occur immediately after the transom; thus, the difference in pressure and local flow between resistance and self-propulsion has a minor effect. In contrast, the even keel condition features a partially dry transom that is highly unsteady and sensitive to the more minor changes in pressure differences. Therefore, the significance of conducting self-propulsion simulations is greater for the cases where partially dry transom flow is observed.

8. Comparison of full-scale delivered power predictions

The trim optimisation towing tank tests have been extrapolated to full scale using the methods described in Section 2. In addition, the predictions from full-scale resistance simulations combined with empirical method (see Section 3.4) and self-propulsion computations (see Section 3.3) are presented. Unlike the model scale, where towing tank tests were conducted with uncertainty estimations, there is no experimental data (i.e. speed trials at the exact loading conditions) with uncertainty estimations in full scale. However, the ship monitoring data, though less accurate than speed trials, can be used to check the trends predicted by different methods.

8.1. Trim trends from extrapolation methods and CFD

The comparison of full-scale predictions is inherently more ambiguous than at the model scale because there is no *true* reference to compare predictions from different methods. Fig. 20 presents the trim optimisation results of the delivered power. In a manner similar to the earlier plots (Figs. 15 and 7), the non-dimensional delivered power predictions at trimmed conditions are presented with respect to the even keel loading at each speed and displacement (see Eq. (20)). 1957 ITTC Performance Prediction Method is denoted as 'ITTC-57', the Standard 1978 ITTC Performance Prediction Method is represented as 'ITTC-78', the ITTC-78 method with the empirical transom correction is denoted as 'ITTC-78tr', and the combined RANS-VOF and empirical self-propulsion method is denoted as 'RANS-VOF-emp' in Fig. 20.

8.2. Extrapolation methods

The towing tank tests were extrapolated using three different methods. As depicted in Fig. 20, there is noticeable agreement in the ΔP_{DS} predictions for the trim by the bow (trim> 0) among the various scaling procedures. For light displacement with bow trim (left column of plots in Fig. 20), the predictions from all three methods are within 0.2%, whereas the heavy displacement shows discrepancies among different methods of up to 1.2%. It is worth noting that the results from ITTC-78 and ITTC-78tr are identical, as there is no transom submergencein the case of bow trim for both displacements.

However, in the case of aft trim (trim< 0), as observed in Fig. 20, the agreement in ΔP_{DS} predictions among the three scaling procedures is less compared to the trim by the bow. The ΔP_{DS} predictions differ by up to 2.2% for light displacement aft trim conditions. The most significant difference is between the ITTC-78 and ITTC-78tr, as the transom is submerged at rest for the aft trim loading condition, and the transom correction is applied in the ITTC-78tr method. As previously discussed, the transom correction is valid when wetted transom flow is present (Korkmaz et al., 2022). Even though the flow behind the transom at aft trim at 15 kn indicates partially wetted transom flow, the higher speeds of 17 kn and 19 kn lean more towards a dry transom. Consequently, the transom corrections at 17 kn and 19 kn result in an artificially increased delivered power, as observed in Figs. 20(c) and 20(e).

The discrepancy in ΔP_{DS} predictions is most significant in the case of heavy displacement with aft trim at 15 kn, as shown in Fig. 20(b). In this condition, nearly wetted transom flow was observed in the towing tank tests as shown in Fig. 8(b). If the flow pattern behind the transom is similar in the model and full scale, the ITTC-78 method is unsuitable since the scaling of the viscous pressure resistance leads to under-prediction of the total resistance and delivered power as discussed by Korkmaz et al. (2022). The under-prediction stems from the flow recirculation (i.e. separated flow) behind the transom, which violates the form factor assumptions (Hughes, 1954) used in scaling the resistance. The ITTC-78tr method introduces a correction assuming that flow separation occurs in both the model and full scale, leading to differences in ΔP_{DS} predictions of up to 8.5% between ITTC-78 and ITTC-78tr methods. At other speeds (17 kn and 19 kn) with heavy displacement and aft trim, partially dry transom flow was also observed in model scale, as shown in Fig. 11(c). Therefore, the ITTC-78tr method includes a correction for submerged transom, assuming a wetted transom in both the model and full scale. This assumption likely does not hold in model scale and probably not in full scale either, causing the ITTC-78tr method to potentially over-predict delivered power in aft trim for heavy displacement, especially at higher speeds.

8.3. CFD computations

The relative changes in delivered power, ΔP_{DM}, predicted by the two CFD based methods are presented in Fig. 20. It is observed that predictions of ΔP_{DS} from both the RANS-VOF and RANS-VOF-emp methods exhibit substantial similarity, despite the latter method being computationally less intensive. In the case of a single screw vessel, the disparity in required computational resources would be even more pronounced, given that the symmetry condition at the centre-plane cannot be applied to self-propulsion computations. Thus, combining full-scale resistance computations with empirical self-propulsion predictions could be considered as an alternative approach to the free-surface RANS self-propulsion computations.

There is no *true reference* in full scale to compare the ΔP_{DS} predictions from the RANS-VOF method. However, the prediction accuracy of the RANS-VOF method in model scale self-propulsion can offer valuable insights when comparing full-scale predictions obtained through extrapolation methods and CFD. The prediction pattern of RANS-VOF exhibit similarities between model and full scale under the loading conditions where transom submergence is either absent or negligible. For instance, the model scale ΔP_{DM} predictions from the RANS-VOF method consistently under-predict the trim by the bow condition when compared to model tests. Similarly, in Fig. 20, the full-scale RANS-VOF predictions are 3%–4% higher than those obtained from extrapolation methods in the trim by the bow condition.

Conversely, at heavy displacement and aft trim conditions, where the transom is substantially submerged (with the submerged transom area comprising approximately 10% of the maximum cross-section area at rest), predictions from all methods diverge significantly, especially at the lowest speed of 15 kn. The contrast between the agreement of

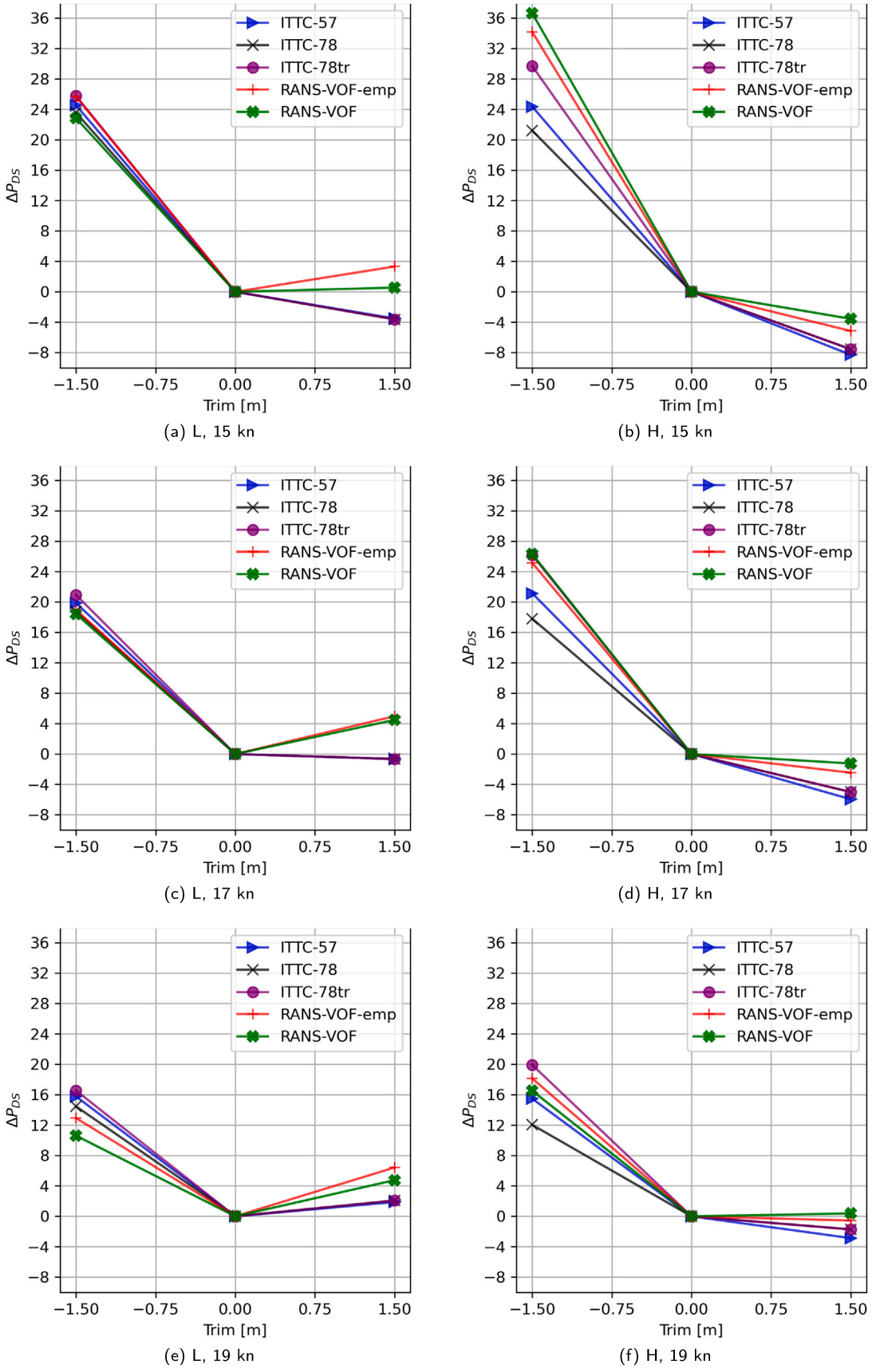

Fig. 20. Trim optimisation results of delivered power from the extrapolation methods, RANS-VOF computations and the combined RANS-VOF-empirical method.

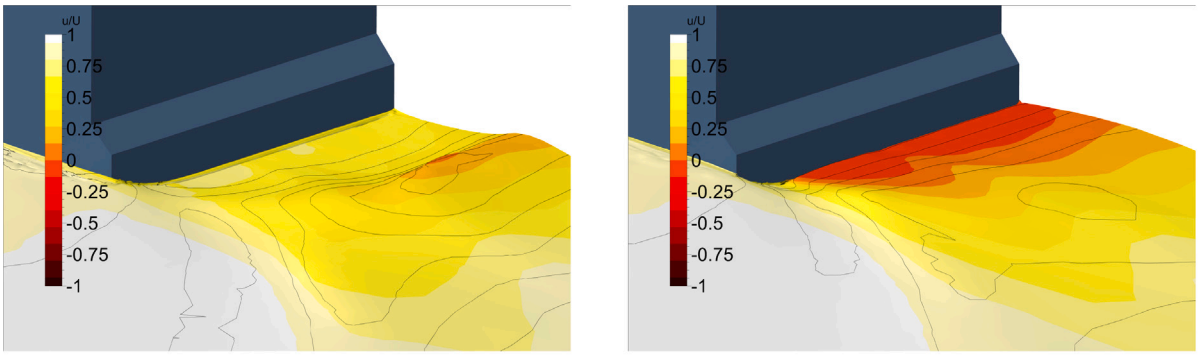

Fig. 21. Non-dimensional longitudinal velocity on the free surface from RANS-VOF computations in full scale at 15 kn.

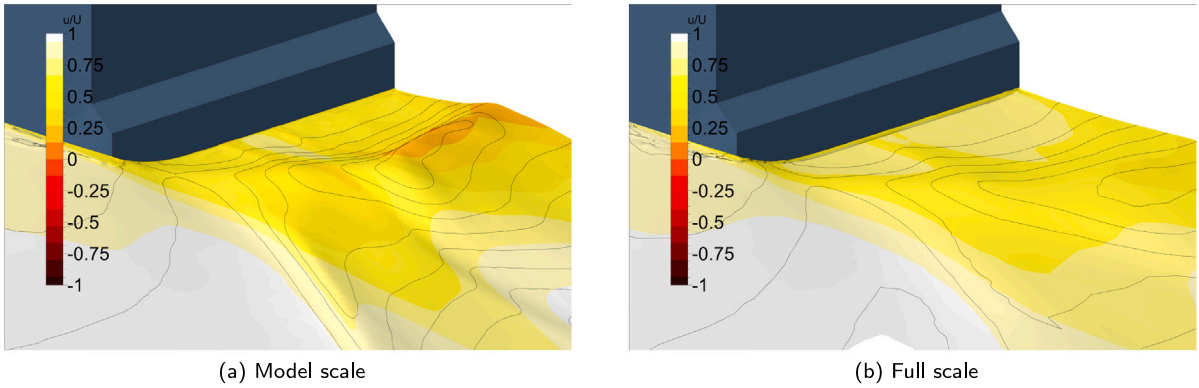

Fig. 22. Non-dimensional longitudinal velocity contours on the free surface from RANS-VOF computations in model and full scale at even keel heavy displacement loading and 17 kn.

the predictions from different methods for the light and heavy displacements with aft trim at 15 kn is significant, as seen in Figs. 20(a) and 20(b). Therefore, the wave pattern and non-dimensional longitudinal velocities on the free surface from RANS-VOF computations under these loading conditions are visualised in Fig. 21. The RANS-VOF predicts that the flow behind the transom is dry for the light displacement case. However, for heavy displacement, a partially dry transom is followed by a substantial flow recirculation zone. As previously argued, the flow separation complicates the scaling procedure for the extrapolation methods. As a result, different extrapolation methods yield vastly different ΔP_{DS} values at the aft trim condition. As depicted in Fig. 20(b), the predictions from the RANS-VOF method are closest to the ITTC-78tr method, which incorporates a correction for the wetted-transom flow. With increasing speed, the transom flow regime transitions from partially dry to completely dry transom, and the discrepancies among the different prediction methods reduces in the H-1.5m condition, as shown in Figs. 20(b), 20(d), and 20(f).

8.3.1. Model and full-scale comparison

Free-surface RANS self-propulsion computations were employed to compare the flow characteristics between the model and full scale. This comparison holds significance due to a substantial variation in loading conditions and speeds, resulting in partially dry transoms, a few instances of dry transoms, and even conditions with wetted-transom flow. As highlighted by Starke et al. (2007), partially-dry transoms are subjected to large scale effects, potentially leading to distinct flow regimes in model-scale and full-scale scenarios. An illustration of this can be observed in Fig. 22, where the model-scale RANS-VOF computations predict a dry transom, but the subsequent wave crest is steep, indicating spill breakers due to low or negative u/V values on the free surface. On the other hand, the full-scale prediction indicates a fully dry transom without a flow recirculation. The primary reason for this scale effect lies in the disparities in the boundary layer and the pressure distribution around the stern between the model and the full scale. With the boundary layer in the full scale being thinner, even when accounting for roughness effects in full-scale computations, the momentum deficit around the wave crest is mitigated, resulting in fully dry transom flow. This change in the boundary layer from model to full scale, in turn, influences the pressure distribution at the stern, which manifests itself in the wave pattern, as seen in Fig. 22. At even keel, heavy displacement, and the speed of 17 kn, the steepness of the first transverse wave crest after the transom, as well as the diverging waves radiating from the transom's side, is significantly reduced. The alteration of the transverse wave profile under these conditions can be observed more clearly in the longitudinal wave cuts in Fig. 23 (middle plot), where the model and full-scale computations are compared.

The longitudinal wave cuts at the centre-line for H+1.5m condition, where the transom outside of the water at rest, exhibit only marginal differences between the model and full scale at speeds of 15 knots, 17 knots, and 19 knots, as seen in Figs. 24, 23 and 25, respectively. The trim by the bow condition (H+1.5m) consistently results in dry transom flow at all speeds, signifying that the pressure at the transom's edge must be equal to atmospheric pressure, and the variation in the boundary layer between the model and full scale does not significantly affect the wave pattern behind the transom.

On the other hand, the trim by the stern (H-1.5m) condition results in a substantially submerged transom followed by a partially dry transom and is influenced by large scale effects. H-1.5m condition at 15 kn showed a considerable variation in ΔP_{DS} predictions among different methods as shown in Fig. 20. An examination of the wave cuts shown in Fig. 24 reveals that the transition from model to full scale does not alter the wave pattern behind the transom for the H-1.5m condition,

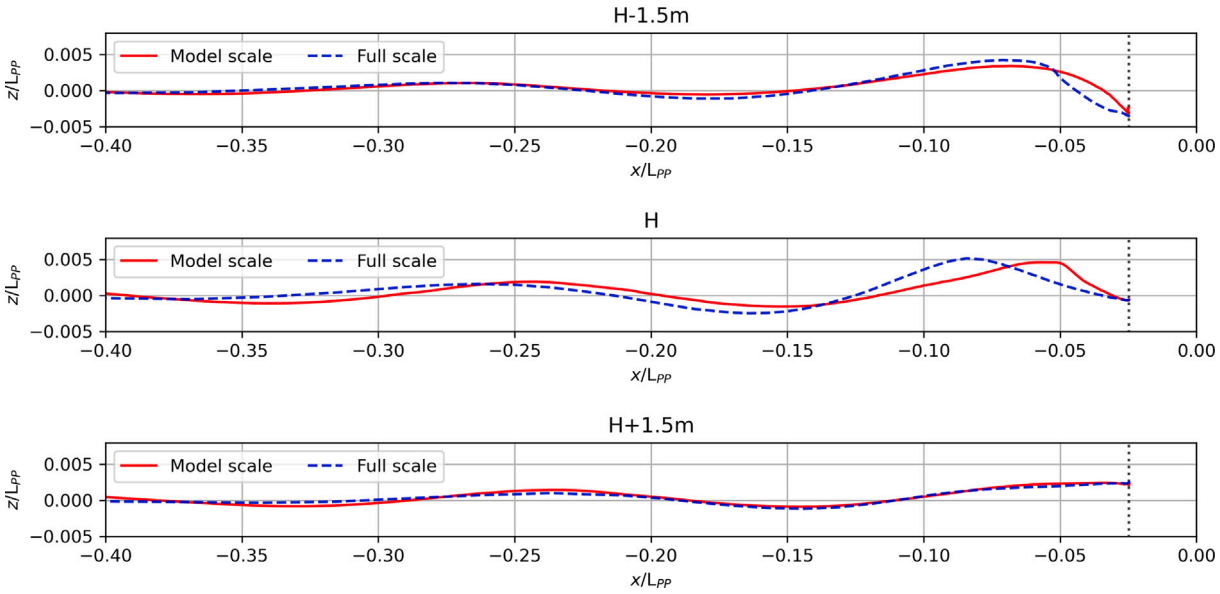

Fig. 23. The longitudinal wave cuts at $y/L_{PP} = 0$ (at the centre-line) from model and full-scale RANS-VOF computations at H-1.5m, H and H+1.5m loading conditions at 17 kn.

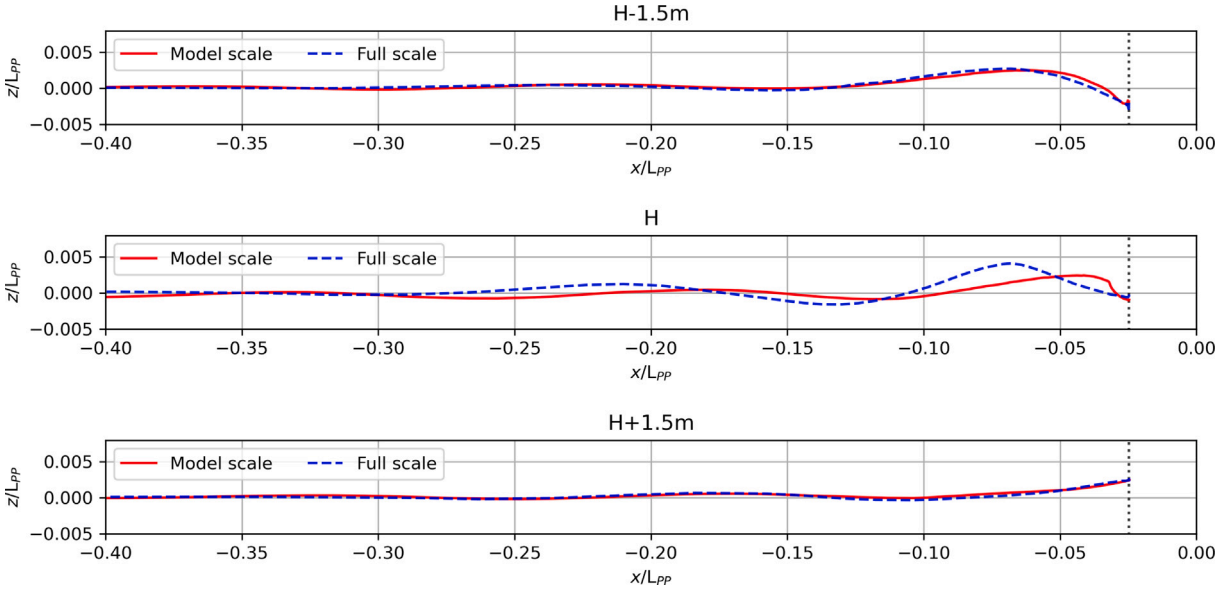

Fig. 24. The longitudinal wave cuts at $y/L_{PP} = 0$ (at the centre-line) from model and full-scale RANS-VOF computations at H-1.5m, H and H+1.5m loading conditions at 15 kn.

with the recirculating flow region persisting in full scale, as shown in Fig. 21. On the other hand, the even keel condition, H, shifts the flow regime from the partially dry transom to a dry transom. Since ΔP_{DS} represents the relative change in delivered power between the trimmed and even keel conditions, the significant variation in ΔP_{DS} under the H-1.5m condition can be attributed to the persistent flow separation in H-1.5m condition and the changing transom flow regime in the H condition.

The wave pattern behind the transom at 19 kn is also influenced by scale effects in both H and H-1.5m conditions as shown in Fig. 25. Similar to 17 kn at these loading conditions, the H-1.5m condition at 19 kn indicates that the flow leaves the transom clearly, but the momentum deficit and steep upward curvature of the wave crest lead to spill breakers; hence, partially dry transom flow is observed in full-scale.

8.4. Ship monitoring data

This section compares the full-scale predictions obtained through extrapolation methods and CFD to the ship monitoring data. The full-scale predictions are compared between the delivered power predictions and the power obtained through the propeller turning rate and the shaft torque measurements.

The analysis process is visualised in Fig. 26. Firstly, regression analyses (model **A**) were performed on the full-scale predictions, which are denoted as CFD & EFD predictions, at the two displacements (light and heavy), three trims (−1.5m, even keel and 1.5m) and three speeds. Through the regression model for each method, the full-scale delivered power can be predicted not only under the six loading conditions and three speeds but also under the other conditions that were outside of the towing tank test and CFD scope.

Secondly, the ship monitoring data is filtered (designated as filter **I**) to eliminate data points with significant environmental effects such as current, wind, wave and water depth, since the predictions were

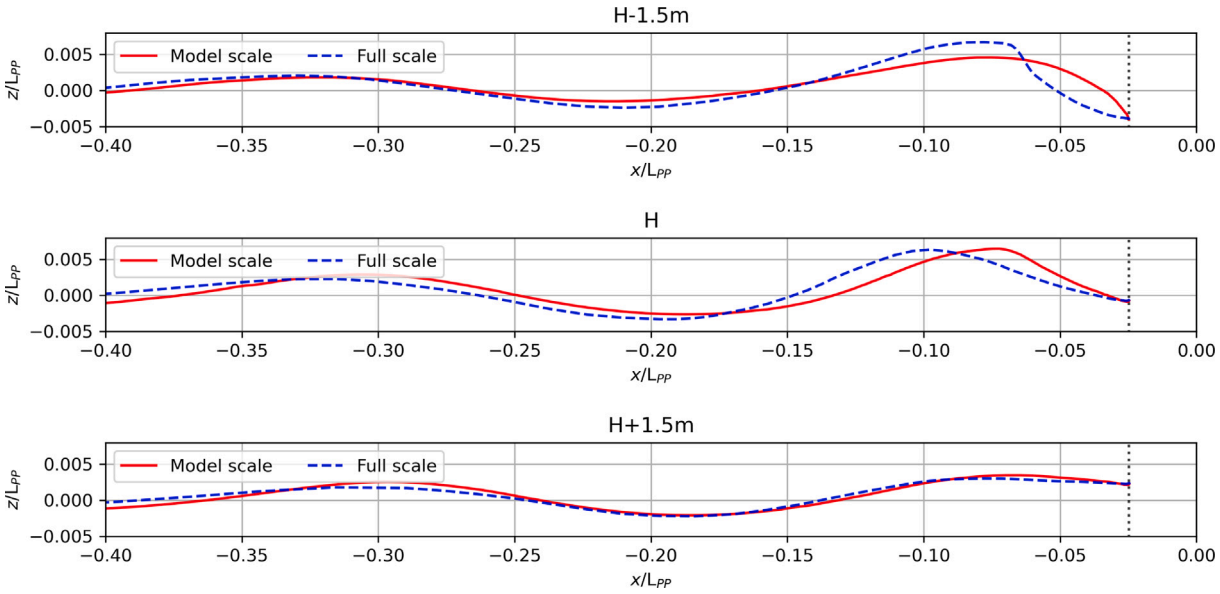

Fig. 25. The longitudinal wave cuts at $y/L_{PP} = 0$ (at the centre-line) from model and full-scale RANS-VOF computations at H-1.5m, H and H+1.5m loading conditions at 19 kn.

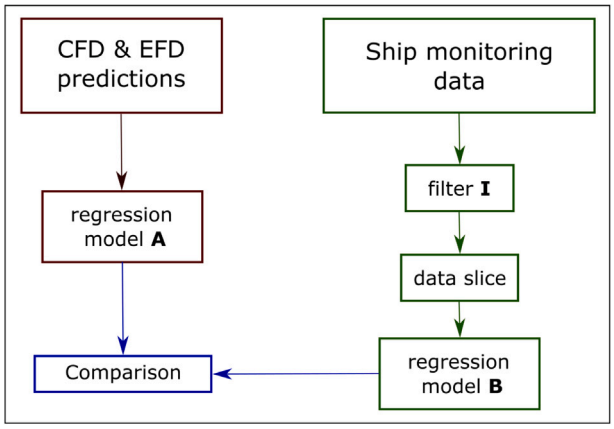

Fig. 26. Full-scale analysis process.

made for the calm and deep water. The filtered data is then sliced into six subsets based on the draught and speed criteria. Each data slice approximately corresponds to the conditions tested in the towing tank. The filtered ship monitoring data points within each slice were utilised to construct a regression model (model **B**).

Finally, the power predictions from the model **A** (predictions) and model **B** (measurements) are compared for the trim trends at the three speeds and two displacements.

8.4.1. CFD & EFD predictions

Full-scale predictions were made for two displacements, three trims and three speeds as described earlier in Section 8. Nevertheless, it is crucial to acknowledge that the actual operating conditions of the ship extends well beyond the 18 conditions derived from the CFD and EFD predictions. Consequently, the development of a surrogate model becomes necessary to approximate the conditions between the predicted conditions.

The polynomial response surface approach has been selected for constructing a surrogate model for each prediction method. The three independent variables – draught at midship (T_M), trim and ship speed – are utilised in the regression analysis to predict the dependent variable, namely, delivered power. Given the limited data points available for each independent variable, determining the polynomial degree presents a challenge. Since only two draughts are available, the polynomial's degree cannot exceed one, resulting in a linear regression. However, initial attempts with linear regression attempts yielded unsatisfactory results. The quality of the fit was assessed using the standard deviation of the errors (the difference between the dependent variable and regression predictions) in per cent of the mean delivered power, resulting in a standard deviation of the errors of 5.8% for the linear regression. Therefore, it was decided to artificially increase the number of data points through linear interpolation for the independent variables of draught and trim. Fig. 27 illustrates the eighteen original predictions (red markers) and the interpolated additional points (black markers) in three-dimensional scatter plots for each speed.

Following linear interpolation, quadratic and cubic polynomials were fitted to the data points, resulting in standard deviations of errors of 1.0% and 0.7%, respectively. The polynomial response surfaces of both fits were checked since the cubic regression might encounter issues due to incorporating three speeds in the regression. Although the quadratic and cubic response surfaces exhibited similarities, the cubic regression, with its lower standard deviation of errors, was selected for further analysis.

The cubic response surface is visualised for the ITTC-78 method predictions in Fig. 27 together with the independent variables (both original and interpolated). To maintain confidentiality, the power is presented in non-dimensional form, and the midship draught is represented by 'Heavy' and 'Light' labels approximately corresponding to the heavy and light displacements, respectively. For each plot (representing each speed) in Fig. 27, the power is non-dimensionalised by dividing the delivered power at each draught and trim condition by the power at the heavy displacement even keel condition. Qualitatively assessing the similarity between the trim trends from the data points and the resulting response surfaces at each speed reveals satisfactory agreement, as depicted in Fig. 27.

8.4.2. Ship monitoring data processing

In the initial stage, a selection of relevant variables is made from the extensive sensor data available. These selected variables characterise the ship's loading conditions, including draught at fore and aft perpendiculars, environmental factors such as current, depth below keel, apparent and true wind speed and direction, and now-casting-based swell and wave height and period. Additionally, variables describing the speed–power performance of the vessel, such as propeller turning

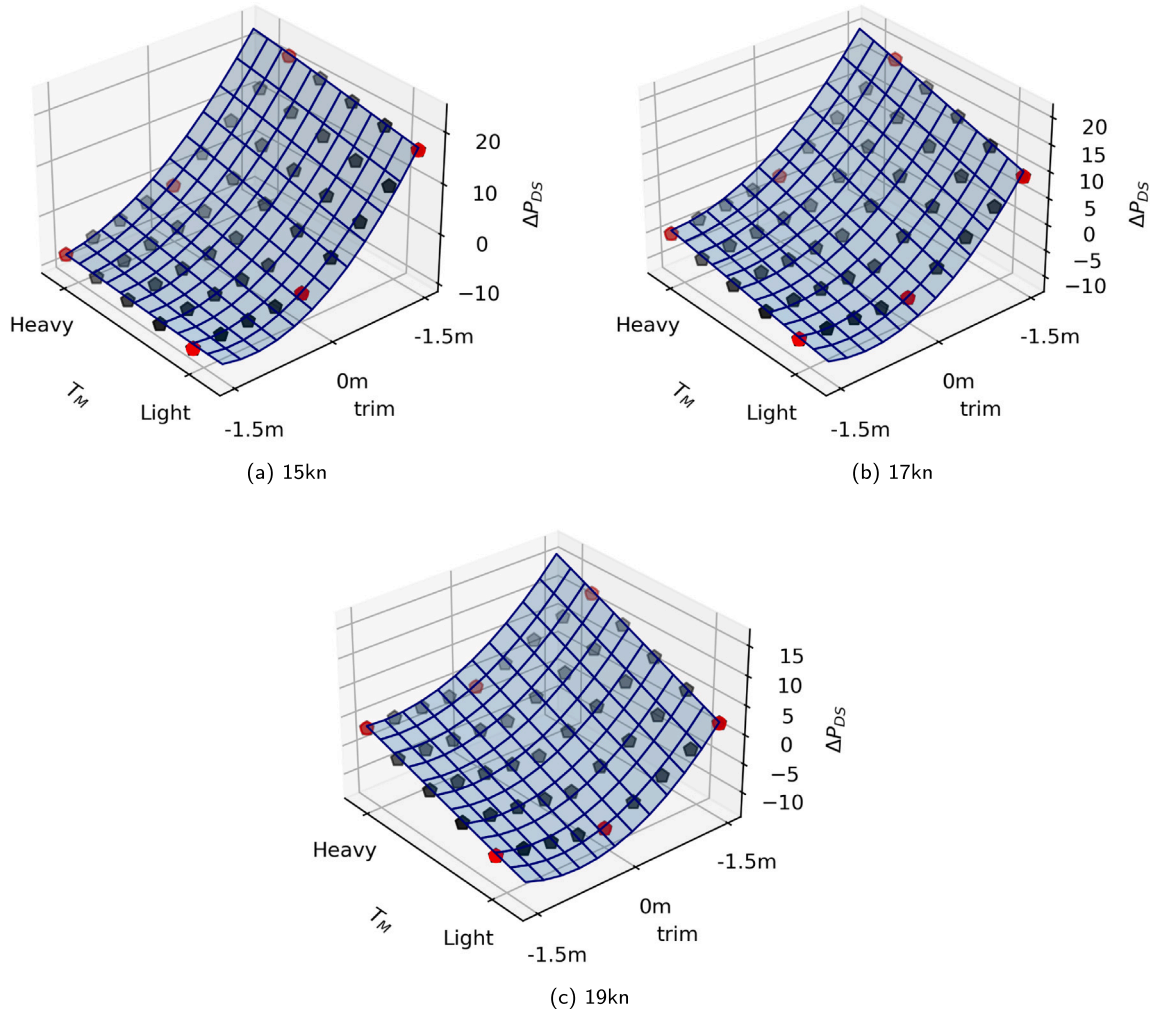

Fig. 27. Data points and the response surface for the ITTC-78 method predictions.

rate, shaft torque per propeller, speed over ground, and speed through water, are included in the selection. Subsequently, a thorough examination of the data set is conducted for each recording to ensure the presence and integrity of all selected variables. Regrettably, the now-casting-based data for wave height and period were found to be absent for the first few years of the recording. Therefore, these variables have been removed from the selection of the variables as it would have caused the loss of a significant part of the data. The exclusion of wave height and wave period variables is justifiable, given that the vessel primarily operates in waters sheltered from the open ocean swells. In such conditions, the true wind speed and direction can serve as suitable indicators of wave conditions.

After the data set was cleaned, a set of filters were applied to obtain conditions that closely resemble the calm and deep waters. This step is marked as filter **I** in the visualisation of the full-scale analysis process depicted in Fig. 26. The objective of the filter **I** is to render the delivered power describable through a regression model with only draught, trim, and the ship speed as independent variables, mirroring the approach employed in the CFD and EFD prediction methods.

The filtering process begins by selecting between speed over ground (SOG) and speed through water (STW) to represent the ship's speed. A comparison between SOG and STW reveals that the discrepancy between the two is mostly less than 2 knots. The information received from the ship operators indicated that STW were accurately obtained by the current predictions. Therefore, speed through water is chosen as the representation of ship speed. STW values less than 14.5 kn and greater than 19.5 kn were excluded from the data set, as the CFD and EFD predictions cover speeds between 15 kn and 19 kn.

The vessel continually operates between two specific harbours, with a substantial portion of the waterway between them being relatively shallow. Consequently, data from the shallow segments of the voyage must be excluded to facilitate a meaningful comparison between ship monitoring data, and CFD and EFD predictions. To achieve this, the depth Froude number (Fr_H), the h/Tm ratio (where h refers to the water depth), and the shallow water correction on the viscous resistance component suggested by Raven (2019) are calculated. Data points where $Fr_H > 0.6$ are removed to ensure that the vessel's operation remains within the sub-critical range, and shallow water effects do not significantly affect wave patterns. Additionally, data points with $h/T_m < 5$ are filtered out to minimise the shallow water effects on the viscous flow. Finally, the data points where Raven's shallow water correction (Raven, 2019) would exceed 3% of the viscous resistance are also removed. The resulting data is assumed closely resemble conditions in the deep and unconstrained waters.

The vessel's twin-screw propulsive arrangement and engine-gearbox-propeller setup provide the ship master with a wide range of operational flexibility. Depending on the environmental conditions and speed requirements, the vessel does not always operate with equal loads on each shaft line. However, the predictions from EFD and CFD were made for equal propeller loading. Consequently, the data points where either one of the shaft lines bears less than 30% or more than 70% of the total power are removed from the selection.

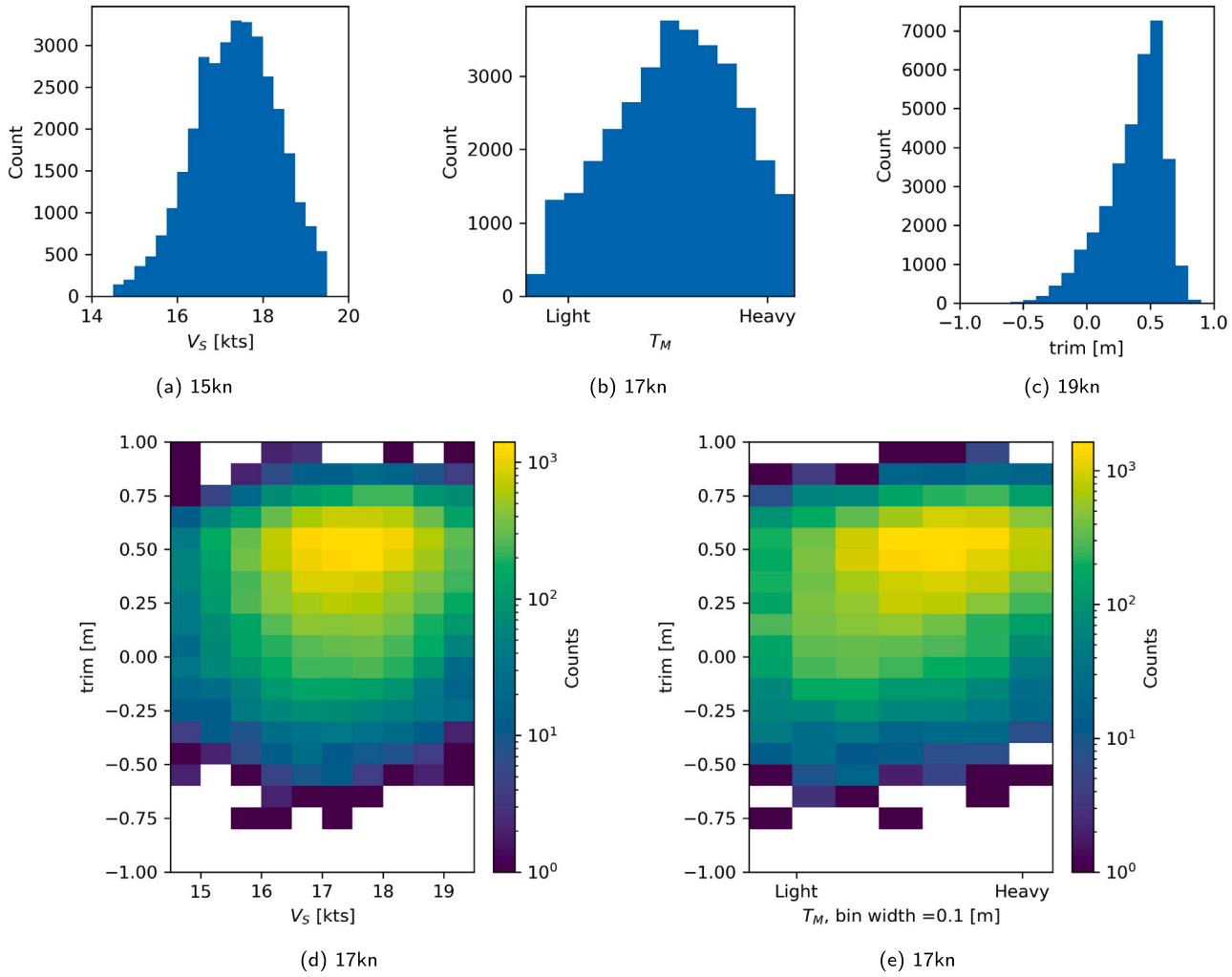

Fig. 28. Histograms of V_S, T_M and trim from the ship monitoring data.

As previously mentioned, sea wave conditions are was considered highly correlated with wind, given that the vessel operates in somewhat sheltered waters characterised by a median true wind speed of approximately 6.5 m/s, with predominant wind direction being consistent throughout the year. Consequently, the apparent wind direction indicates that the vessel usually experiences the wind from the bow. Accordingly, the maximum limit is set slightly less than twice the ship speed, and the apparent wind speeds exceeding 18 m/s are filtered out.

In addition to speed, data points with draught at midship and trim values falling outside the scope of towing tank tests are excluded. The resulting number of data points is 9.5% of the original recordings in the data set. In other words, filter **I** excludes approximately 90% of the data to align conditions similar to the full-scale CFD and EFD predictions. Histograms of ship speed (denoted as V_S), draught at midship, and trim are presented in Figs. 28(a), 28(b), and 28(c), respectively. The histograms reveal that the speed (15, 17 and 19 knots) and draught conditions (L and H) used for the predictions are not evenly distributed. Moreover, the range of trim values in the filtered data is significantly narrower than the towing tank test range (−1.5 m to 1.5 m), with a pronounced bias towards bow trim.

In addition to classical histograms, two-dimensional histograms are presented to visualise the distribution of points for each combination of trim and speed values in Fig. 28(d), and for draught and trim values in Fig. 28(e). The two-dimensional histograms also confirm uneven distribution of data in terms ship speed, draught, and trim conditions. Therefore, a regression analysis on the whole filtered data set is not considered appropriate as the data is highly skewed. Instead, the filtered data is divided into slices presented in Table 11. Each subset is aimed to represent the loading condition and the speeds tested in the towing tank earlier indicated as 'Target' in Table 11. Like the regression model A explained in Section 8.4.1, each data subset is processed with a regression analysis where the independent variables are ship speed, draught at midship and trim and the dependent variable is the total power. As evident in Figs. 28(d) and 28(e), there is a shortage of trim values at the extremities. To mitigate potential bias stemming from limited trim values, each regression model corresponding to a data subset is constructed where a sufficient number of trim values is available, as presented in Section 8.4.3.

Table 11
Data slices.

Slice no	V_S [kn]	T_M	Target
1	15.0 to 16.5	L-0.1m to L+0.2m	light, 15 kn
2	16.5 to 17.5	L-0.1m to L+0.2m	light, 17 kn
3	17.5 to 19.0	L-0.1m to L+0.2m	light, 19 kn
4	15.0 to 16.5	H-0.2m to H+0.1m	heavy, 15 kn
5	16.5 to 17.5	H-0.2m to H+0.1m	heavy, 17 kn
6	17.5 to 19.0	H-0.2m to H+0.1m	heavy, 19 kn

As illustrated in Fig. 26, regression model **B** is employed to predict the precise conditions under which full-scale predictions were conducted. To assess the performance of each data subset's regression model, residuals are calculated. These residuals represent the difference

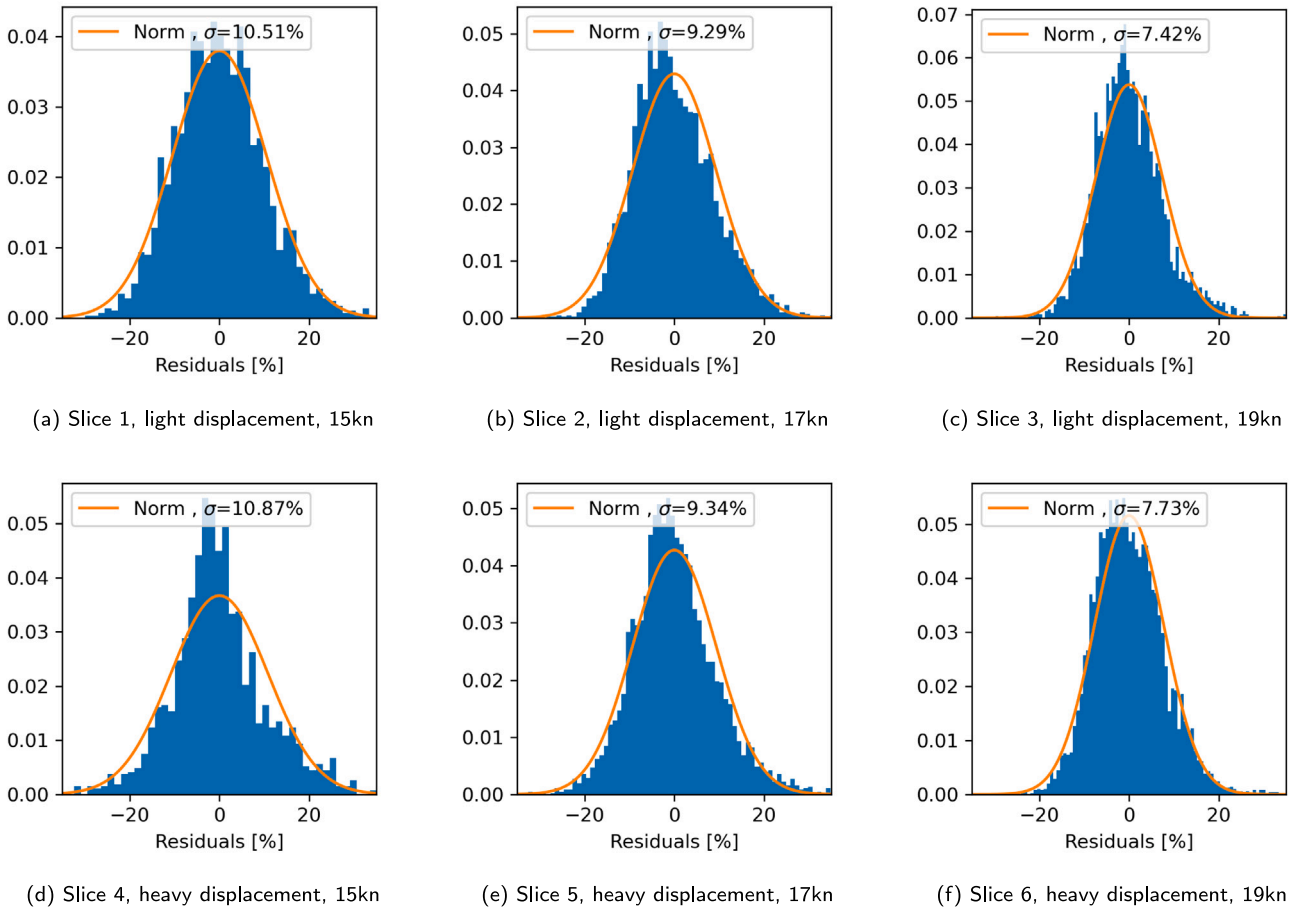

(a) Slice 1, light displacement, 15kn (b) Slice 2, light displacement, 17kn (c) Slice 3, light displacement, 19kn

(d) Slice 4, heavy displacement, 15kn (e) Slice 5, heavy displacement, 17kn (f) Slice 6, heavy displacement, 19kn

Fig. 29. The normalised distribution of errors for the regression model **B** for each data slice.

between the measured and predicted power within each data subset using model **B**. The residuals are normalised based on the power prediction at even keel conditions at the 'Target' displacement and speed specified in Table 11. The residuals and an approximation of the probability density function are presented in Fig. 29. The residuals are distributed close to a normal distribution, and the standard deviation of the normalised residuals ranges between 8% to 11%. Considering that the combined bias and precision limit of a single speed trial is approximately 8% (Insel, 2008), and that ship monitoring data collection generally exhibits less precision than speed trials conducted under relatively controlled environmental conditions, the prediction accuracy of regression model **B** step for each data subset is deemed satisfactory.

8.4.3. Comparison of predictions and ship monitoring data

The final step in the full-scale analysis process involves comparing the measured and predicted power. As shown in Fig. 26, the two regression models (**A** and **B**) can be used to estimate the trends in trim optimisation conditions explored in the preceding sections: light and heavy displacement, three speeds and the appropriate range of trim values within each data subset. In Fig. 30, predictions derived from extrapolation methods and CFD are presented alongside the trim trends derived from the ship monitoring data, denoted as data fit. Notably, the combined RANS-VOF and empirical self-propulsion (RANS-VOF-emp) method is omitted from the plot, as its full-scale predictions largely overlap with those of RANS-VOF. A reference band (the light blue shaded region) of $\pm 5\%$ is placed around the data fit curve, and histograms of the trim values are displayed above each plot. The x-axis of these histograms and the plots below them are aligned to indicate the frequency and skewness of the trim values in each data slice. The comparison of each prediction method and data fit is confined to the range where a sufficient number of trim values are available. The extent of the curves in each plot corresponds to the trim values used to generate the regression model **B** for the respective data slices. The y-axis, denoted as ΔP_{DS}, represents the change in power with varying trim values in per cent of the power prediction of each method at zero trim, for each displacement and the speed indicated in the caption. Lastly, the number of points in each data slice is indicated with N in the histogram plots.

Fig. 30 is organised and presented similarly to the earlier full-scale predictions shown in Fig. 20. The foremost and most significant observation is that all predictions from the extrapolation and CFD methods fall within the 5% reference band. Given the uncertainties associated with ship monitoring data collection and curve fitting, this strong agreement between the predictions and measurements across the entire range of loading conditions and ship speeds is noteworthy. In addition, all prediction methods and the data fit concur that trimming by the stern increases the delivered power demand at all loading conditions and speeds. While the measurements and the predictions for the trim by the bow largely align, the data fit suggests that the optimum trim occurs at smaller trim values compared to the prediction methods.

It is worth noting that the trim trends derived from the ship monitoring data fit exhibit some inconsistencies. For instance, the data fit indicates changes in delivered power of approximately −6%, −1% and −4% for the heavy displacement, 0.75 m trim at the speeds 15 kn (Fig. 30(b)), 17 kn (Fig. 30(d)), and 19 kn (Fig. 30(f)), respectively. However, this trend cannot be justified, as flow phenomena observed in the towing tank tests and the CFD computations suggest a monotonic change. Therefore, the trim trends derived from the ship monitoring

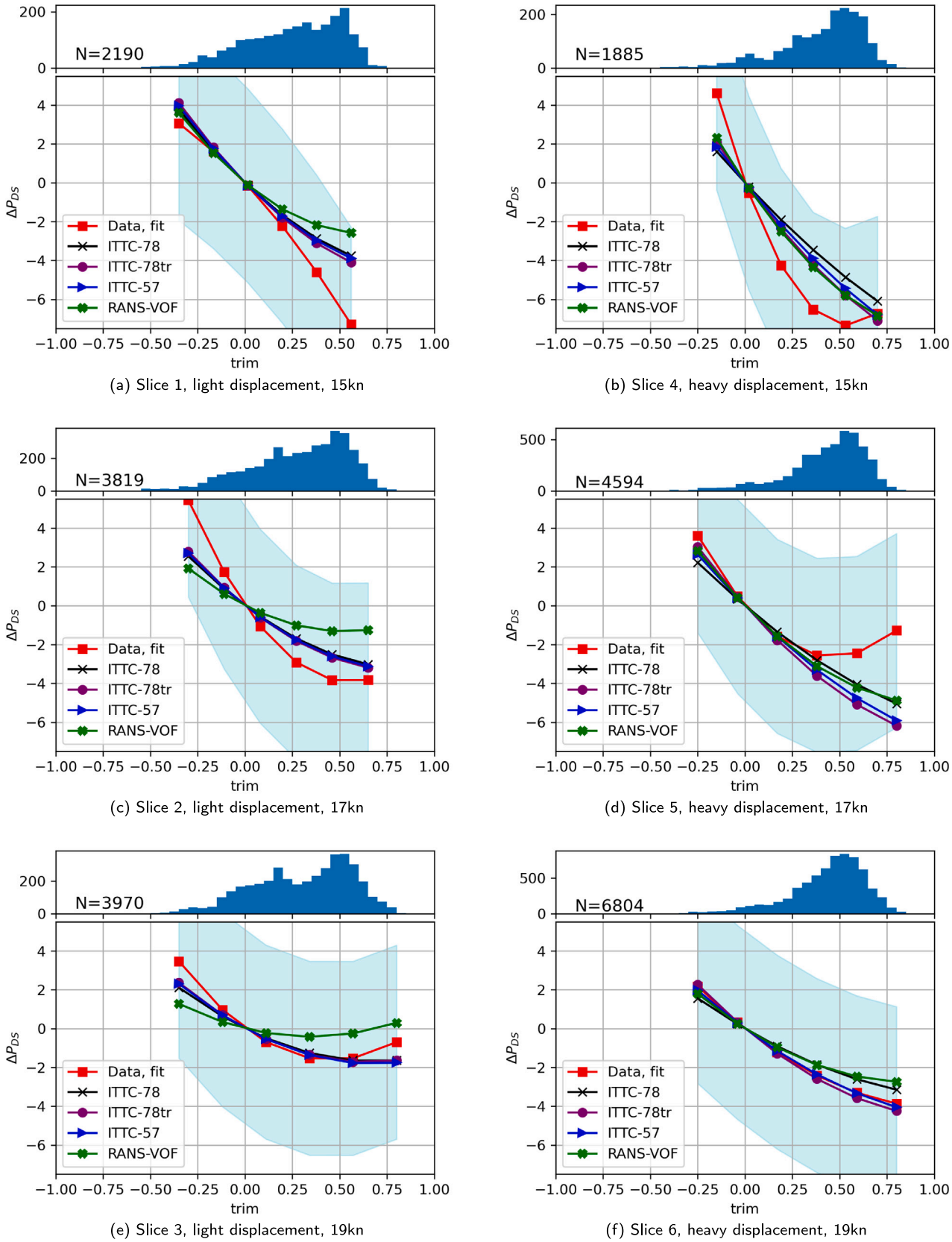

(a) Slice 1, light displacement, 15kn

(b) Slice 4, heavy displacement, 15kn

(c) Slice 2, light displacement, 17kn

(d) Slice 5, heavy displacement, 17kn

(e) Slice 3, light displacement, 19kn

(f) Slice 6, heavy displacement, 19kn

Fig. 30. The comparison between the trim trends from the ship monitoring data, the extrapolations methods and RANS-VOF.

data should only be used as an indication with a considerable reference band that can account for some of the fluctuations observed in the data curve fits.

9. Conclusions

In this study, the trim optimisation trends of a RoPax vessel were investigated using experimental and computational methods. The accuracy of various CFD methods in the model scale was assessed through comparisons made with towing tank tests. Subsequently, full-scale predictions obtained from both experimental and computational methods were compared with the ship monitoring data.

Four grid dependence studies were conducted using adaptive grid refinement technique. The resistance and self-propulsion computations, covering both model and the full scales, exhibited a pattern of monotonic and asymptotic convergence for the series of meshes. It is noteworthy that imperfect geometrical similarity , coupled with the potential existence of higher-order errors, may have contributed to modest fluctuations observed between the power-of-law curve fits and computed values. Nevertheless, the utilisation of grid adaptation predicated on metric tensors (i.e. the adaptive grid refinement) proved effective in generating series of meshes suitable for grid convergence studies, both at the model and the full-scale Reynolds numbers.

The model scale computations were validated against the model test results with measurement uncertainty estimations at the even keel heavy displacement loading condition. The validation was achieved from a programmatic standpoint for the total resistance from the resistance computations with the finest three grids. However, the comparison error for the thrust from the self-propulsion computation exceeded the validation uncertainty, pointing towards nonnegligible modelling errors. Considering the simplistic approach of the actuator disc model used in this study, some modelling errors are expected. However, the off-prediction of the absolute values can be tolerated concerning the trim optimisation studies as the relative change between the loading conditions is more important to capture than the absolute value.

Towing tank resistance tests revealed limited potential for resistance reduction through trimming by the bow, while trimming by the stern resulted in significant resistance penalties across all loading conditions and speeds. Comparison between different CFD methods and the towing tank resistance tests yielded the following insights:

- the combined double-body RANS and potential flow method proved inadequate in accurately predicting resistance trim trends for the test case. The double-body approach struggled to model substantial changes in submerged geometry due to wave patterns or dry transoms. Additionally, the potential flow method was challenged by significant breaking waves and transom flow regimes characterised by high viscous effects, such as wetted and partially dry transom flows.
- The RANS-VOF method provided generally accurate replication of towing tank resistance tests. Notably, its prediction accuracy was significantly higher for the trim by the bow conditions compared to the trim by the stern. This observation is attributed to the modelling errors caused by highly unsteady and complicated flow phenomena observed when the transom is substantially submerged. Nonetheless, the primary flow features such as transom dryness, recirculation zones, and wave patterns were predicted accurately by the RANS-VOF method.
- Examination of resistance components in various loading conditions and speeds showed that changes in frictional resistance component with respect to trim was insignificant. The viscous pressure resistance also shows a limited variation with respect to trim, unless the flow regime behind the transom changes. In contrast, wave resistance (or residual resistance) exhibited significant variations with different trims, making it the primary contributor to potential gains or losses resulting from trimming.
- The trim trends of a vessel are primarily influenced by transom submergence and the consequent flow regimes behind the transom. However, the design of the forebody, including the bulbous bow, also played a significant role in determining optimal trim. It is essential to note that bulbous bows optimised for specific narrow operational conditions could lead to undesirable wave patterns and increased resistance when the vessel is in a trimmed state.

In addition to resistance tests, self-propulsion tests were conducted in the towing tank. The trim trends observed for resistance and self-propulsion tests were generally in agreement. However, significant variations in propulsive efficiency variation with trim were noted. Consequently, accurately quantifying the optimum trim and potential gains or losses necessitates self-propulsion tests. The effect of the propeller jet was also found to have a substantial impact on dynamic sinkage and trim, and local flow.

Self-propulsion towing tank tests were replicated using the RANS-VOF method with a relatively simple actuator disc model. While prediction accuracy in power was slightly lower for self-propulsion simulations compared to predicting resistance from the resistance tests, the actuator disc model effectively captured variations in propulsive efficiency. Furthermore, the propeller jet generated by the actuator disc reproduced the local flow differences, particularly in conditions involving partially dry transoms, as observed in resistance and self-propulsion tests.

Full-scale predictions for delivered power were made using three different extrapolation methods: one computational method and one combined CFD & empirical method. Comparison of these prediction methods revealed that

- transom submergence is the most decisive factor for the agreement between prediction methods. The trim trends for power predictions from the extrapolation methods closely aligned when transom submergence was minimal (i.e., light displacement at even keel and bow trim, and heavy displacement in trim by the bow). Conversely, power predictions for the trim by the stern (involving large transom submergence) exhibited substantial variation.
- predictions from the direct full-scale CFD (RANS-VOF) and the combined CFD & empirical method were largely similar. Given the significantly lower computational resources required for the latter, it presents a viable alternative to full-scale self-propulsion computations. However, the combined CFD & empirical method necessitates estimations for the propulsive factors, which may pose challenges for users lacking a robust reference or database.
- among the three EFD based extrapolation methods, the ITTC-78 method with transom correction exhibited the closest agreement with full-scale CFD predictions.

In addition to comparing flow fields between the resistance and self-propulsion at the model scale, free surface RANS self-propulsion computations were employed to compare local flow between the model and full scale. Conditions involving partially-dry transom flow exhibited significant scale effects. In some cases, the flow regime behind the transom was fully dry at full scale but partially dry at the model scale. In other instances, both scales exhibited partially dry transom, but wake and wave pattern behind the transom varied considerably between the model and full scale. Scale effects were less pronounced when the transom was fully wetted or dry.

Comparison between ship monitoring data and predictions from extrapolation methods and full-scale CFD revealed similar trim trends across various loading conditions and ship speeds. While optimum trim angle indications from ship monitoring data were slightly smaller than those suggested by EFD and CFD based predictions, all prediction methods' trim trends were are within 5% of the measurements. It is advisable to use ship monitoring data as an indication with a reference

band of 5% or more, which can account for the artificial fluctuations observed in the data curve fits.

In summary, the full-scale self-propulsion CFD method (denoted as RANS-VOF) emerges as a reasonably accurate and cost-effective approach for determining trim trends. However, it is crucial to acknowledge the potential presence of modelling errors in specific loading conditions, underscoring the importance of thorough verification and validation studies are advised. In case of towing tank testing, results should be extrapolated using a method that incorporates corrections for the substantially submerged transom.

The conclusions and recommendations derived from this study are applicable primarily to deep and calm sea conditions, which may not always reflect real ship operation scenarios. Consequently, further research is needed to investigate the impact of shallow waters and waves on trim trends.

CRediT authorship contribution statement

Kadir Burak Korkmaz: Conceptualization, Methodology, Validation, Formal analysis, Investigation, Data curation, Writing – original draft, Writing – review & editing, Visualization. **Sofia Werner:** Conceptualization, Methodology, Investigation, Writing – review & editing, Supervision, Project administration, Funding acquisition. **Rickard Bensow:** Conceptualization, Methodology, Investigation, Writing – review & editing, Supervision.

Declaration of competing interest

The authors declare that they have no known competing financial interests or personal relationships that could have appeared to influence the work reported in this paper.

Data availability

The authors do not have permission to share data.

Acknowledgements

This research was funded by Energimyndigheten, the Swedish Energy Agency, grant 2020-018759, and the computational resources provided by RISE-SSPA Maritime Center. The funders had no role in the design of the study; in the collection, analyses, or interpretation of data; in the writing of the manuscript, or in the decision to publish the results.

References

Bertram, V., 2020. Fairy tales revisited – energy efficiency options. In: 5th Hull Performance & Insight Conference. Hamburg, Germany.

Broberg, L., Regnström, B., Östberg, M., 2014. SHIPFLOW Users Manual. FLOWTECH International AB, Gothenburg, Sweden.

Chen, J., Yu, C., Shen, L., 2019. Study of trim optimization based on design of experiments and rans simulation. In: 11th International Workshop on Ship and Marine Hydrodynamics. Hamburg, Germany.

Coraddu, A., Oneto, L., Baldi, F., Anguita, D., 2017. Vessels fuel consumption forecast and trim optimisation: A data analytics perspective. Ocean Eng. 130, 351–370. http://dx.doi.org/10.1016/j.oceaneng.2016.11.058, URL https://www.sciencedirect.com/science/article/pii/S0029801816305571.

Eça, L., Hoekstra, M., 2014. A procedure for the estimation of the numerical uncertainty of cfd calculations based on grid refinement studies. J. Comput. Phys. 262, 104–130. http://dx.doi.org/10.1016/j.jcp.2014.01.006.

Hansen, H., Freund, M., 2010. Assistance tools for operational fuel efficiency. In: 9th International Conference on Computer and I.T. Applications in the Maritime Industries. COMPIT 2010. Gubbio, Italy.

Hüffmeier, J., Lundman, J., von Elern, F., 2020. Trim and Ballast Optimisation for a Tanker Based on Machine Learning. Technical Report WP3, Research Institutes of Sweden, p. 55.

Hughes, G., 1954. Friction and form resistance in turbulent flow, and a proposed formulation for use in model and ship correlation. R. I. N. A. 96.

IMO, 2011. Annex 19: resolution MEPC.203(62).

IMO, 2021. Fourth IMO GHG Study 2020. International Maritime Organisation, 4 Albert Embankment, London SE1 7SR.

IMO, 2022a. 2022 Guidelines on operational carbon intensity indicators and the calculation methods (CII guidelines, G1). Annex 14: Resolution MEPC.352(78).

IMO, 2022b. 2022 Guidelines on the method of calculation of the attained energy efficiency existing ship index (EEXI). Annex 12: Resolution MEPC.350(78).

IMO, 2023. Definitions of maturity levels according to uptake across the maritime industry, and degree of proven technology/principle. URL https://greenvoyage2050.imo.org/technology-groups/.

Insel, M., 2008. Uncertainty in the analysis of speed and powering trials. Ocean Eng. 35 (11), 1183–1193. http://dx.doi.org/10.1016/j.oceaneng.2008.04.009, URL http://www.sciencedirect.com/science/article/pii/S0029801808000929.

Islam, H., Guedes Soares, C., 2019. Effect of trim on container ship resistance at different ship speeds and drafts. Ocean Eng. 183, 106–115. http://dx.doi.org/10.1016/j.oceaneng.2019.03.058, URL https://www.sciencedirect.com/science/article/pii/S0029801819301477.

ITTC, 1957. Subjects 2 and 4 skin friction and turbulence stimulation.

ITTC, 2014. General guideline for uncertainty analysis in resistance tests. ITTC – Recomm. Proced. Guidel. 7.5-02-02-02.

ITTC, 2021a. 1978 ITTC performance prediction method. ITTC – Recomm. Proced. Guidel. 7.5-02-03-01.4.

ITTC, 2021b. General guideline for uncertainty analysis in resistance tests. ITTC - Qual. Syst. Man. Recomm. Proced. Guidel. 7.5-02-02-02.

ITTC, 2021c. Open water test. ITTC – Recomm. Proced. Guidel. 7.5-02-03-01.

ITTC, 2021d. Practical guidelines for ship resistance CFD. ITTC – Recomm. Proced. Guidel. 7.5–03–02–04.

ITTC, 2021e. Quality assurance in ship CFD application. ITTC – Recomm. Proced. Guidel..

ITTC, 2021f. Quality assurance in ship CFD application. ITTC – Recomm. Proced. Guidel. 7.5-03-01-02.

ITTC, 2021g. Resistance test. ITTC – Recomm. Proced. Guidel. 7.5-02-02-01.

ITTC, 2021h. Uncertainty analysis in CFD verification and validation methodology and procedures. ITTC - Qual. Syst. Man. Recomm. Proced. Guidel. 7.5-03-01-01.

Kanninen, P., Peltonen, P., Vuorinen, V., 2022. Full-scale ship stern wave with the modelled and resolved turbulence including the hull roughness effect. Ocean Eng. 245, 110434. http://dx.doi.org/10.1016/j.oceaneng.2021.110434, URL https://www.sciencedirect.com/science/article/pii/S0029801821017194.

Kjellberg, M., Gerhardt, F.C., Werner, S., 2022. Sailing in waves: A numerical method for analysis of seakeeping performance and dynamic behavior of a wind powered ship. In: The 24th Chesapeake Sailing Yacht Symposium. Annapolis, Maryland.

Korkmaz, K.B., Werner, S., Bensow, R., 2019. Investigations for CFD based form factor methods. In: Numerical Towing Tank Symposium. NuTTS 2019.

Korkmaz, K.B., Werner, S., Bensow, R., 2021a. Verification and validation of CFD based form factors as a combined CFD/EFD method. J. Marine Sci. Eng. 9 (1), http://dx.doi.org/10.3390/jmse9010075, URL https://www.mdpi.com/2077-1312/9/1/75.

Korkmaz, K.B., Werner, S., Bensow, R., 2022. Scaling of wetted-transom resistance for improved full-scale ship performance predictions. Ocean Eng. 266, 112590. http://dx.doi.org/10.1016/j.oceaneng.2022.112590, URL https://linkinghub.elsevier.com/retrieve/pii/S002980182201873X.

Korkmaz, K.B., Werner, S., Sakamoto, N., Queutey, P., Deng, G., Yuling, G., Guoxiang, D., Maki, K., Ye, H., Akinturk, A., Sayeed, T., Hino, T., Zhao, F., Tezdogan, T., Demirel, Y.K., Bensow, R., 2021b. CFD based form factor determination method. Ocean Eng. 220, 108451. http://dx.doi.org/10.1016/j.oceaneng.2020.108451, URL https://www.sciencedirect.com/science/article/pii/S0029801820313585.

Larsson, L., Raven, H.C., 2010. Ship Resistance and Flow. The Society of Naval Architects and Marine Engineers, Jersey City, New Jersey.

Lemb Larsen, N., Simonsen, C.D., Nielsen, C.K., Holm, C.R., 2012. Understanding the physics of trim. In: 9th Annual Green Ship Technology (GST) Conference. Copenhagen, Denmark.

Mahmoodi, H., Ghamari, I., Hajivand, A., Mansoori, M., 2023. A CFD investigation of the propulsion performance of a low-speed vlcc tanker at different initial trim angles. Ocean Eng. 275, 114148. http://dx.doi.org/10.1016/j.oceaneng.2023.114148, URL https://www.sciencedirect.com/science/article/pii/S0029801823005322.

Mahmoodi, H., Hajivand, A., 2022. Numerical trim and draft optimization of a twin-screw modern surface combatant with inverted bow. Appl. Ocean Res. 123, 103186. http://dx.doi.org/10.1016/j.apor.2022.103186, URL https://www.sciencedirect.com/science/article/pii/S0141118722001298.

Menter, F.R., 1993. Zonal two-equations $k-\omega$ turbulence models for aerodynamic flows. In: 23rd Fluid Dynamics, Plasmadynamics, and Lasers Conference. Orlando, FL, U.S.A, pp. 93–290. http://dx.doi.org/10.2514/6.1993-2906.

Menter, F.R., 1994. Two-equation eddy-viscosity turbulence models for engineering applications. AIAA J. 32 (8), 1598–1605. http://dx.doi.org/10.2514/3.12149.

Prohaska, C.W., 1966. A simple method for the evaluation of the form factor and low speed wave resistance. In: Proceeding of 11th ITTC.

Queutey, P., Visonneau, M., 2007. An interface capturing method for free-surface hydrodynamic flows. Comput. & Fluids 36, 1481–1510.

Raven, H.C., 2019. Shallow-water effects in ship model testing and at full scale. Ocean Eng. 189, 106343. http://dx.doi.org/10.1016/j.oceaneng.2019.106343, URL https://www.sciencedirect.com/science/article/pii/S0029801819305062.

Regnström, B., 2008. Introduction to Overlapping Grids in SHIPFLOW. FLOWTECH International AB, Gothenburg, Sweden.

Reichel, M., Minchev, A., Larsen, N.L., 2014. Trim optimisation - theory and practice. TransNav, Int. J. Marine Navig. Safety Sea Transp. 8 (3), 387–392. http://dx.doi.org/10.12716/1001.08.03.09.

Roache, P., 2009. Fundamentals of verification and validation. Hermosa Publishers.

Sames, P.C., Köpke, M., 2012. CO2 emissions of the container world fleet. Procedia - Soc. Behav. Sci. 48, 1–11, URL https://linkinghub.elsevier.com/retrieve/pii/S1877042812027188.

Schultz, M.P., 2007. Effects of coating roughness and biofouling on ship resistance and powering. Biofouling 23 (5), 331–341. http://dx.doi.org/10.1080/08927010701461974, PMID: 17852068.

Shivachev, E., Khorasanchi, M., Day, A.H., 2017. Trim influence on Kriso container ship (KCS): An experimental and numerical study. In: Volume 7A: Ocean Engineering. American Society of Mechanical Engineers, Trondheim, Norway, http://dx.doi.org/10.1115/OMAE2017-61860.

Starke, B., Raven, H., van der Ploeg, A., 2007. Computation of transom-stern flows using a steady free-surface fitting RANS method. In: 9th International Conference on Numerical Ship Hydrodynamics. p. 18.

Sun, J., Tu, H., Chen, Y., Xie, D., Zhou, J., 2016. A study on trim optimization for a container ship based on effects due to resistance. J. Ship Res. 60 (01), 30–47. http://dx.doi.org/10.5957/jsr.2016.60.1.30.

Tezdogan, T., Incecik, A., Turan, O., 2016. A numerical investigation of the squat and resistance of ships advancing through a canal using CFD. J. Marine Sci. Technol. 21 (1), 86–101. http://dx.doi.org/10.1007/s00773-015-0334-1.

Wackers, J., Deng, G., Guilmineau, E., Leroyer, A., Queutey, P., Visonneau, M., 2014. Combined refinement criteria for anisotropic grid refinement in free-surface flow simulation. Comput. & Fluids 92, 209–222. http://dx.doi.org/10.1016/j.compfluid.2013.12.019, URL https://www.sciencedirect.com/science/article/pii/S0045793013005112.

Wackers, J., Deng, G., Guilmineau, E., Leroyer, A., Queutey, P., Visonneau, M., Palmieri, A., Liverani, A., 2017. Can adaptive grid refinement produce grid-independent solutions for incompressible flows? J. Comput. Phys. 344, 364–380. http://dx.doi.org/10.1016/j.jcp.2017.04.077, URL https://linkinghub.elsevier.com/retrieve/pii/S0021999117303650.

Wackers, J., Koren, B., Raven, H.C., van der Ploeg, A., Starke, A.R., Deng, G.B., Queutey, P., Visonneau, M., Hino, T., Ohashi, K., 2011. Free-surface viscous flow solution methods for ship hydrodynamics. Arch. Comput. Methods Eng. 18 (1), 1–41. http://dx.doi.org/10.1007/s11831-011-9059-4, URL http://link.springer.com/10.1007/s11831-011-9059-4.